RESILIENCE ASSESSMENT OF ACTIVE DISTRIBUTION NETWORKS

by

Ryan Jared Alexander Miller

A thesis submitted in partial fulfillment
of the requirements for the degree

of

Master of Science

in

Electrical Engineering

MONTANA STATE UNIVERSITY
Bozeman, Montana

December 2021

ACKNOWLEDGEMENTS

Special thanks go to Maryam Bahramipanah and Zagros Shahooei for providing counsel, insight, and continual feedback throughout the process of this work.

TABLE OF CONTENTS

TABLE OF CONTENTS CONTINUED

LIST OF TABLES

Table Page

LIST OF FIGURES

Figure Page

LIST OF FIGURES CONTINUED

Figure Page

LIST OF FIGURES CONTINUED

Figure Page

LIST OF FIGURES CONTINUED

Figure Page

LIST OF FIGURES CONTINUED

Figure Page

LIST OF FIGURES CONTINUED

Figure Page

LIST OF FIGURES CONTINUED

Figure Page

LIST OF FIGURES CONTINUED

Figure Page

GLOSSARY

LIHP – Low Impact High Probability

HILP – High Impact Low Probability

DER – Distributed Energy Resource

SG – Synchronous Generator

WT – Wind Turbine

PV – Photovoltaic

BESS – Battery Energy Storage System

BPG – Bulk Power Grid

PIC – Point of Interconnection

PCC – Point of Common Connection

SOC – State of Charge

DoD – Depth of Discharge

SRT – System Recovery Time

EIP – Equipment Impact Percentage

EDRR – Equipment Degradation-Recovery Rate

ENS – Energy Not Supplied

APNS – Average Power Not Supplied

ESR – Energy Supplied Ratio

ASSAI – Average System Service Availability Index

ABSTRACT

Power system resilience focuses on a system's ability to prepare for and recover from events which would severely degrade its performance. With severe weather events and regional disasters such as hurricanes, polar vortex cold, and wildfires increasing in frequency and intensity in recent years, work toward simulation and quantification techniques of power system resilience is more necessary than ever. To generate a realistic model, this work produces a geographic topography to geographically lay out and test power system. Furthermore, different extreme events such as flooding, hurricanes, wildfires, and tornadoes are modeled, and the proposed technique evaluates their impacts on the power system degradation and resilience. The availability of recovery resources and several stochastic recovery dynamics that modify the system's depth of degradation and recovery profile during repair time are studied in this work. Multiple resilience metrics are proposed to aid in analyzing the system's recovery performance. The performance of this proposed technique is then evaluated for a flood of intermediate intensity which causes component failures and system outages within the grid. System recovery resources are varied by adjusting the number of crews who can simultaneously repair the system. Resilience indices are evaluated, and it is shown that with increasing availability of repair crews and recovery resources, the system resilience improves. The proposed strategy can be applied to an arbitrary test system with ease. Different strategies such as energy storage management and repair prioritization can be modified in future works to test potential improvements or optimizations for a given test system under the occurrence of a specific extreme event.

INTRODUCTION

Background and Definitions

Power system resilience has been a topic of increasing interest in recent years as the frequency of extreme weather events has increased and is expected to continue increasing in the future [1]. Resilience is generally defined as the ability for a system to recover from disturbance [2]; for power systems, this definition is focused on the ability of a system to recover from highly damaging events while continuing to accomplish the primary objective of the system: to reliably deliver electrical energy to customers.

Damage to electrical infrastructure is a near certainty considering the breadth of existing equipment spanning across diverse regional climates, each bringing unique threats. Resilience and its more mature counterpart reliability are two ways to quantify a system's ability to withstand and recover from damage. The key difference between these two is in the scope of damage considered.

Reliability focuses on low-impact, high probability (LIHP) events such as localized equipment failure, minor weather impacts, or vegetation shorting conductors. The power grid was historically designed to be reliable and withstand minor disturbances. Thus, the concept of grid reliability is more mature, and industry standardized definitions and quantitative metrics have been well developed to analyze system components [3].

In contrast to reliability, resilience centers on high-impact, low probability (HILP) events such as extreme weather events and natural or human-caused regional disasters. Serious works into this subject only began several decades ago, and because of this fact, the definitions and metrics surrounding power system resilience are not yet standardized.

The purpose of this work is to describe a simulation method to evaluate a system's resilience. This simulation accepts a test system specification such as that described in [4], models and locates that system geographically on a regional topography, simulates an extreme event on the topography which will be used to degrade the system, and performs a per-hour recovery process simulation until all system equipment is fully restored. To quantify the recovery effectiveness, a series of numerically assessed resilience metrics are defined. The remainder of this chapter is dedicated to introducing alternate attempts to characterize resilience and simulate extreme event impacts on power systems according to various sources studied during the literature review process.

Resilience Characterized

Numerous attempts to characterize and quantify resilience and related metrics have been made over time. Various government agencies and research works have posited definitions such as in [5, 6, 7, 8, 9, 10]; most of these definitions center around similar features to resilience considerations. For the sake of brevity, the features described by [6] will be discussed: robustness, resourcefulness, rapid recovery, and adaptability. Robustness describes a system's ability to continue operation when confronted with an extreme event and is typically evaluated before events occur. Resourcefulness is the ability to mitigate damage and control system degradation during an extreme event. Rapid recovery is the timely restoration of a system to normal operation through effective dispatch of resources and collaboration immediately after an event occurs. Finally, adaptability is the evaluation of lessons learned from extreme events and the improvement of the system or response procedures to reduce the risk from similar events in the future.

To effectively discuss extreme events and resilience, it is helpful to study the system performance over time before, during, and after an extreme event occurs as shown in Figure 1.1 [11]. The figure portrays a generic system's overall performance metric in response to an extreme event. In this plot, an extreme event occurs at time t_A and lasts until t_B; during this time, the system performance degrades until it reaches its lowest level. From t_B until t_C, the system degradation is evaluated, and the method of best recovery is determined. At t_D, the system may be supplying loads as necessary but still requires additional recovery steps to allow for redundancy and other performance protections. After t_F, the system has returned to its full prior-event performance level.

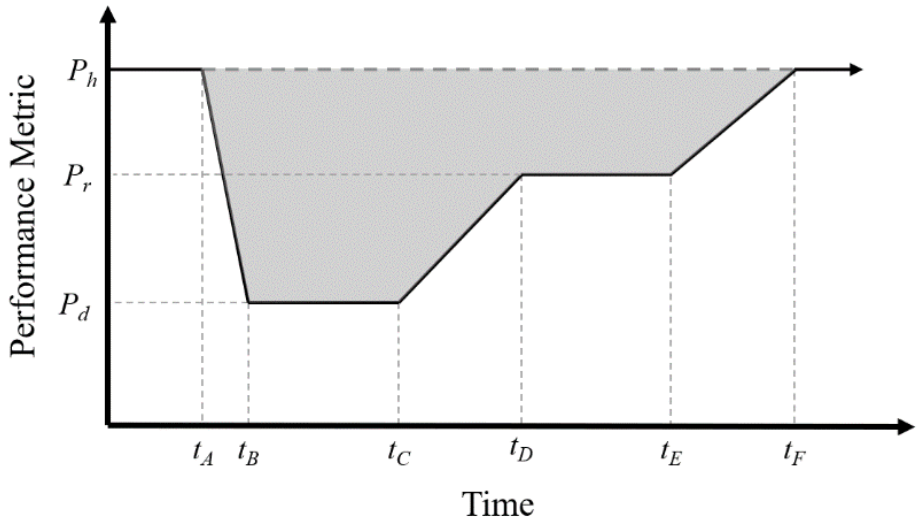

Figure 1.1. System response curve to a disruptive event. The event and its immediate aftermath occur between t_A and t_C; the system recovers between t_C and t_F. During the event, the system degrades from its healthy performance P_h to its most degraded state, P_d, before attaining a recovery performance level P_r and eventually returning to normal, pre-event operation.

There are four main zones to this extreme event response curve. Before t_A, the system is said to be in "prevention" state, where contingencies are planned, and operators maintain normal system operation. From t_A to t_B, the system falls into a "degradation" state where operators take

action to minimize damage from the highly disruptive event. Between t_B and t_C, the system stabilizes and reaches a "degraded" state where available resources are evaluated, infrastructure is inspected, and the best recovery action is planned. Finally, from t_C to t_F, the system moves into a "recovery" state where equipment is repaired, and service is restored to impacted regions. This is typically the longest stage to the entire extreme event impact process due to lack of availability of replacement parts and limited work crews. [12]

Resilience Metrics Review

Many papers exist that present ideas for metrics that could quantify a system's resilience, such as [12, 13, 14, 15]. In most cases, these metrics are focused on one stage of the extreme event response process: the recovery stage. In [12], proposed metrics focus on the grayed portion of Figure 1.1 – what is often labelled the "resilience triangle" or "resilience trapezoid". The authors propose an index that integrates the difference between nominal system performance and system performance at time *t*. Other authors, such as in [14], suggest metrics based on system degradation and recovery profiles. Others still, offer metrics derived from reliability indices, as discussed in [15]. The exact details of these indices are best left to their respective authors' writings and are outside the scope of this paper.

Simulation Processes Review

Throughout the literature review for this project, an investigation into existing modeling procedures was performed. Many simulation strategies only considered a single weather event, such as [16, 17] or made assumptions regarding the depth of a system's degradation before recovery, like in [18]. Others focused on individual component degradation and recovery instead

of the whole system in analysis. No process found through this review included equipment reliability from time in service and potential equipment failures during the recovery stage of resilience analysis. Limited research included a regional weather event impact map that incorporated differing impact likelihoods for various equipment.

The following sections of this paper will discuss the steps taken toward completion of this project. Chapter two introduces the modeling processes for the benchmark test system utilized in this work. Chapter three describes the methodology behind simulation of regional extreme weather events and how these are integrated with the benchmark test system model. Chapter four details the simulation process of the power system model degradation and recovery. Chapter five explains the metrics used to quantify resilience in terms of the simulation's execution. Finally, chapter six discusses and compares trends in the statistical results of a Monte-Carlo simulation performed for multiple system recovery configurations, modified according to system recovery resource availability.

MODELING THE BENCHMARK TEST SYSTEM

Test System Introduction

As mentioned in the previous chapter, the electrical system simulated in this project is based primarily off the benchmark test system detailed in [4]. This test system utilizes a multiple-microgrid structure, where individual microgrids can be operated either independently, connected to the bulk power grid, or isolated from the grid but interconnected to support each other. The structure of this test system is shown in Figure 2.1.

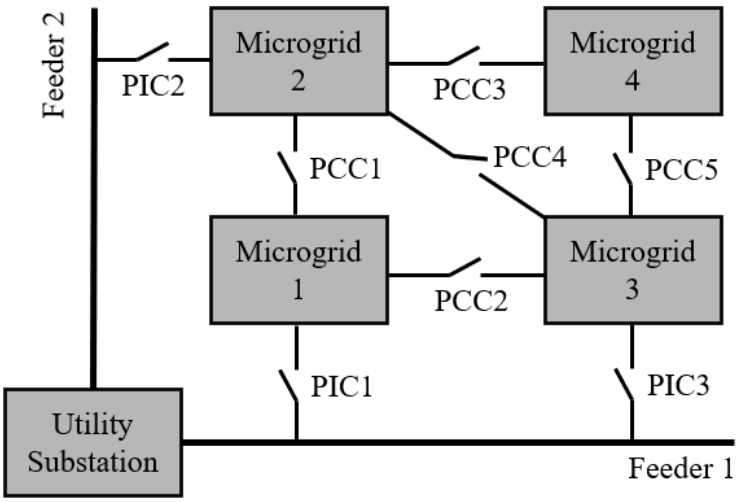

Figure 2.1. The multi-microgrid benchmark test system modeled for simulation in this project. Each microgrid can be connected to another via Points of Common Coupling (PCC), and some have connections to the utility substation through Points of Interconnection (PIC).

Each microgrid incorporates Distributed Energy Resources (DER) in the form of Synchronous Generators (SG), Wind Turbines (WT), Photovoltaic resources (PV), and Battery Energy Storage Systems (BESS). The locations of all these resources are shown in the test system one-line diagram in Figure 2.2. This diagram is taken directly from [4], which combines PV and ESS resources at buses with PV connected; therefore, no ESS's are explicitly labelled.

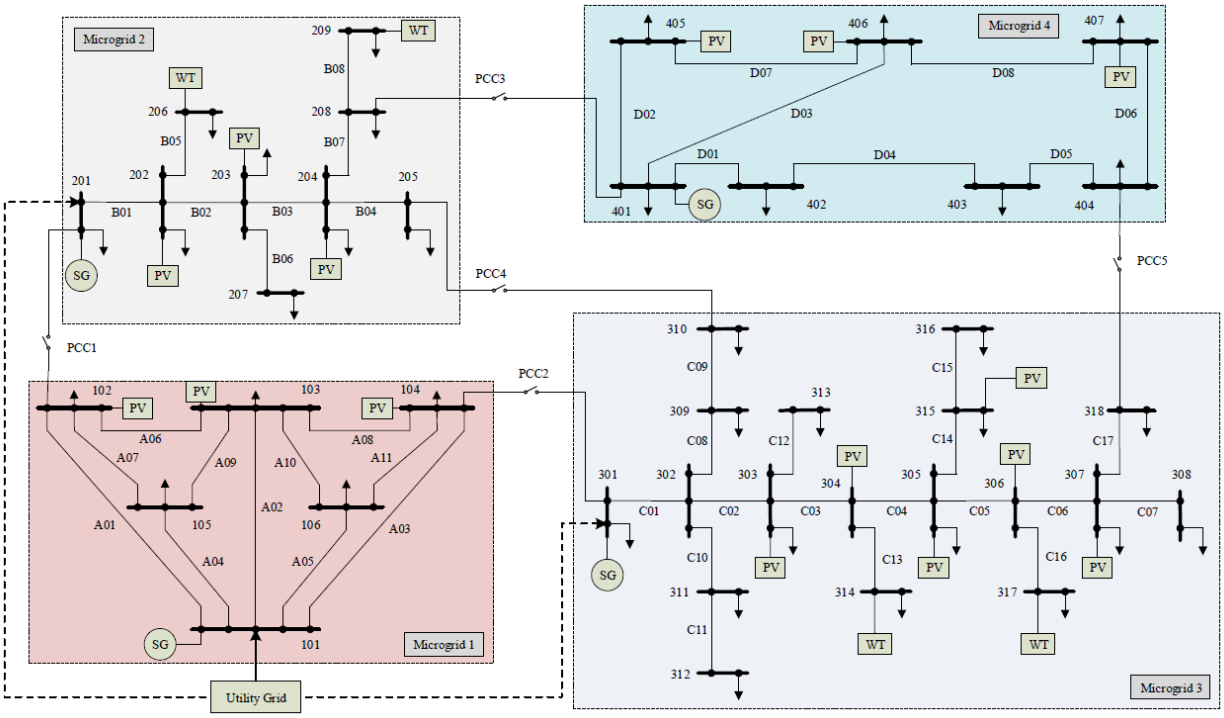

Figure 2.2. The multi-microgrid benchmark test system one-line diagram with DER's labelled. This diagram combines PV and ESS resources and is taken directly from [4].

Overall, this system incorporates 41 buses, 52 lines, 15 PV/ESS resources, 4 WT's, and 4 SG banks with a total peak system load of 31.5 MVA. Each component has basic specifications unique to the equipment type defined in [4], and that paper further includes failure rates and failure durations for most equipment to perform reliability analysis.

Each component type will be discussed in the following sections. For simplicity, transformers and circuit breakers are not modeled. Key parameters for all equipment include failure rate (to determine equipment reliability based on time in operation), failure duration (to identify mean repair time for an individual component), and unique equipment ratings depending on the equipment type (i.e., P_{max}, Q_{max}, Q_{min}, ESS Depth of Discharge [DoD], etc.). These specifications will be discussed appropriately in the following sections.

Power Line Modeling

The power line parameters (line length, impedance, current ratings, failure rates, and failure durations) are provided in Table 2.1. All lines are underground cables operating at 11kV, as specified in [4]. Additionally, four types of cabling were identified according to conductor cross-sectional area and cable placement; this specification is shown in Table 2.2, along with line classification by cable type.

Table 2.1. Line parameters, failure duration, and failure rates, as specified in [4]. Bold values represent those for which assumptions needed to be made.

ID	From Bus	To Bus	Length (km)	R (Ω)	X (Ω)	Normal Rating (A)	SCCR (kA)	Failure Rate (λ)	Fail Dur. (hr)
A01	101	102	3	0.0927	0.1431	1000	114.4	0.256	16
A02	101	103	2.4	0.0934	0.1199	890	83.8	0.25	16
A03	101	104	3	0.0927	0.1431	1000	114.4	0.256	16
A04	101	105	1.6	0.0622	0.0799	890	83.8	0.242	16
A05	101	106	1.6	0.0622	0.0799	890	83.8	0.242	16
A06	102	103	2	0.0778	0.0999	890	83.8	0.246	12
A07	102	105	1.5	0.0584	0.0749	890	83.8	0.241	12
A08	103	104	2	0.0778	0.0999	890	83.8	0.246	12
A09	103	105	1.2	0.0467	0.0599	890	83.8	0.238	12
A10	103	106	1.2	0.0467	0.0599	890	83.8	0.238	12
A11	104	106	1.5	0.0584	0.0749	890	83.8	0.241	12
B01	201	202	1.4	0.0545	0.0699	890	83.8	0.24	72
B02	202	203	1.6	0.0622	0.0799	890	83.8	0.242	24
B05	202	206	1.5	0.2385	0.1620	310	21.4	0.24	10
B03	203	204	2.2	0.0856	0.1099	890	83.8	0.241	24
B06	203	207	1.4	0.2226	0.1512	310	21.4	0.244	10
B04	204	205	1.8	0.0700	0.0899	890	83.8	0.248	24
B07	204	208	1.2	0.0467	0.0599	890	83.8	0.238	12
B08	208	209	0.8	0.1272	0.0864	310	21.4	0.234	12
C01	301	302	1.2	0.0467	0.0599	890	83.8	0.238	24
C02	302	303	1.8	0.0700	0.0899	890	83.8	0.244	24
C08	302	309	1.5	0.0584	0.0749	890	83.8	0.24	24
C10	302	311	1.4	0.2226	0.1512	310	21.4	0.24	10
C03	303	304	1.2	0.0467	0.0599	890	83.8	0.241	24
C12	303	313	1.5	0.2385	0.1620	310	21.4	0.24	10
C04	304	305	1.4	0.0545	0.0699	890	83.8	0.24	24
C13	304	314	1.4	0.2226	0.1512	310	21.4	0.241	16

ID	From Bus	To Bus	Length (km)	R (Ω)	X (Ω)	Normal Rating (A)	SCCR (kA)	Failure Rate (λ)	Fail Dur. (hr)
C05	305	306	1.6	0.0622	0.0799	890	83.8	0.238	24
C14	305	315	1.4	0.2226	0.1512	310	21.4	0.243	16
C06	306	307	1.5	0.0584	0.0749	890	83.8	0.241	24
C16	306	317	1.4	0.2226	0.1512	310	21.4	0.238	16
C07	307	308	1.5	0.2385	0.1620	310	21.4	0.24	10
C17	307	318	1.7	0.0661	0.0849	890	83.8	0.238	24
C09	309	310	1.5	0.0584	0.0749	890	83.8	0.242	24
C11	311	312	1.2	0.1908	0.1296	310	21.4	0.241	10
C15	315	316	1.2	0.1908	0.1296	310	21.4	0.241	10
D01	401	402	0.6	0.0381	0.0315	700	52.9	0.232	12
D02	401	405	1	0.0635	0.0525	700	52.9	0.236	12
D03	401	406	1.8	0.1143	0.0945	700	52.9	0.244	12
D04	402	403	2	0.1270	0.1050	700	52.9	0.246	12
D05	403	404	0.6	0.0381	0.0315	700	52.9	0.232	12
D06	404	407	1	0.0635	0.0525	700	52.9	0.236	12
D07	405	406	1.5	0.0953	0.0788	700	52.9	0.241	12
D08	406	407	1.5	0.0953	0.0788	700	52.9	0.241	12
PCC1	102	201	1	0.0309	0.0477	1000	114.4	0.256	12
PCC2	104	301	1.5	0.0464	0.0716	1000	114.4	0.256	12
PCC3	208	401	2	0.0778	0.0999	890	83.8	0.246	16
PCC4	205	310	2.5	0.0973	0.1249	890	83.8	0.246	16
PCC5	318	404	1	0.0389	0.0500	890	83.8	0.246	12
PIC1	BPG	101	1	**0.0309**	**0.0477**	**1000**	**114.4**	**0.256**	**16**
PIC2	BPG	201	3	**0.0927**	**0.1431**	**1000**	**114.4**	**0.256**	**16**
PIC3	BPG	301	3	**0.0927**	**0.1431**	**1000**	**114.4**	**0.256**	**16**

Table 2.2. Cable types used for each line defined in [4]. Bold items represent lines for which a cable type was assumed.

Cable Cross-Section Area (sq. mm)	Cable Placement	Line ID's Using This Cable Type
400	Double	A01, A03, PCC1, PCC2, **PIC1-3**
300	Double	A02, A04-11, B01-04, B07, C01-06, C08, C09, C17, PCC3-5
185	Double	D01-08
150	Single	B05, B06, B08, C07, C10-16

The only lines lacking explicit definition for impedance, current ratings, failure rate, and failure duration were those linking the microgrids to the utility grid (PIC1-3). To resolve this, all lines were generalized according to cable type used; each cable was then defined to have a specific impedance per kilometer and current ratings that could extend to all lines using that cable type. Assuming the utility grid feeder lines were built with the largest cable type available, the impedance and current ratings for the lines were known; failure rates and durations were chosen based on the typical values defined for other lines with similar cable types. That assumption process is reasonable, since the microgrids must be able to be fully supplied from the utility grid and this cable type provides the lowest losses and highest capacity under these conditions.

Load Modeling

The specification of the test system includes load data at each bus; that is, the peak P and Q values of both critical and total bus loads, according to Table 2.3. A one-year load profile is specified in terms of percentages of peak load according to weekly, daily, and hourly (by season) percentage values, as shown in tables 2.4, 2.5, and 2.6, respectively. Additionally, the number of customers who constitute total loads and critical loads on each bus are included in Table 2.3.

Table 2.3. Peak loads and customer count by bus, separated by total and critical amounts from [4].

Bus	Total Bus Load			Critical Load		
ID	Customers	kW	kVAR	Customers	kW	kVAR
101	0	0	0	0	0	0
102	437	2125	336	18	450	68
103	696	3329	1023	26	650	124
104	471	2050	555	8	200	50
105	273	1257	310	8	200	35
106	222	1056	240	8	200	35
201	150	600	100	0	0	0
202	208	1250	487	20	500	80
203	196	1203	410	20	500	80
204	205	1366	443	26	650	138
205	191	764	36	0	0	0
206	126	503	21	0	0	0
207	87	345	11	0	0	0
208	158	629	8	0	0	0
209	140	642	12	4	100	25
301	145	580	150	0	0	0
302	110	650	85	10	250	50
303	169	673	96	0	0	0
304	110	439	135	0	0	0
305	98	600	128	10	250	50
306	140	560	112	0	0	0
307	133	851	145	16	385	50
308	105	420	25	0	0	0
309	125	500	45	0	0	0
310	160	637	33	0	0	0
311	124	788	95	14	350	83
312	32	125	50	0	0	0
313	43	169	20	0	0	0
314	50	200	43	0	0	0
315	37	250	32	5	125	25
316	54	213	12	0	0	0
317	34	133	25	0	0	0
318	50	200	38	0	0	0
401	107	426	80	0	0	0
402	54	318	78	5	125	20
403	63	356	81	5	125	20
404	115	459	88	0	0	0
405	205	820	91	0	0	0
406	447	2500	635	34	850	150
407	152	816	60	10	250	44

Table 2.4. Weekly peak load as a percentage of maximum bus load. Duplicated from [4].

Week	Peak Load	Week	Peak Load	Week	Peak Load	Week	Peak Load
1	90.5	14	97.4	27	83.2	40	85.9
2	93.8	15	93.2	28	78.6	41	88.5
3	93.4	16	89	29	76.6	42	90.3
4	94.5	17	87	30	76.2	43	90.5
5	94.5	18	85	31	72.4	44	91.2
6	97.8	19	83.7	32	75.1	45	90.3
7	98	20	87.4	33	77.5	46	88.7
8	99.8	21	87.4	34	79.2	47	87
9	99.6	22	85.7	35	81.2	48	88.1
10	99.6	23	87.6	36	81.9	49	89.8
11	99.1	24	89.6	37	82.3	50	89.8
12	100	25	84.3	38	83	51	95.7
13	99.1	26	85	39	82.8	52	90.5

Table 2.5. Daily peak load as a percentage of weekly peak load. Duplicated from [4].

Day Number	Day Name	Peak Load
1	Monday	94.2
2	Tuesday	98.1
3	Wednesday	95.6
4	Thursday	100
5	Friday	97.5
6	Saturday	76.3
7	Sunday	73.9

Table 2.6. Hourly peak load by season as a percentage of daily peak load. Duplicated from [4].

Hours	Summer Weeks 1-13		Monsoon Weeks 14-26		Autumn Weeks 27-35		Winter Weeks 36-52	
	Wkdy	Wknd	Wkdy	Wknd	Wkdy	Wknd	Wkdy	Wknd
00-01	81	66	86	65	80	71	80	73
01-02	77	68	86	63	81	70	75	64
02-03	80	72	84	72	82	73	78	65
03-04	79	72	83	77	84	72	80	65
04-05	79	75	84	82	86	77	83	67
05-06	82	75	84	88	86	81	86	75
06-07	84	77	87	90	89	83	89	80
07-08	87	78	90	93	90	86	90	87
08-09	90	83	95	94	92	94	92	94

Hours	Summer Weeks 1-13		Monsoon Weeks 14-26		Autumn Weeks 27-35		Winter Weeks 36-52	
	Wkdy	Wknd	Wkdy	Wknd	Wkdy	Wknd	Wkdy	Wknd
09-10	94	89	98	94	94	94	95	97
10-11	95	88	99	96	96	94	94	97
11-12	94	88	98	97	95	94	96	98
12-13	93	88	96	96	94	89	96	97
13-14	91	86	92	94	92	86	94	89
14-15	88	84	89	94	90	84	90	86
15-16	87	86	87	88	90	86	90	81
16-17	91	93	90	89	92	90	93	85
17-18	95	97	95	94	100	96	96	96
18-19	98	100	99	100	100	100	100	100
19-20	100	95	100	96	100	98	100	100
20-21	97	93	99	98	97	91	99	94
21-22	94	85	97	95	93	85	94	92
22-23	84	72	90	82	83	70	84	80
23-00	88	74	93	73	83	71	83	80

The load data was formatted into configuration files as lookup tables during the simulation runtime to provide the load at any bus at any hour of the year. On each bus, it is assumed that normal and critical loads are grouped into combined circuits such that when switched, all normal loads and/or all critical loads can be in or out of service, but no bus can partially supply normal or critical loads.

DER's Modeling

Perhaps one of the most intensive steps in the modeling process was building the models for DER's in this system. Four types of DER were employed: SG, WT, PV, and BESS. Each of these is described in [4], but in terms of what was necessary for the simulation model, most were underspecified. The modeling process and assumptions for each DER in this system are detailed in the following subsections.

SG Resources

The benchmark test system defines the inclusion of standby SG's at bus number one of each microgrid (101, 201, etc.). These SG banks are composed of multiple units with kVA ratings large enough to supply the entire microgrid alone if all other resources (utility grid interconnections, PV, WT) were to fail. The specification for these resources is provided in Table 2.7.

Table 2.7. SG resource ratings. Bold items were not defined in [4] and required assumptions.

Bus ID	Unit capacity (kVA)	Number of Units	Unit QG_{min} (kVAR)	Unit QG_{max} (kVAR)	Combined Failure Rate (λ)	Failure Duration (hr)
101	5000	3	-3000	5000	**0.015**	**75**
201	2000	3	-1500	2000	**0.006**	**30**
301	2000	3	-1500	2000	**0.006**	**30**
401	2000	2	-1000	2000	**0.004**	**20**

Combined failure rate and failure duration represent values which were not originally specified by the test system and required assumptions to be made. No resources could be found that adequately specified failure rates or failure duration for standby generators, so values needed to be assumed. To simplify modeling, the entire SG bank is modeled as one contiguous unit; this modeling strategy is an all-or-nothing approach for this resource and does not allow for de-rated generating capability if, for example, one unit had an in-service failure and others continued operating normally.

To set the combined failure rate of the generator bank, it is assumed that a well-maintained generator would have a low failure rate. This value is calculated according to Equation 2.1, where the constant multiplier is chosen to facilitate a small failure rate.

$$\lambda = 10^{-6} \times (combined\ unit\ capacity)\ \text{[f/yr]} \qquad \text{(Eq. 2.1)}$$

Failure duration is similarly set, assuming the largest generator bank would require just over three days to repair; accordingly, failure duration is calculated by Equation 2.2.

$$FD = 0.005 \times (combined\ unit\ capacity)\ \text{[hrs]} \qquad \text{(Eq. 2.2)}$$

The 0.005 constant in this equation is set according to the target repair time for the largest SG bank.

Additional SG parameters provided in the test system specification were disregarded, including any highly detailed information pertaining to generator time constants or stator resistance/reactance. These values would be necessary for a detailed time-domain analysis of performance during fault scenarios but are unnecessary for the scope of this work.

Finally, the per-unit SG capability curve assumed for this model is shown in Figure 2.3, where this curve traces an ellipse with the vertical axis as real power output and the horizontal axis as reactive power output. The SG can operate anywhere within the shaded region.

Figure 2.3. The assumed per-unit P-Q capability curve for SG resources, where the SG can operate anywhere within the shaded region.

WT Resources

The locations of four WT resources are included in the [4]. The location and ratings of these resources are provided in Table 2.8.

Table 2.8. WT ratings and locations. Bold items were not pre-defined and required assumptions.

Bus ID	PG_{max} (kW)	QG_{min} (kVAR)	QG_{max} (kVAR)	Combined Failure Rate (λ)	Failure Duration (hr)
206	800	-250	250	**0.04**	**32**
209	500	-200	200	**0.025**	**20**
314	500	-250	250	**0.025**	**20**
317	1200	-600	600	**0.06**	**48**

Like the SG resources, the original test system did not provide failure rates or failure durations for any WT, so assumptions were made according to the maximum output for each resource. Failure rate was calculated according to Equation 2.3 with a target failure rate of 0.005 per 100 kW rating of the WT.

$$\lambda = (5 \times 10^{-5}) \times (WT\ P_{\max}\ Rating)\ \text{[f/yr]} \qquad \text{(Eq. 2.3)}$$

According to [19], a single 2 MW wind turbine typically experiences one failure per year. Based on this data, the estimate used in this work is overly optimistic for reliability of WT resources. Since this study is not focused on reliability, the given failure rate assumptions are still adequate for accomplishing the objective of this project: analysis of resilience to extreme events.

Failure duration for each WT is chosen based on a target repair time of 20 hours for a 500kW resource and is calculated according to Equation 2.4. This assumption is not unreasonable when compared with data from [20] which identifies downtimes for large offshore

wind resources between 25 and 118 hours. For a smaller WT resource on land, the failure duration can reasonably be expected to be less.

$$FD = 0.04 \times (WT\ P_{max}\ Rating)\ \text{[hrs]} \quad \text{(Eq. 2.4)}$$

The test system specification defines an annual wind availability table by hour of the day. Provided in Table 2.9, this data defines the percentage of maximum rated output power capacity for a given hourly window. This percentage availability is used to set the real power availability for the WT and derive the available reactive power generation limits according to Equation 2.5. A per-unit representation of the WT capability curve is shown in Figure 2.4, where the WT can operate anywhere in the shaded region. This plot is based on data from [21].

$$Q_{max\ or\ min} = \pm \left| \frac{Q_{max}}{0.2 * P_{max}} * P_{available} \right| \text{[kVAR]} \quad \text{(Eq. 2.5)}$$

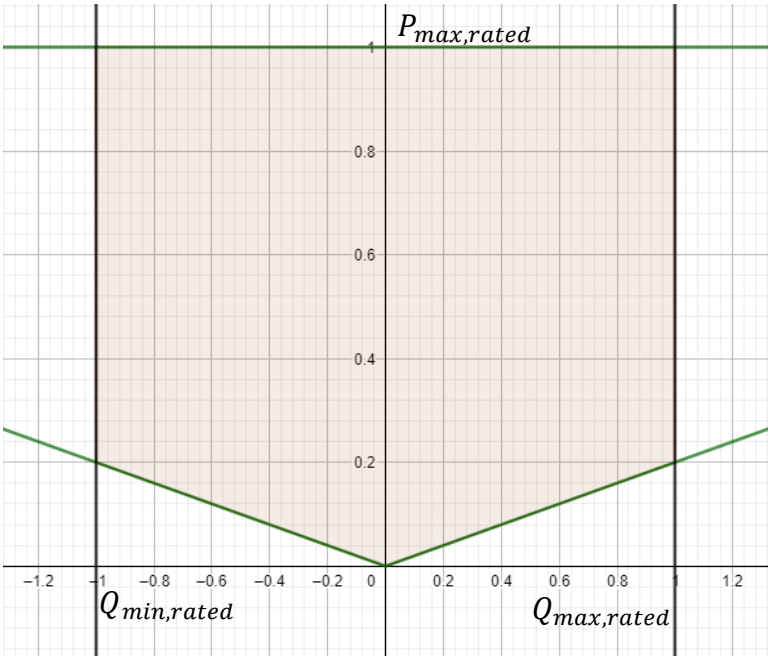

Figure 2.4. The assumed per-unit P-Q capability curve for WT resources, where the WT can operate anywhere within the shaded region.

Table 2.9. WT power availability by week of the year and hour of the day.

Week	Wind Power Generation (%) in 24 hours of the day											
	0-2	2-4	4-6	6-8	8-10	10-12	12-14	14-16	16-18	18-20	20-22	22-24
1-2	0	0	18	20	27	23	23	21	28	34	24	0
3-4	0	17	34	28	21	18	18	32	33	26	19	0
5-6	19	24	37	40	52	56	56	46	43	24	21	18
7-8	23	36	32	40	53	39	39	60	49	46	34	21
9-10	36	45	67	58	69	35	35	31	47	60	34	27
11-12	38	44	52	62	67	43	43	54	67	71	45	47
13-14	34	70	57	45	73	88	88	92	100	84	56	28
15-16	0	28	22	34	29	19	19	23	19	17	0	0
17-18	0	28	22	0	0	0	0	0	21	23	0	0
19-20	0	0	0	23	21	0	0	0	27	0	0	0
21-22	0	0	25	20	0	0	0	18	37	34	0	0
23-24	0	0	0	0	0	42	42	0	0	0	0	25
25-26	0	0	17	21	0	0	0	0	0	0	0	0
27-28	0	0	0	0	0	0	0	0	19	0	0	0
29-30	0	0	21	19	0	0	0	0	0	0	0	0
31-32	0	0	0	0	0	0	0	0	0	0	0	0
33-34	0	0	0	0	0	0	0	0	25	27	0	0
35-36	16	19	24	21	0	0	0	0	0	0	0	0
37-38	18	21	28	20	0	0	0	0	24	21	0	0
39-40	23	20	0	0	0	0	0	0	25	27	0	0
41-42	32	35	40	31	25	0	0	0	0	34	21	22
43-44	44	47	41	35	0	0	25	23	31	56	45	31
45-46	22	25	27	0	0	34	28	43	51	32	22	19
47-48	0	18	21	25	33	37	35	31	32	43	27	0
49-50	0	22	25	30	35	56	67	44	49	41	33	28
51-52	0	0	40	32	41	33	42	37	32	0	0	0

PV and BESS Resources

Several buses throughout the microgrids incorporate PV with on-site BESS resources. Each pair of PV and BESS resources on a bus is connected to each other and the grid through a two-way converter / charge controller allowing for both BESS charging from and discharging to the Bulk Power Grid (BPG). The diagram for this connection is shown in the description for bus modeling in the next section. The test system specification was not intuitively clear in [4] with

how specifications were defined across these three pieces of equipment. Therefore, a clearer identification of equipment ratings is shown in Table 2.10, and a plot of the implemented converter capability curve is shown in Figure 2.5.

Table 2.10. PV, BESS, and converter power ratings and reactive power limits, as applicable.

Bus	Converter			PV	BESS	
ID	P_{max} (kW)	Q_{min} (kVAR)	Q_{max} (kVAR)	P_{max} (kW)	Capacity (kWh)	P_{max} (kW)
102	2000	0	400	2000	3000	2000
103	2400	0	480	2400	4000	2400
104	2000	0	400	2000	3000	2000
202	1600	0	320	1600	4000	1600
203	1600	0	320	1600	4000	1600
204	2400	0	480	2400	4000	2400
303	2000	0	500	2000	3600	2000
304	400	0	100	400	800	400
305	800	0	160	800	2000	800
306	800	0	160	800	2000	800
307	800	0	160	800	2000	800
315	800	0	160	800	2000	800
405	1600	0	320	1600	3000	1600
406	2400	0	500	2400	6000	2400
407	1600	0	320	1600	3000	1600

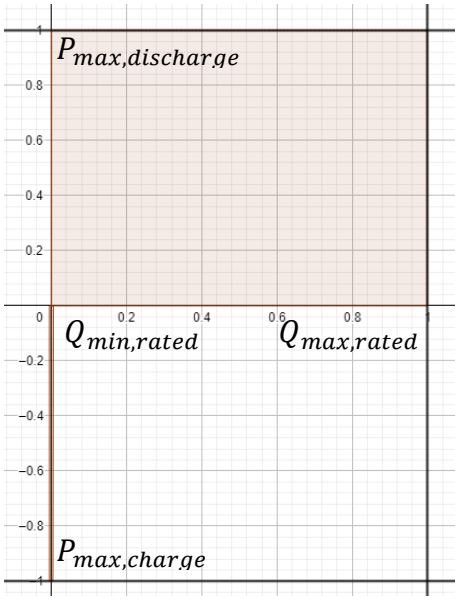

Figure 2.5. The assumed per-unit P-Q capability curve for converters with PV and BESS resources, where the converter can operate anywhere within the shaded region; when P is negative, the BESS is charging from grid resources; when positive, power is supplied to the grid.

Lithium-ion BESS are considered in this work which allows for an 80% DoD. Using this information within the converter, the battery State of Charge (SOC) and, consequently, the input/output powers can be managed. According to [4], efficiencies for charging and discharging the BESS are 0.95 and 0.92, respectively. Power ratings of the BESS are defined as maximum safe power output from the battery cells while discharging and maximum safe input power at the terminals during charging. Hence, efficiencies are factored into the model to affect BESS SOC. When charging, SOC changes according to Equation 2.6, and SOC changes by Equation 2.7 when discharging. γ is the charging/discharging efficiency; E_{BESS} is the capacity of the BESS; and P_{in} and P_{out} are battery input/output powers as viewed from the grid through the converter.

$$\Delta SOC_{charging} = \frac{P_{in} \times \gamma_{charging}}{E_{BESS}} \times \Delta t \quad \text{(Eq. 2.6)}$$

$$\Delta SOC_{discharging} = \frac{P_{out}}{\gamma_{discharging} \times E_{BESS}} \times \Delta t \quad \text{(Eq. 2.7)}$$

Like other DER's, failure rates and failure durations are needed for performing the time-based recovery simulation, and these values were not defined by [4]. The values considered for each of these parameters are shown in Table 2.11.

Table 2.11. PV, BESS, and converter failure rates and durations.

Bus ID	Converter		PV		BESS	
	Failure Rate (λ)	Failure Duration (hr)	Failure Rate (λ)	Failure Duration (hr)	Failure Rate (λ)	Failure Duration (hr)
102	**0.07008**	**8**	**1.0**	**20**	**0.120**	**12**
103	**0.08410**	**8**	**1.2**	**24**	**0.160**	**12**
104	**0.07008**	**8**	**1.0**	**20**	**0.120**	**12**
202	**0.05606**	**8**	**0.8**	**16**	**0.160**	**12**
203	**0.05606**	**8**	**0.8**	**16**	**0.160**	**12**
204	**0.08410**	**8**	**1.2**	**24**	**0.160**	**12**
303	**0.07008**	**8**	**1.0**	**20**	**0.144**	**12**
304	**0.01402**	**8**	**0.2**	**4**	**0.032**	**12**
305	**0.02803**	**8**	**0.4**	**8**	**0.080**	**12**
306	**0.02803**	**8**	**0.4**	**8**	**0.080**	**12**
307	**0.02803**	**8**	**0.4**	**8**	**0.080**	**12**
315	**0.02803**	**8**	**0.4**	**8**	**0.080**	**12**
405	**0.05606**	**8**	**0.8**	**16**	**0.120**	**12**
406	**0.08410**	**8**	**1.2**	**24**	**0.240**	**12**
407	**0.05606**	**8**	**0.8**	**16**	**0.120**	**12**

Failure rates and failure durations for converters rely on other equipment failure rates and the assumption the power electronics fail at a lower rate than mechanical systems. To this end, converters were assumed to fail according to equation 2.8, where the equation's constant is set to provide a failure rate one order of magnitude less than most mechanical equipment in the rest of the system. Failure duration is assumed to be constant regardless of power rating and is set to eight hours.

$$\lambda = 4 \times 10^{-9} \times 8760 \times (converter\ P_{max}) \text{ [f/yr]} \quad \text{(Eq. 2.8)}$$

PV resource failure rates were set according to data in [22], which reports solar panels fail at a rate of 5 out of 10,000 each year. Using this statistic and an assumption that every 1 kW of rated PV capability equates to one panel, failure rates for PV resources can be calculated according to Equation 2.9. Failure duration for these resources is set according to a target repair

time of one hour per 100 kW of rated capability to provide similar times to other equipment in this system; this calculation is shown in Equation 2.10.

$$\lambda = 5 \times 10^{-4} \times (PV\ P_{max}) \text{ [f/yr]} \quad \text{(Eq. 2.9)}$$

$$FD = 0.01 \times (PV\ P_{max}) \text{ [hrs]} \quad \text{(Eq. 2.10)}$$

BESS failure rate is based on Lithium-ion battery lifetimes and degradation, as mentioned in [23]. Using 80% DoD (i.e., for each cycle, the battery is discharged to its maximum safe extent), a minimum number of cycles for the battery lifetime is approximately 25,000 cycles. For a single cell with a capacity of 1 kWh and 25,000 cycles annually (less than three cycles per day on average), the cell would fail after one year, giving a scalable failure rate based on storage capacity of the BESS. The calculation for this value is shown in Equation 2.11. Like the converter, all BESS's have a single constant failure duration regardless of capacity at 12 hours to be consistent with other equipment failure rates in this system.

$$\lambda = \frac{1}{25000} \times \left(E_{BESS,\ rated}\right) \text{ [f/yr]} \quad \text{(Eq. 2.11)}$$

Finally, solar availability over one year defines a percent of rated PV generation availability as a function of both week of the year and hour of the day. This data is shown in Table 2.12 and is used as a lookup table for solar resource availability as the recovery simulation is performed.

Table 2.12. PV power available as percent peak rating by week of the year and hour of the day.

Week	Solar power generation (%) during sunshine hours (6AM – 6PM)											
	6-7	7-8	8-9	9-10	10-11	11-12	12-1	1-2	2-3	3-4	4-5	5-6
1-2	11	20	40	60	86	100	100	100	83	56	32	23
3-4	17	35	45	64	87	100	100	100	87	59	36	27
5-6	19	38	46	68	93	100	100	100	89	65	40	31
7-8	23	39	50	73	100	100	100	100	91	69	50	35
9-10	24	40	52	75	100	100	100	100	92	71	50	36
11-12	25	41	53	76	100	100	100	100	92	73	51	36
13-14	15	32	45	63	81	85	89	84	72	46	31	17
15-16	11	23	31	42	54	63	64	55	33	21	15	9
17-18	4	9	13	16	21	32	38	32	20	14	9	7
19-20	4	8	11	14	19	27	35	23	17	9	7	5
21-22	0	3	5	9	16	20	25	15	9	5	3	2
23-24	10	30	44	49	59	67	56	40	33	25	18	13
25-26	3	6	13	15	19	24	31	22	17	15	9	5
27-28	0	0	0	6	12	18	20	14	11	7	0	0
29-30	0	0	0	5	11	17	21	12	11	6	0	0
31-32	0	0	0	6	14	22	26	14	10	7	0	0
33-34	0	0	0	7	22	33	39	19	13	8	0	0
35-36	0	0	6	16	25	40	45	23	18	9	2	0
37-38	0	0	8	21	34	65	68	47	28	17	5	0
39-40	0	0	7	22	36	73	75	42	26	15	6	0
41-42	0	5	14	24	44	76	81	47	32	18	7	3
43-44	0	6	16	30	51	88	94	56	38	22	9	5
45-46	2	15	27	56	73	100	97	65	51	28	11	10
47-48	5	19	28	59	71	98	100	76	56	33	12	13
49-50	7	21	32	61	78	100	100	81	67	38	14	16
51-52	9	23	38	66	82	100	100	87	70	40	21	18

Buses Modeling

Buses have a fixed location within the simulated regional geography, and by linking equipment to a bus, loads, DER's, and lines are provided with a geographic location as well. Equipment is linked to the necessary buses according to the one-line diagram shown in Figure 2.2. Bus connections are shown in Figure 2.6. Simply stated, all loads of a given priority (i.e., standard loads vs. critical loads) on a single bus are linked together and can be connected or

disconnected via a single switch. Likewise, any DER's on a bus are connected to the bus through a switch that can isolate the equipment as necessary. The failure rate and outage duration are defined uniformly for all buses as 0.22 failures per year and 10 hours, respectively, according to [4].

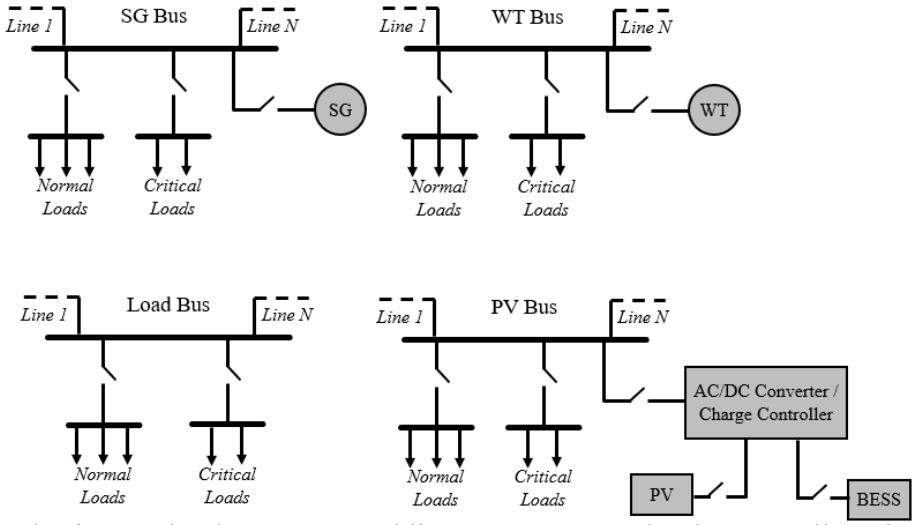

Figure 2.6. The basic way loads, DER's, and lines are connected to buses. All equipment can be disconnected independently depending on whether it fails or if other equipment around it fails.

This project aims to investigate a power system in a geographic layout. Therefore, the one-line diagram previously shown in Figure 2.2 needs to be translated into a two-dimensional geographic layout. Using the line data from Table 2.1, each bus can be placed relative to another according to line lengths and which buses a line connects. This task was completed manually such that all but four lines (PCC1-PCC4) obey their specified lengths. The resulting two-dimensional plot of buses and lines is shown in Figure 2.7.

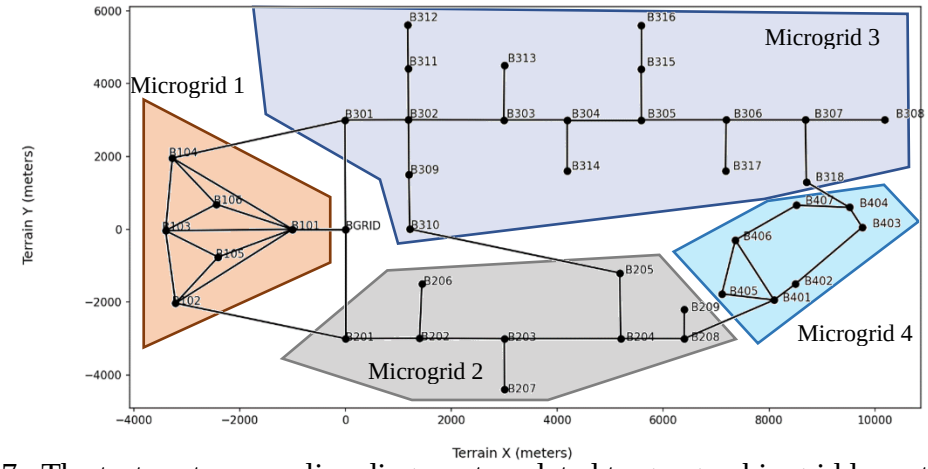

Figure 2.7. The test system one-line diagram translated to geographic grid layout. Each bus is labelled, and each microgrid is boxed. Terrain scale is 1:1m, so a coordinate change of 1 is 1 meter.

Regional Geography Modeling

To complete the system layout over geography, a regional terrain is necessary for overlaying the geographic bus map and simulating extreme weather. While real-world topographical data could have been acquired for use in this role, the regional geography was instead generated as an arbitrary normalized height map that could later be scaled and vertically shifted to represent a regional elevation profile.

The process of generating this terrain is straightforward. Using the width and height of the two-dimensional bus layout from before, a matrix of random values between 0.0 and 1.0 is loaded with slightly larger dimensions. Those values are then smoothed according to a gaussian blur algorithm until the statistical variance of height values across the region is below a desired threshold. The resulting regional height map is saved to a file for persistent use across all simulations, as will be discussed in chapter four. A three-dimensional example of a region map is shown in Figure 2.8, and the same region in two dimensions is shown in Figure 2.9.

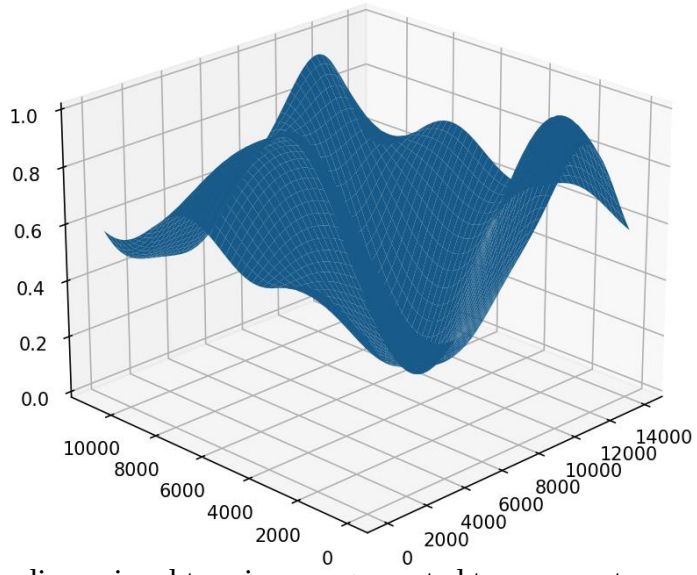

Figure 2.8. A three-dimensional terrain map generated to represent normalized regional topography where a geographically placed bus map would be located.

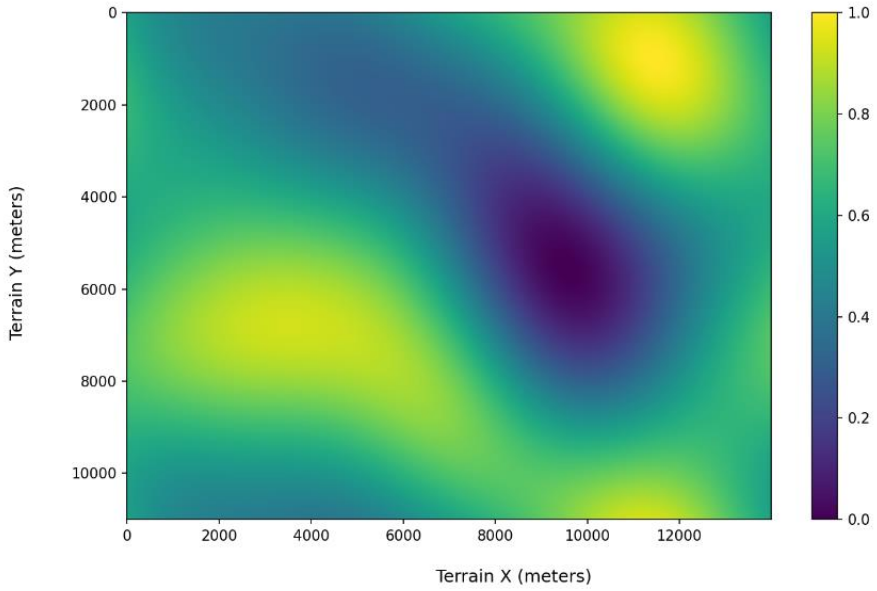

Figure 2.9. A two-dimensional terrain map generated to represent normalized regional topography where a geographically placed bus map would be located. Lighter colors represent higher elevations.

When overlayed on the generated geography, the geographic bus map would have line lengths that are no longer true to the line specifications, and those errors would only increase with more exaggerated regional elevation differences. Because the scope of this work is focused on equipment operability status and system recovery time, these errors are negligible. This improvement will be left for the future.

Extreme Event Simulation Basics

Once a physical grid layout and regional terrain map are available, a multitude of extreme events are simulated to impact the region and test a recovery strategy. To simulate an extreme event, three parameters are needed: event type, topography, and severity. These values are passed into the event simulator according to the block diagram shown in Figure 3.1.

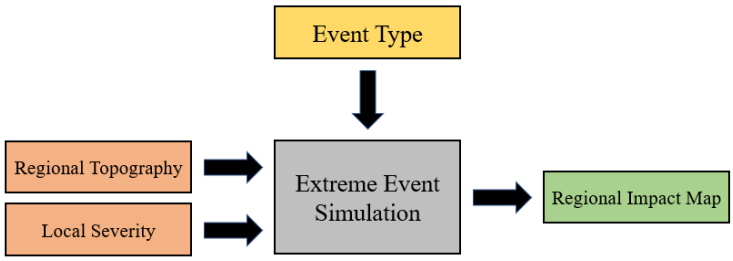

Figure 3.1. The extreme event simulation block diagram. Simulation accepts input parameters for extreme event type, regional topography, and event severity (on a scale 1-10) and outputs a two-dimensional normalize impact map representing probability of impact at any given coordinate.

The regional topography input to the extreme event simulator is a two-dimensional height map representing an arbitrary region's topography which is scaled and translated to represent true topographical heights in the region. This parameter sets the dimensions of the resulting impact probability map and contributes to the impact map's formation when an event type's simulation relies upon the regional topography.

The local severity parameter is a scalar integer between 0 and 10 representing the severity of the event to the local region. This severity definition was selected for this simulation due to recognition that the same type of event can impact different regions with different intensities; for

example, a flood in a region with a flat landscape may be more devastating with a smaller water level rise than a flood in a region with drastic elevation differences.

The event type parameter defines the type of extreme event that should occur. Four extreme event types were defined to be chosen from for this simulation: flooding, tornadoes, wildfire, and windstorms. For a flood, the severity factor defines the floodwaters' height; among tornadoes, severity identifies the diameter of the funnel across the ground; in wildfires, it defines the speed of fire spreading and the lifetime of flames; and, in windstorms, it identifies the magnitude of the wind speed across the ground.

The output of the event simulator is a two-dimensional map with the same dimensions as the regional topography input. This map contains normalized values that represent the likelihood of a point in the region to be impacted by the extreme event. For an arbitrary point, if the value on the event impact map is 0.5 or 1.0, the event is said to have a likelihood of 50% or 100%, respectively, of impacting that point. This impact percentage is utilized later during the electrical system degradation process to help identify whether a piece of equipment was damaged from an extreme event. This process is covered in more detail in chapter four.

Four extreme events were specified in this work. Each of those and the methodology behind their design will be described in subsequent sections. Sample outputs will also be included.

Flood Simulation

To generate the impact probability map, a water level is selected based on the event severity parameter passed to the extreme event simulator. Equation 3.1 provides a mathematical formula for evaluating the impact of a flood for given water level on a point (x, y). In this

equation, H(x, y) is the topological height of the terrain and W is the elevation the water level reaches.

$$I(x, y, W) = \frac{1}{1+e^{4*(H(x,y)-W)-1}} \quad \text{(Eq. 3.1)}$$

The impact function utilizes a logistic function to enable a blurring of the boundary between absolute impact and absolute non-impact in order to model edge effects such as soil saturation that can cause destabilization of equipment foundations. The height the water level reaches, W, can be calculated based on the local severity parameter according to Equation 3.2.

$$W(severity) = \frac{severity}{10} \times \left(\max\big(H(x,y)\big) - \min\big(H(x,y)\big)\right) \quad \text{(Eq. 3.2)}$$

An example of a flood over a small region with a severity of five is shown in Figure 3.2. In this example, the logistic function's blurring effect is obvious in certain regions.

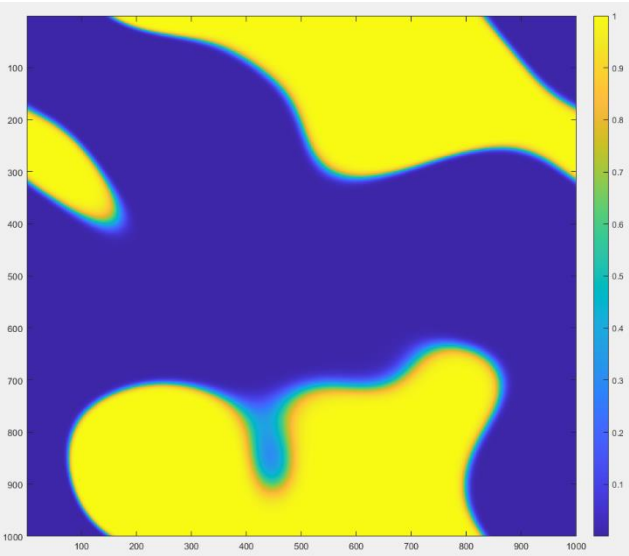

Figure 3.2. A severity-5 flood event simulated over a 1000x1000 sample terrain. Yellow regions are areas of high impact probability; purple regions are low-probability regions.

Tornado Simulation

To simulate how tornadoes would affect a region, the first step is to consider how one might move. Over flat terrain, a tornado is considered to move in an approximately straight line with velocity directly related to that of the weather above it. Because the region being simulated has depth, the driving factor for tornado motion became how tornadoes move relative to hills and terrain changes; this information came from [24] which describes how tornadoes tend to move uphill.

With tornado motion basics identified, the effect of local severity factor is established as modifying the radius of impacted area off a central point. To accomplish this, a gaussian function is used to define probabilities of damage away from the central (x, y) location of the tornado. The radius of the gaussian is set as a linear range from 0 meters (0 severity) to 300 meters (10 severity), with the radial standard deviation of the gaussian as one quarter the radius of impact. This gaussian function is used to produce a matrix of weights summing to 1.0 that would additively modify the impact map at each iteration of the event simulation. Hence, the longer a tornado sits over a particular point, the greater the impact probability to that location.

To perform the tornado simulation itself, a random point (x, y) is chosen on the topography, and the tornado is given a random velocity magnitude in a random direction. In each simulation iteration, the tornado moves according to its current velocity and adjusts that velocity based on the landscape gradient in addition to a random vector. The simulation lasts for 1000 iterations or until the tornado moves outside the region. Through this methodology, a tornado centered at a point would move across the landscape with a biased random motion

according to the region's topography. Two examples of a tornado's path across a test region are shown in Figure 3.3, both with a severity value of 10.

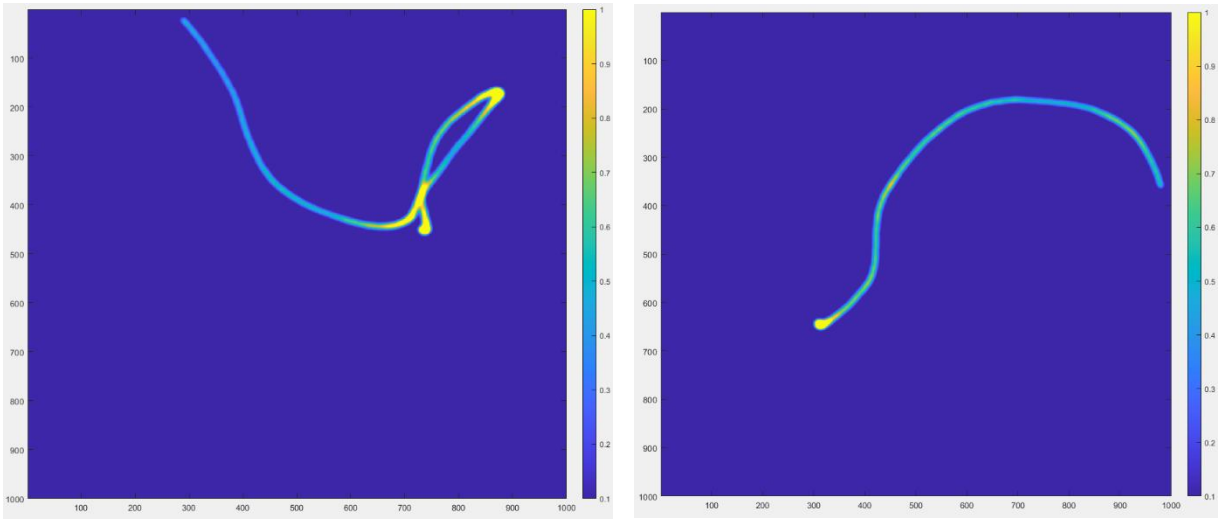

Figure 3.3. Two severity-10 tornado events simulated over a 1000x1000 sample terrain. Yellow regions have high impact probability; purple regions have low impact probability.

Windstorm Simulation

To model a windstorm, how wind behaves over a terrain must be understood. Based on information from [24], wind is more damaging on the windward side of an obstacle than the leeward side, which is intuitive to anybody who has walked in a field with hills on a windy day. Therefore, the objective through the event simulation is to trace the path of the wind and increase impact probabilities for a coordinate if the elevation is trending upward and slowly decrease impact probability as the terrain trends downward.

The local severity value defines the baseline impact probability (if the terrain was flat) according to Equation 3.3. It also defines the magnitude of the wind speed.

$$I_b = 16 + 6 * severity \text{ [\%]} \qquad \text{(Eq. 3.3)}$$

To perform the simulation itself, a random angle is chosen to define the vector through which wind flows. Using this vector, a "ray tracing" methodology is employed to collect coordinate pairs along the wind vector through which a straight line would follow. The impact probabilities are assigned based on these points for elevation profile changes as the wind propagates through the terrain. For every unit increase in elevation, the impact probability increases by 2% of the elevation change up to 100% impact. For every unit decrease, the impact decreases by 1% the elevation change down to the baseline impact probability. For no change, the impact reduces by 0.5% per point. This process is repeated until all points in the impact map have values assigned according to this process. An example of this algorithm's result is shown in Figure 3.4.

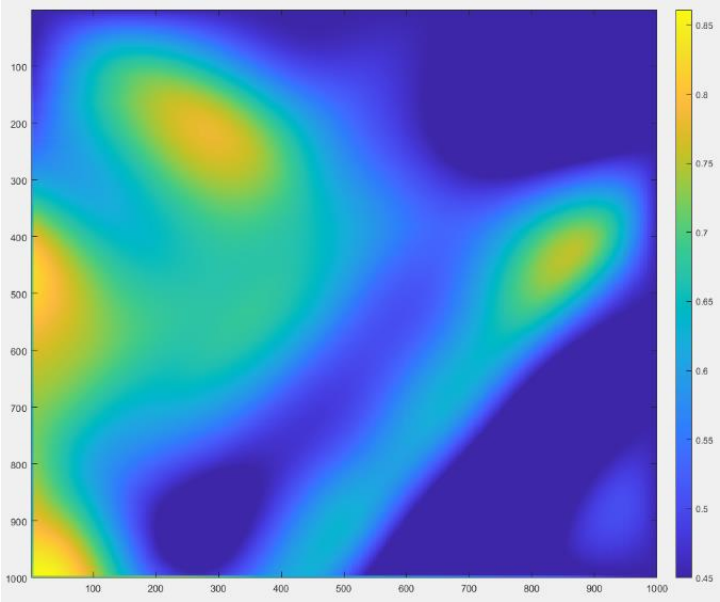

Figure 3.4. A severity-5 windstorm simulated over a 1000x1000 sample. Yellow regions have high impact probability; purple regions have low impact probability. For this example, wind is streaming from top right to bottom left.

Wildfire Simulation

Spurred in part by the numerous fires in California over the past several years, this event is a worthwhile addition to the extreme event simulations. The primary principles are fire spreads uphill faster than it does downhill; embers flying through the air can start new fires away from the source of those embers; and the longer a fire burns, the more likely it is to be extinguished by firefighters, nature, or consumption of fuel.

Due to the complexity of the event, severity drives several aspects within the simulation execution, including number of initial fires, lifetime of all fires, probability of spreading up and down hills, probability of spreading indirectly through embers, maximum number of concurrent fires, and radius of indirect fire spread. The way in which these factors are impacted by severity are shown in Table 3.1.

Table 3.1. Wildfire simulation features and local event severity impact during execution.

Simulation Feature	Description
Initial number of Fires	$count = 2 + severity$; $spawn\ radius = round\left(\frac{ceil(\sqrt{severity+2})}{2}\right)$
Lifetime of each fire	Random, normally distributed with mean of (10 + severity) simulation iterations
Probability of uphill spread	$\max(15, 4 \times severity)$ [%], experimentally determined based on simulation results
Probability of downhill spread	$\max(8, 2.5 \times severity)$ [%], experimentally determined based on simulation results
Probability of indirect spread	$\max(10, 4 \times severity)$ [%], experimentally determined based on simulation results
Maximum number of fires	$150 \times severity$
Radius of indirect fire spread	$round(\max(3, 0.0003 \times severity \times \min(topography\ dimension)))$

This simulation is performed for 1500 iterations or until all fires are extinguished. At each iteration, each fire has a chance of spreading directly to an adjacent coordinate point if that point can burn, spreading indirectly to a nearby point that can burn in a radius defined in Table 3.1, or being extinguished. Whether any or all these events occur is determined by a random number compared against the probability of fire spread (defined in Table 3.1) or probability of fire extinguishing, defined by Equation 3.4.

$$P_{extinguish} = \max\left(0, 0.8 - \frac{remaining\ fire\ lifetime}{total\ fire\ lifetime}\right) \qquad \text{(Eq. 3.4)}$$

At each simulation iteration, an active fire at a point adds 1% impact probability to that point; if this impact probability reaches 100% before the fire is otherwise extinguished, the fire is extinguished, having assumed it has burned all its available fuel at that point. An example of a result from this simulation is shown in Figure 3.5 for a severity 10 wildfire.

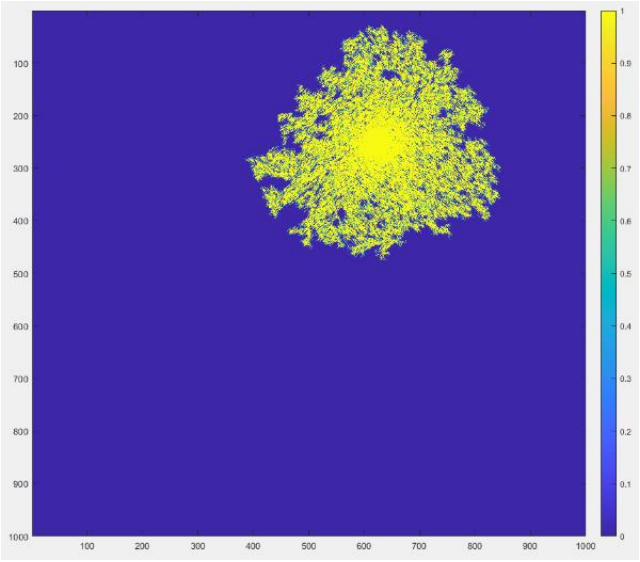

Figure 3.5. A severity-10 wildfire simulated over a 1000x1000 sample. Yellow regions have high impact probability; purple regions have low impact probability.

SIMULATION RUNTIME

Process Introduction

The previous two chapters detailed equipment and extreme events modeling. This chapter focuses on how those components tie together to produce a simulation that can output meaningful results. The high-level simulation process is shown in Figure 4.1. Key aspects of this work include loading the system configuration from files, building a simulation instance with a specific regional topography and extreme event impact probability map, evaluating the extreme event degradation to the test system, and performing a repair process. Each of these aspects are discussed in greater detail in the following sections.

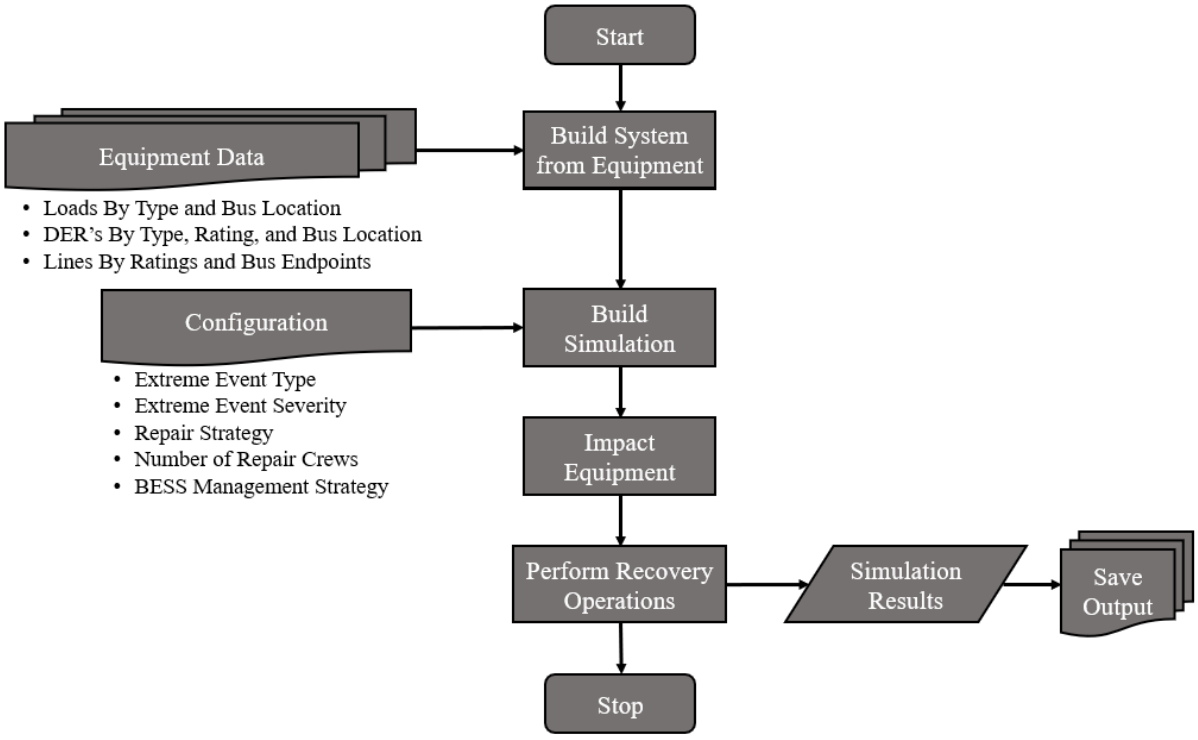

Figure 4.1. The high-level sequence of steps in the extreme event system recovery simulation.

Several steps in the simulation process also include variation that determines how many specific equipment are impacted and how fast the system recovers. For this purpose, a Monte-Carlo simulation is performed by executing the simulation process repeatedly and saving simulation results for later analysis according to the process outlined in Figure 4.2. This process will be discussed later in this chapter as well.

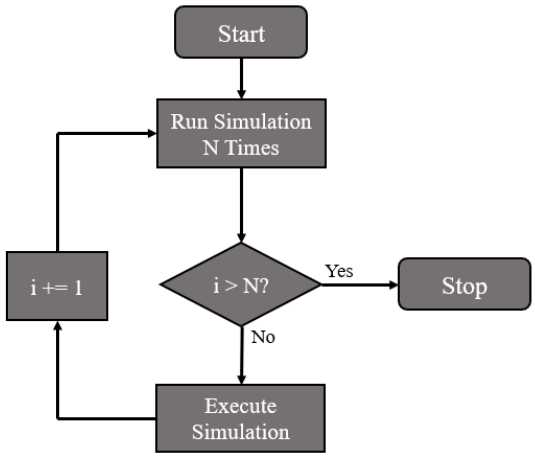

Figure 4.2. The sequence of steps in a Monte-Carlo execution of the extreme event system recovery simulation.

Building the System from Equipment Specifications

The tables of data discussed throughout chapter two contain all the configuration data required to instantiate equipment and construct the aggregate system model. A flow chart representing the process of loading all data for system initialization is provided in Figure 4.3. First, all buses and loads are instantiated for the system according to Table 2.3. With buses added, the lines connected those buses can be included according to the specifications in Table 2.1. The last equipment required are DER's, which are added according to Tables 2.7, 2.8, 2.10, and 2.11. Finally, the relative locations of all buses with respect to the utility substation placed

at the origin are loaded from the manually created coordinates that define the bus locations shown in Figure 2.7.

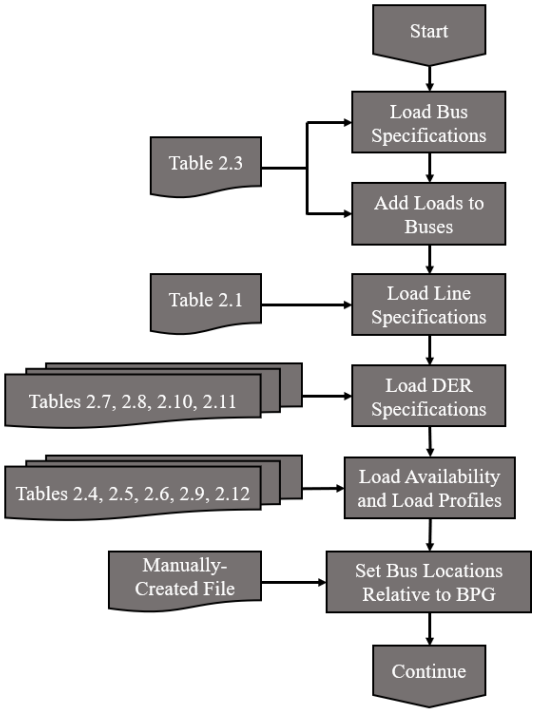

Figure 4.3. The steps taken during construction of the simulated power system according to specifications defined in chapter two.

Building the Simulation

Once the system of equipment is created, the simulation environment can be set up. The flow chart of processes performed during this stage is shown in Figure 4.4. Key stages in this process are creating the simulation manager instance, creation of a regional topography, overlaying the system equipment on that topography, simulating the extreme event that will degrade the system, establishing the initial times in operation for all equipment, and setting the initial status of charge of all BESS's in the system. Some of these steps have already been discussed in earlier chapters, such as the generation of a region topography and simulating extreme events; these processes will not be redescribed in this section.

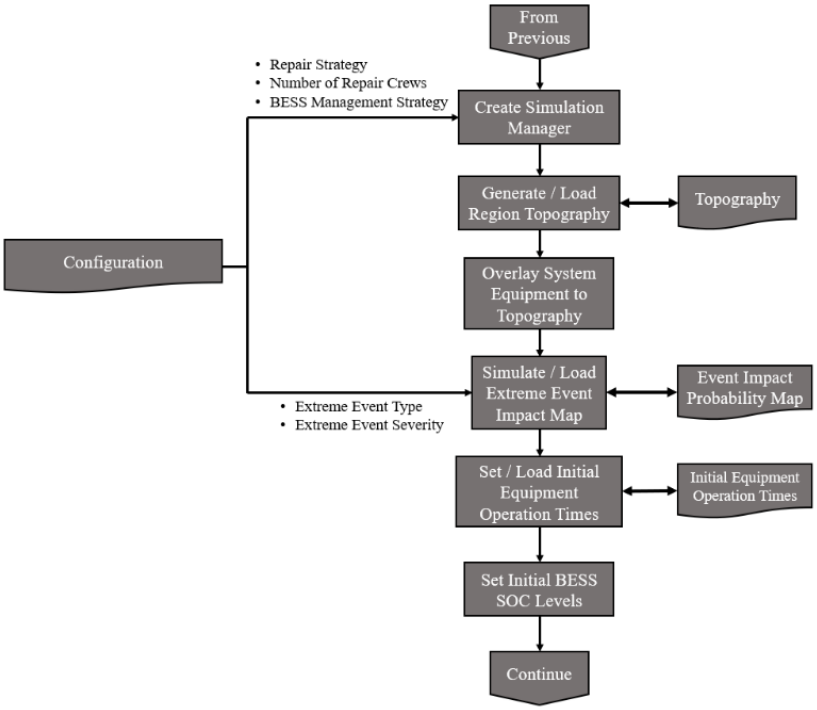

Figure 4.4. The steps taken during construction of the simulation profile according to configuration parameters defined by the user.

Persistent Data

In this stage of simulation execution, a "runtime profile" is generated based on the user-defined configuration parameters for repair strategy, number of repair crews, BESS energy management strategy, extreme event type, and extreme event severity. For a unique combination of these five parameters that has yet to run, a series of persistent values are generated and saved to enable repeated execution with these simulation aspects maintained. This action allows fundamental aspects of a system to remain constant (region topography, extreme event impact probability map, initial equipment operating times at the time of extreme event occurrence), while other aspects vary depending on system degradation and in-service failures during recovery, among other aspects.

Creating the Simulation Manager

The simulation manager supervises all strategic aspects of the simulation execution. Based on the combination of the five previously mentioned parameters which the user specifies, the simulation manager creates and oversees repair crews, ensuring they obey the requested repair strategy, maintains the given BESS energy management strategy, and produces a record of each system component's performance and behavior during the recovery simulation. This process also is responsible for generating the regional topography and extreme event impact probability map according to the specified geographic bus layout and extreme event type and severity. The relevant sub-components to the simulation manager are shown in Figure 4.5.

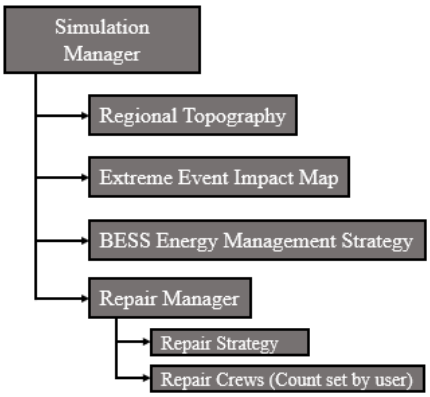

Figure 4.5. Key recovery simulation components supervised by the simulation manager object.

One source of variation between different executions of this simulation manager creation is the introduction of a 'skill' parameter to the repair crews' initialization. This parameter is normally distributed with a mean of 1.0 and standard deviation of 0.05 and acts a scale factor to either reduce or lengthen the repair time of equipment to which the crew is assigned. While this factor has a minor impact on the overall recovery time of the system, it allows for additional variation that allows the recovery profile to resemble more closely what could be a real system's recovery after an extreme event.

Overlay the Grid on Regional Topography

Once the simulation manager is created, a map of bus placements relative to the utility substation is available, and the regional topography is generated, the bus locations need to be placed over the topography. Because the dimensions of the topography are derived from the bus locations, this process is as simple as adding offsets to the x- and y-dimensions of bus locations such that the geographical bus map is centered over the region topography. The resulting bus model overlayed on the terrain is shown in Figure 4.6, where the terrain elevation profile is shown as a normalized height map under the system overlay.

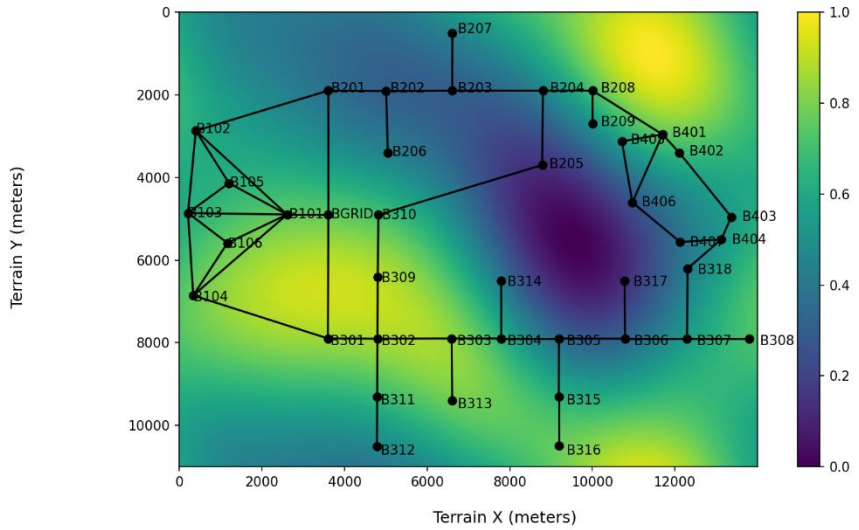

Figure 4.6. Geographic bus placement overlayed on the region topography; topography is shown as a normalized height map with 0.0 as minimum local elevation and 1.0 as maximum.

Set Equipment Initial Time in Service

Because the recovery simulation is based on system evolution over an unknown length of time, one factor which must be considered is the diminishing reliability of equipment with time in service. The implementation of this during the system recovery process is described in greater detail in the “Recovery Process” section of this chapter. In is stage of simulation initialization,

the initial conditions for equipment time in service at the time of extreme event occurrence are loaded from a previously existing configuration or generated if that configuration is missing.

The objective of this process is to produce a system that more closely resembles equipment reliabilities that might be found in a distribution system. To accomplish this, a uniformly distributed random reliability value between 80 and 99% is chosen. This range of values is selected with the assumption that preventive maintenance on equipment is performed before its reliability falls below 80% and that some equipment in the system might be due for maintenance when the extreme event occurs. A time in service can then be calculated using this target reliability value and a component's failure rate according to Equation 4.1. This equation is simply a re-arrangement of the constant failure rate reliability equation shown in Equation 4.2 with a variable substitution for time in hours instead of years.

$$t = round(\max\left(0, -\frac{1}{\lambda} \times \ln\left(R_{target}\right)\right) \times 8760) \text{ [hrs]} \quad \text{(Eq. 4.1)}$$

$$R(t) = e^{-\lambda t} \quad \text{(Eq. 4.2)}$$

Once generated for the first time, these values are saved as persistent data to provide common initial conditions for equipment from which all simulations can be performed and ultimately compared with the help of Monte-Carlo simulation techniques.

Set BESS Initial SOC

The final stage in simulation initialization is setting the SOC for all BESS's in the grid. This step introduces some variation that can exist between simulation executions with all other user configuration input held constant. For simplicity, an independent, random value is chosen between the minimum SOC of the BESS (defined as 100% - DoD) and 100%. These random

values are distributed uniformly throughout this range and are meant to represent varying degrees of resource availability within BESS's at the start of a recovery simulation.

System Degradation from Extreme Event

Since all equipment are loaded and geographically located, simulation parameters are initialized, initial conditions are set, and the extreme event is simulated. The last remaining step before beginning the system recovery / restoration simulation is calculating system degradation due to the extreme event.

To begin this process, a damage probability threshold value is calculated for all equipment in the system according to Equation 4.3. In this equation, $P(D)_{x, y, type}$ is the probability of failure based on equipment type and location (x, y), R and F are equipment reliability and unreliability, respectively, $P(I)_{x, y}$ is the probability of extreme event impact at geographic point (x, y), and $P(F|I)_{x, y, type}$ is the probability of failure given extreme event impact at geographic point (x, y) and the type of equipment being impacted.

$$P(D)_{x,y,type} = F + R \times P(I)_{x,y} \times P(F|I)_{x,y,type} \quad \text{(Eq. 4.3)}$$

The structure of this equation is selected because a piece of equipment not impacted by an extreme event can still fail according to its failure rate and the time in service determining its reliability. Any additional failure probability greater than the equipment's unreliability would stem from the extreme event impact. The value of $P(I)_{x, y}$ in Equation 4.3 is determined by the extreme event impact probability map generated as the output of the extreme event simulation described in chapter three. $P(F|I)_{x, y, type}$ identifies the likelihood of individual equipment to experience damage from the extreme event based on unique extreme event features at a given location and the type of equipment. For example, in a flood event, the probability of failure of

buses and overhead lines can depend on clearance between conductors and the water level and what type of debris is suspended in the water. Likewise, equipment such as underground cables may not be impacted at all from a flood since these are commonly designed to operate below a region's water table. For all equipment besides lines, $P(F|I)_{x, y, type}$ is a single value based on the equipment's location; for lines, this value is taken as the maximum impact probability for a series of sample points evaluated along the length of the line from its origin bus to the destination bus.

With equipment damage probabilities specified, a single, uniformly distributed random variable between 0.0 and 1.0 is selected to degrade the entire system, representing the extreme event's overall impact to system degradation. The selection of this value is the second point of variation between multiple executions of the same simulation configuration and using Monte-Carlo simulation. Many iterations of this process can be performed to find the most likely system degradation due to an extreme event. An example of a system degradation map due to a severity-5 flood is shown in Figure 4.7, where green equipment is operating normally, red equipment is failed, and black equipment is disconnected.

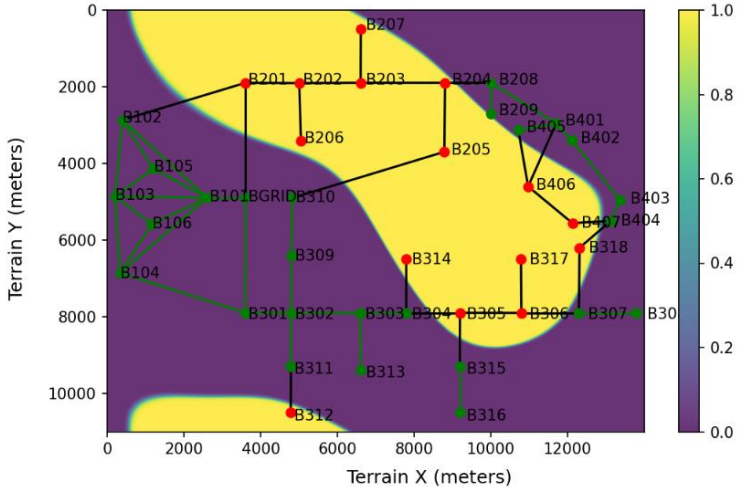

Figure 4.7. Example system degradation due to a severity-5 flood event. Red equipment is failed; green equipment is operating normally; and black equipment is disconnected.

Recovery Process

The recovery simulation process is a sequence of actions performed repeatedly from an initial time when the extreme event degrades the system until the time at which all equipment in the system returns to an operable state, regardless of how long that process takes. Considering the worst-case scenario for power generation and demand analysis, the simulation assumes that all loads in the system are attempting to draw their normal load profile worth of power from the grid throughout the entire recovery process; while reality would suggest some loads would be reduced or eliminated until customers recover from the event. This simulation is interested in finding the average upper limit to load curtailment due to generation resource losses from the extreme event.

The recovery process starts by establishing what hour of the year the extreme event occurred. This, like other aspects of the setup process for the recovery simulation, introduces variation to the recovery in the form of different generation profiles on WT and PV resources. After selecting the hour of year, all operable but disconnected equipment (such as interconnects or common connection lines initialized as disconnected) are reconnected to pool generation resources and supply loads wherever possible.

Throughout the recovery simulation, key statistics for all equipment are logged to include the equipment operation status, hour of the year, time in service, time out of service, and equipment reliability; each equipment type has some unique parameters as well, including loads supplied and loads not supplied at each bus. Once the simulation concludes and all equipment is once again operational, these records are saved to later calculate resilience metrics (chapter five)

and determine the most likely system resilience metrics based on the results of a Monte-Carlo simulation with many of these simulation procedures.

Recovery Iteration Procedure

One iteration of the simulation executes for each hour in the recovery process. During this loop, the islanding of the grid is calculated based on buses or groups of buses and lines that are in service but disconnected from the overall system. For each of these islands, a curtailment strategy is calculated to determine which loads will be energized and which will not when generation resources are scarce.

In calculating curtailment, BESS resource dispatch is first determined according to the user-defined BESS energy management strategy passed in via runtime configuration. An example strategy uses the dispatch model that when demand is greater than the available generation without BESS's, discharge as much as necessary to cover the difference, up to the maximum BESS output or maximum discharge power that would result in depletion of the BESS over the next one hour. Otherwise, when generation is greater than demand, charge the BESS with the surplus, up to the maximum rating of the BESS or the power that would result in a fully charged BESS over one hour. By this strategy, additional energy resources can be acquired prior to curtailment strategy calculation. The load is curtailed based on the load's priority. By default, critical loads are the first to be supplied when generation is available and the last to be curtailed if necessary. The load supply priorities utilized in this simulation include smallest to largest critical to normal loads and largest to smallest critical to normal loads by apparent power demand; whichever of these two priority lists supplies more power is the prioritization used for curtailment.

After incrementing the simulation time, BESS SOC is updated to reflect the total remaining energy change based on a 1-hour power charge/discharge rate modified by the charge/discharge efficiency. Subsequently, in-service equipment failures are calculated based on the equipment reliability (determined from time in service) and a random number chosen from a highly skewed normal distribution; an example of this distribution's probability point function is shown in Figure 4.8.

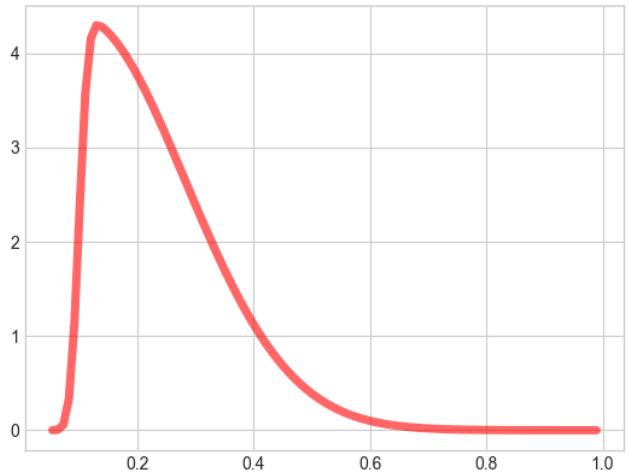

Figure 4.8. The highly skewed normal distribution used for producing in-service failures of equipment during recovery runtime. Skew value is 15 with a scale of 1/5.5 on the x-axis and horizontal shift of 0.1.

Simulating this distribution of random values 10,000 times for one piece of equipment over one year (8760 hours) results in average probabilities of values greater than 0.7, 0.8, and 0.9 shown in Table 4.1. This means that while the probability of highly reliable equipment failing is low, it can still happen and add additional variation to the recovery simulation execution similar to what could happen if this was a real-world recovery procedure.

Table 4.1. The highly skewed normal distribution used for producing in-service failures of equipment during recovery runtime. Skew value is 15 with a scale of 1/5.5 on the x-axis and horizontal shift of 0.1.

Reliability Threshold [R]	P(Value > R) [%]
0.7	0.0967
0.8	0.0118
0.9	0.0011

The final step in the recovery simulation is processing system repairs. As discussed in the section titled "Building the Simulation" earlier in this chapter, the system configuration defines a repair strategy and number of crews to handle repairs. During a recovery iteration, any crews not assigned to a repair task are assigned according to the prioritization list defined by the repair strategy. Once assigned, the repair time of the equipment is calculated according to a normally distributed random variable with a mean at the equipment failure duration and standard deviation of 10% the failure duration. Therefore, the repair time for a piece of equipment is most likely to range between 0.7 and 1.3 times the specified equipment failure duration. Once this repair time has elapsed with a repair crew working on the equipment, the equipment is put back into normal operation.

Monte-Carlo Simulation

The procedure defined throughout this chapter contains multiple sources for random variation that affects the recovery profile of the system: BESS SOC initial levels, system depth of degradation, hour of year at which the simulation starts, repair crew skill, time to repair a failed piece of equipment, and any variation otherwise utilized for specific recovery strategies. To reduce the effects of these variations and determine what the most likely recovery of this

system with a given configuration is, Monte-Carlo simulation is implemented. To utilize this simulation strategy, thousands of simulations were performed for several different system configurations. The statistics used to gauge system resilience are defined in the next chapter, and the results of this Monte-Carlo simulation are discussed in chapter six.

RESILIENCE METRICS

Metrics Summary

Several resilience metrics were defined to evaluate the performance of a recovery simulation. These metrics are partially based on reliability indices to allow an observer's familiarity with reliability indices to help to help introduce what the values are meant to represent; the names of the metrics reflect this similarity or are otherwise meant to be self-explanatory. These calculations measure key features of the recovery process, namely how severe the system damage was, how long the recovery lasted, how fast the system recovered, and how well the system accomplished the goals of supplying power to customers during the recovery. Each metric and the formula to calculate it are described below.

System Recovery Time (SRT)

This metric is simply the measure of how many hours the recovery simulation lasted, from t=T_0 being the time the extreme event finished degrading the system and recovery could begin until t=T when the final piece of equipment returned to normal operation. The formula for this is shown in Equation 5.1. The value for this metric is influenced primarily by the number of equipment failures due to the extreme event, the number of repair crews working to restore the system, and whether in-service failures were experienced during system recovery.

$$SRT = \int_{T_0}^{T} dt \text{ [hrs]} \qquad \text{(Eq. 5.1)}$$

Equipment Impact Percentage (EIP)

This metric is the ratio of failed equipment due to the extreme event and total equipment count in the system, excluding loads. This metric is expressed as a percentage and is intended to gauge the system degradation severity due to extreme event impact. This value is primarily affected by the extreme event type specified in the simulation configuration, the severity of the extreme event, and the random number chosen to degrade the system. The formula for calculating this is shown in Equation 5.2.

$$EIP = \frac{N_f}{N} \times 100 \text{ [\%]} \quad \text{(Eq. 5.2)}$$

Equipment Degradation-Recovery Rate (EDRR)

This metric provides a measure of how rapidly the system recovers, on average. The primary influencing factors for this metric are the number of repair crews restoring the system. The formula for this metric is provided in Equation 5.3.

$$EDRR = \frac{EIP}{SRT} \text{ [\%/hr]} \quad \text{(Eq. 5.3)}$$

Energy Not Supplied (ENS)

As the name suggests, this metric calculates the total energy shortage over the recovery time by integrating power shortage for all N_L buses over the recovery time $T\text{-}T_0$. The power shortage is defined as the apparent power demand of operable loads less the apparent power demand of loads actively supplied. This metric can be extended to apply strictly to critical loads (denoted as ENS_C) by considering only operable and active critical loads instead of all loads. This metric can be assessed at both the bus level as well as at the system level and is primarily

impacted by how quickly loads are reconnected and generation meets demand. Hence, repair strategy, number of repair crews, and BESS energy management strategy affect this metric. A formula for this metric is provided in Equation 5.4.

$$ENS = \sum_{k=1}^{N_L} \int_{T_0}^{T} S_{O,k}(t) - S_{A,k}(t)\, dt \text{ [kVAh]} \quad \text{(Eq. 5.4)}$$

Average Power Not Supplied (APNS)

This metric measures the average power (in kVA) not supplied to loads across the evaluation region; like ENS, this metric can apply to both individual buses and an entire system. If ENS_C is used to calculate this metric, it becomes the average power not supplied to critical loads, denoted as $APNS_C$. The formula for calculating this is shown in Equation 5.5.

$$APNS = \frac{ENS}{SRT} \text{ [kVA]} \quad \text{(Eq. 5.5)}$$

Energy Supplied Ratio (ESR)

This is a measure of how effectively energy was supplied to N_L loads, as a ratio of total energy supplied to total energy demanded. Like ENS and APNS, this measure can be directed toward only critical loads and is denoted as ESR_C when this is the case. It applies for both single-bus analysis or the entire system. The formula for ESR is shown in Equation 5.6.

$$ESR = 1 - \frac{ENS}{\sum_{k=1}^{N_L} \int_{T_0}^{T} S_k(t) dt} \quad \text{(Eq. 5.6)}$$

Average System Service Availability Index (ASSAI)

This index is based on the Average Service Availability Index from reliability analysis and is generalized for resilience to represent the ratio of customers actively supplied with power

to the total number of customers at each of the N_L buses, averaged across all buses and throughout the recovery duration. As with other metrics, this can be applied to only critical customers and is denoted as $ASSAI_C$ when this is the case. The formula for calculating this is shown in Equation 5.7.

$$ASSAI = \frac{\int_{T_0}^{T} \frac{1}{N_L} \sum_{k=1}^{N_L} \frac{N_{C,A,k}(t)}{N_{C,k}(t)} dt}{SRT} \quad \text{(Eq. 5.7)}$$

SIMULATION RESULTS

Source of Results

For the sake of simplicity and brevity in this report, all simulation results discussed in this chapter relate to Monte-Carlo simulation results performed with four constant configuration parameters while varying the repair crew count, as described in Table 6.1. A severity-5 flood is selected due to its significant impact across the regional topography and how it isolates sections of the grid from each other; a map of this extreme event and its most common impact to the test system is shown in Figure 6.1. BESS management is performed to prefer a 100% SOC whenever possible, delivering power to loads only when there is a generation shortage. The repair strategy utilizes a blind-pick method of prioritization, meaning equipment priorities are selected randomly without any preference to repairing specific lines or connecting islanded sections of the grid.

Table 6.1. Simulation configuration parameters for which simulations were performed. In this series of simulations all parameters except repair crew count are held constant.

Parameter	Simulated Value(s)	Description
Extreme Event	Flood	A flood event occurs in the region where water levels rise above the minimum regional topographical elevation.
Event Severity	5	A level 5/10 flood occurs; water levels rise to cover 50% of the elevation difference in the region.
Repair Strategy	Blind Pick	No preference to equipment type / loads / topology / etc. is made; prioritize equipment repairs by random selection.
Repair Crew Count	1 – 6	Run simulations to test the effects of crew size on repair time, using 1 to 6 crews to concurrently repair equipment.
BESS Energy Management	Prefer 100% SOC	Charge BESS when generation > demand; discharge BESS when demand > generation.

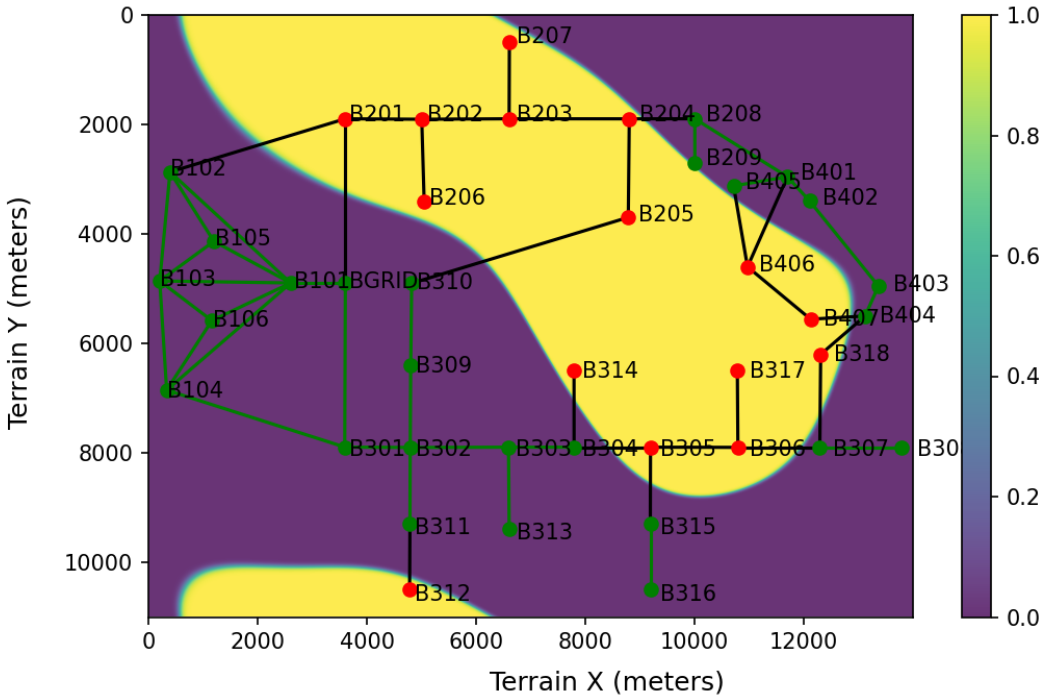

Figure 6.1. A severity-5 flood event impact map overlayed and demonstrating the most common impact to the test system.

The next section in this chapter will discuss trends in each resilience metric based on changes to repair crew count. Histogram plots showing the statistical occurrence of resilience metrics for the Monte-Carlo simulations of 1-6 repair crews are shown in Appendices A-F, respectively, at the end of this report. Included on all these plots are vertical lines where the statistical mean (red) and median (green) values lie for the data sets.

Most histogram plots of the Monte-Carlo simulation results follow a skewed normal distribution. This distribution is not unexpected considering how system degradation is performed to account for equipment reliability; if a random number is generated that causes all equipment in the system to fail, including those which were not directly impacted by the extreme event, outlier statistics will be generated in the results. These outliers will, in turn, pull the mean value of the resilience metrics away from the center of the distribution with highest frequency of

similar results. Therefore, the median value of the Monte-Carlo results will be taken to represent the measure of central tendency in each simulation series when determining the most likely resilience metric quantity. An example of one of these outlier system degradation maps is shown in Figure 6.2.

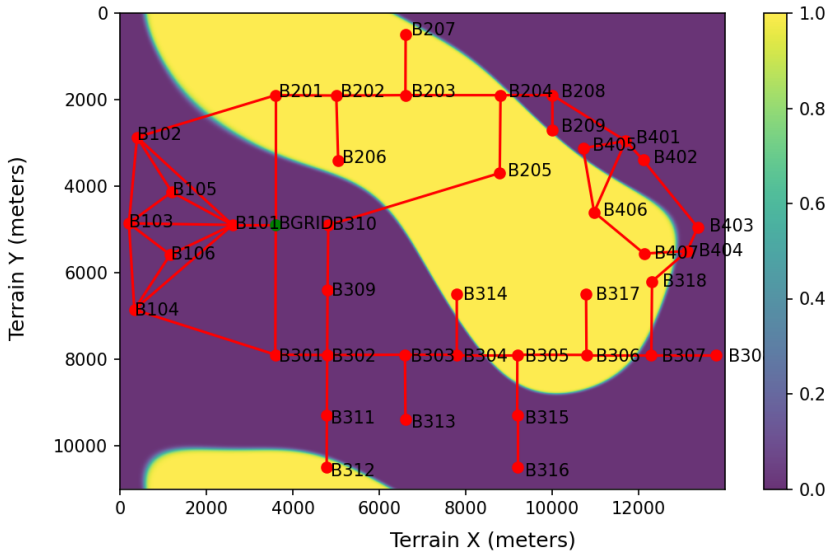

Figure 6.2. A severity-5 flood event with system degradation as an outlier occurrence to the expected model of event impact.

Trends Across Metrics

The individual Monte-Carlo simulation statistics become less important to overall results once the measure of central tendency converges for all metrics. The median values for each resilience metric according to repair crew size are shown in Table 6.2. Plotting these values reveals several unsurprising trends, which are plotted with mean (red) and median (green) values. Each plot of resilience metric trend is shown and discussed in the following subsections.

The plots and include error bars extending above and below the mean value by one standard deviation to provide context for the variance of the resilience metric values.

Table 6.2. Median resilience metric values for various Monte-Carlo simulation results according to different system repair crew sizes.

Resilience Metric (Median Value)	Repair Crew Size					
	1-Crew	2-Crews	3-Crews	4-Crews	5-Crews	6-Crews
SRT [hours]	371	190	136	109	95.5	86
EIP [%]	17.69	17.69	17.69	17.69	17.69	17.69
EDRR [%/hour]	0.0475	0.0930	0.1318	0.1659	0.1944	0.2184
ENS [kVAh]	2,145,892	1,068,834	721,532	543,322	441,770	376,212
ENS_C [kVAh]	528,422	260,273	177,323	133,392	108,690	90,900
APNS [kVA]	5900.5	5755.2	5514.6	5177.5	4839.5	4644.5
$APNS_C$ [kVA]	1442.1	1386.5	1328.9	1247.4	1185.0	1116.9
ESR	0.7384	0.7454	0.7586	0.7736	0.7883	0.8002
ESR_C	0.6792	0.6887	0.7022	0.7239	0.7368	0.7500
ASSAI	0.7213	0.7299	0.7446	0.7571	0.7730	0.7855
$ASSAI_C$	0.7546	0.7629	0.7744	0.7898	0.7992	0.8116

SRT Trends

SRT as a function of repair crew count is shown in Figure 6.3. With an increasing number of crews repairing equipment concurrently, total SRT appears to decay exponentially and approach an asymptotic value. It might seem reasonable to assume this metric would asymptotically approach a value of zero; however, because SRT is the time it takes for all impacted equipment to return to normal operation, the minimum possible value for SRT is determined by the longest equipment failure duration among the impacted equipment. Another point to note about this trend is that as the repair crew count increases, the variance in mean SRT value decreases. This is most likely due to a reduction of in-service failures associated with a shorter simulated repair time.

Figure 6.3. Trends in mean (red) and median (green) SRT as a function of repair crew size.

EIP and EDRR Trends

Figures 6.4 and 6.5 provide a trend plot of EIP and EDRR with increasing repair crew count, respectively. Median EIP value remains constant through all crew sizes, as is expected since the region impacted by the extreme event remains constant for each crew count simulation series; however, as crew count increases and median SRT value decreases, median EDRR increases almost quadratically. The increasing error bar range with increasing repair crew count for mean EDRR value is because the magnitude of mean EDRR increases by nearly a full order of magnitude; with increased magnitude comes increased variance.

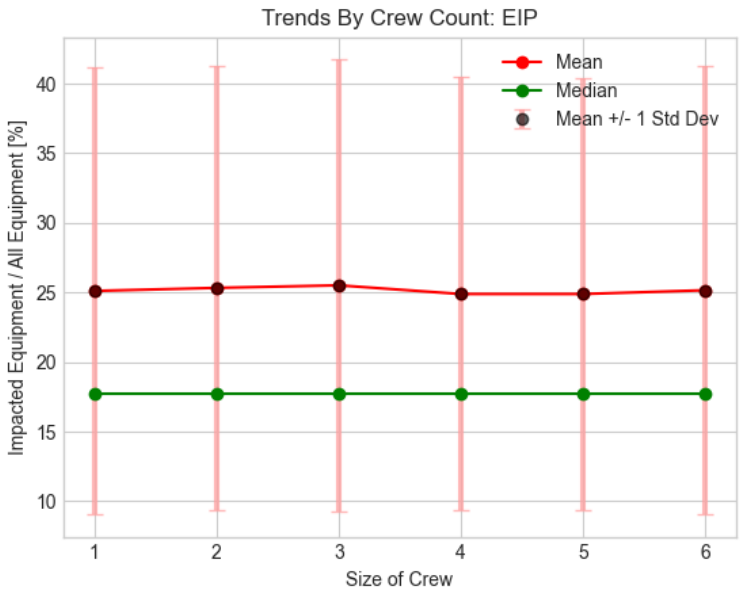

Figure 6.4. Trends in mean (red) and median (green) EIP as a function of repair crew size.

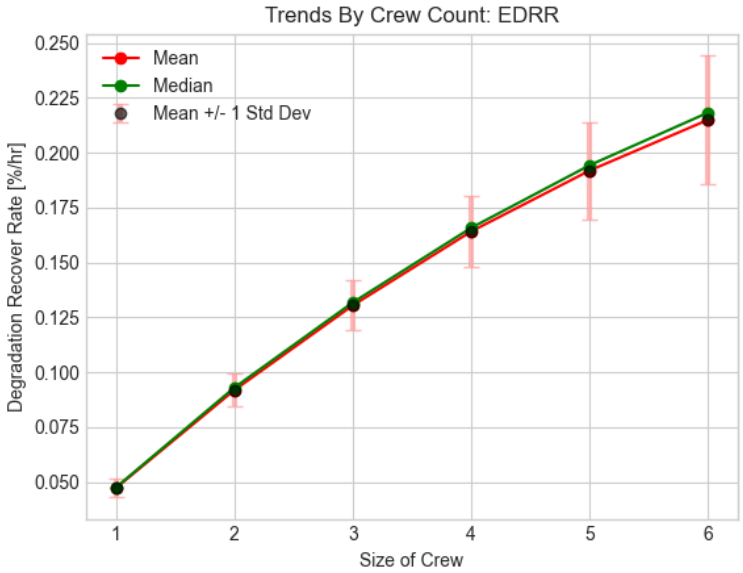

Figure 6.5. Trends in mean (red) and median (green) EDRR as a function of repair crew size.

ENS and ENS_C Trends

Figures 6.6 and 6.7 show the trend that ENS and ENS_C, respectively, follow with increasing repair crew count. Both these values decay almost exponentially and will eventually reach a minimum value greater than zero due to the finite repair time of buses and the strategy employed to reconnect loads and repair equipment. If a more directed repair strategy was to be employed that prioritized reconnecting loads, it is possible this value could be reduced further; this claim would need to be experimented with in a later work, though. Considering the difference in scale and scope between ENS and ENS_C, little more can be determined regarding the significance of these values relative to each other besides demonstrating their magnitudes.

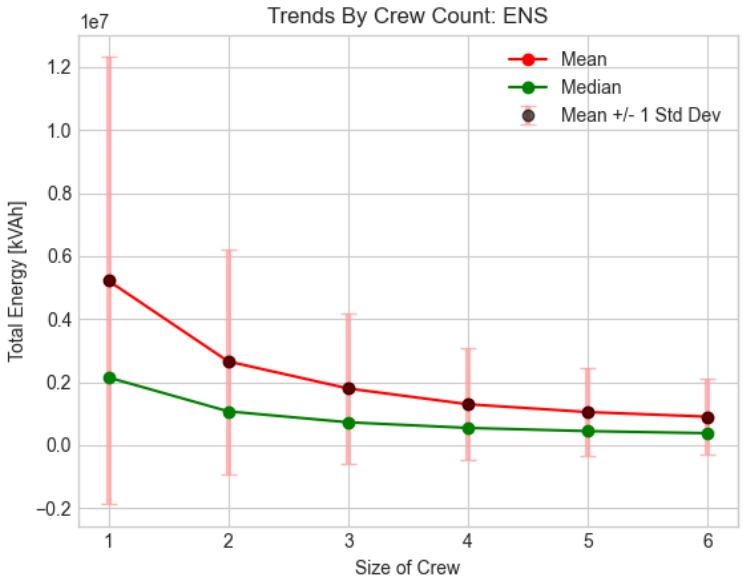

Figure 6.6. Trends in mean (red) and median (green) ENS as a function of repair crew size.

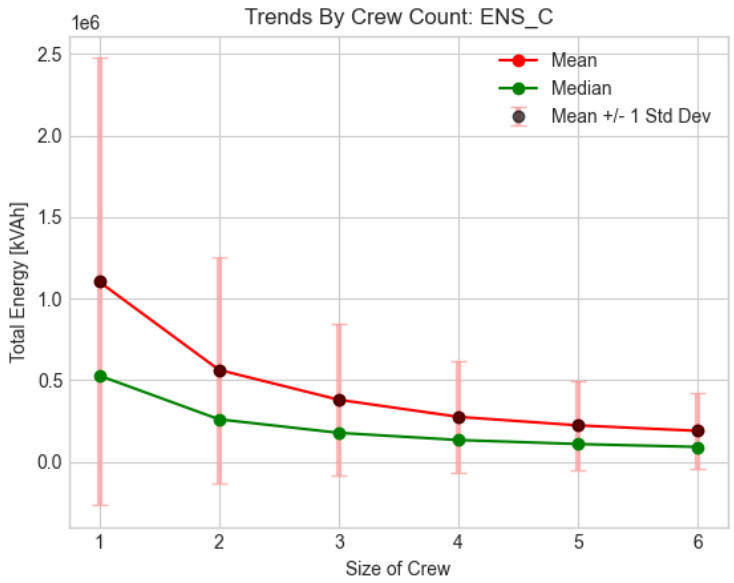

Figure 6.7. Trends in mean (red) and median (green) ENS_C as a function of repair crew size.

APNS and $APNS_C$ Trends

Figures 6.8 and 6.9 show the trend of APNS and $APNS_C$, respectively, according to increasing repair crew count. As expected and desired, with an increased number of work crews repairing the system concurrently, the SRT decreases and loads can be reconnected to the grid faster; accordingly, the average power not supplied to all loads and specifically to critical loads decreases at an approximately linear rate. This is a desirable trend, since a lower power not supplied rating represents stronger resilience in the recovery stage of event response. Unfortunately, similarly to ENS and ENS_C, these metrics portray absolute values, and thus, no insight can be gained by comparing these values against each other; no context is provided with these values as to how "good" or "bad" these values are at any point in the simulation.

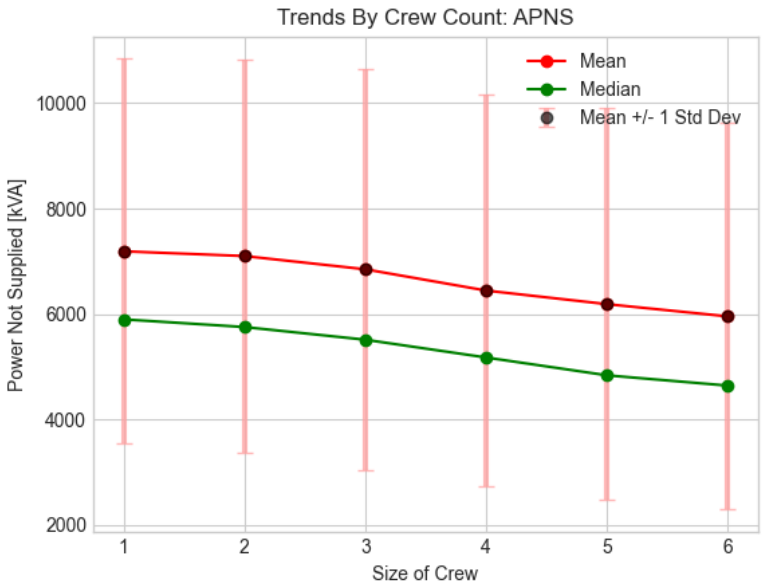

Figure 6.8. Trends in mean (red) and median (green) APNS as a function of repair crew size.

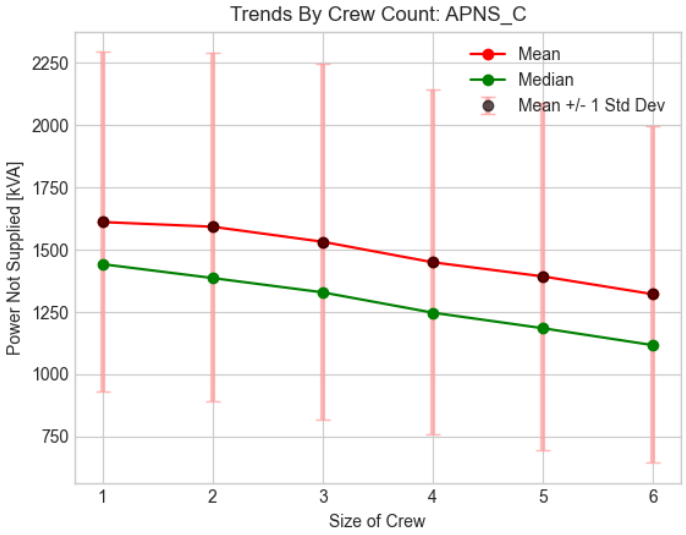

Figure 6.9. Trends in mean (red) and median (green) $APNS_C$ as a function of repair crew size.

ESR and ESR_C Trends

Figures 6.10 and 6.11 display the ESR and ESR_C, respectively, as a function of work crew count. As with other metrics previously mentioned, the trend of these values is predictable

in the sense of increasing with greater work crew availability. When more resources are available to facilitate equipment repairs, a greater number of loads can be reconnected in a shorter duration, resulting in a greater ratio of energy supplied.

Ideally, ESR_C for each data point would be greater than ESR to emphasize the fact that critical loads are supplied with priority over normal loads; the lack of this trend could be due in part to poor BESS energy management and demand-side management when limited generation resources are available. If a BESS outputs maximum power to supply loads without ignoring normal loads during an emergency operation condition, the BESS will become depleted and then no load on that islanded system will receive power, negatively impacting the ESR and ESR_C ratings of the system. This challenge could be a point for future research in optimizing BESS management strategies with demand-side management to continue supplying critical loads in emergency situations.

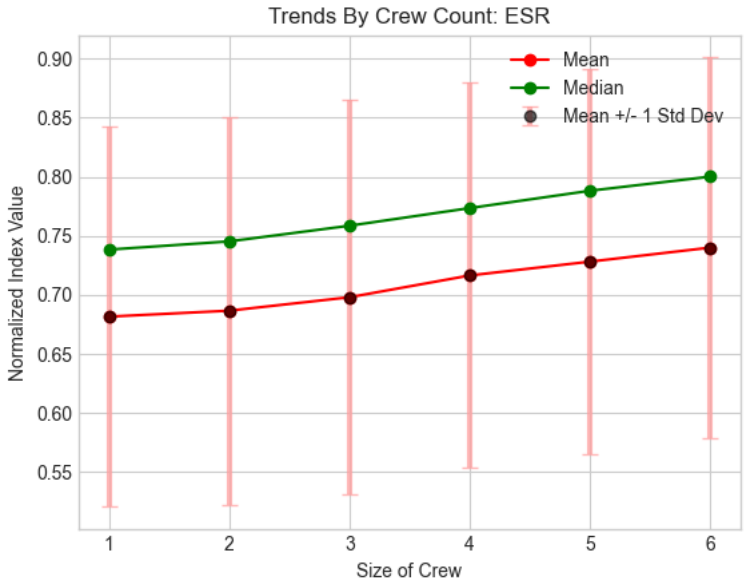

Figure 6.10. Trends in mean (red) and median (green) ENS as a function of repair crew size.

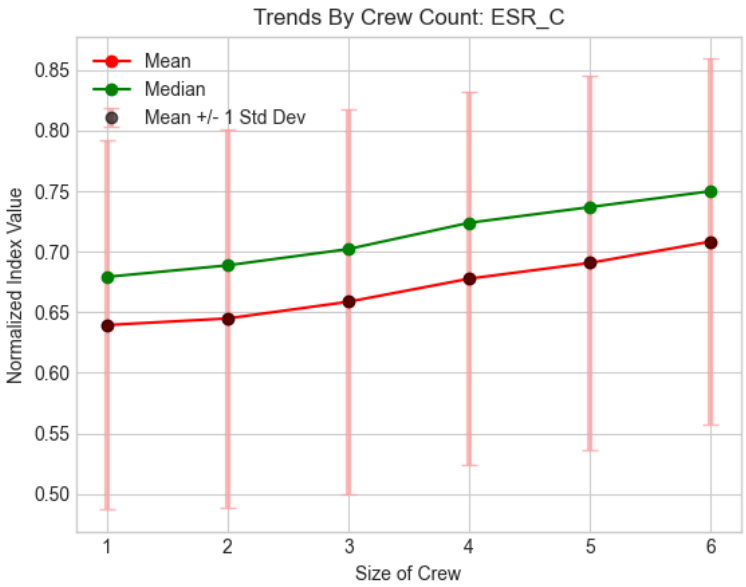

Figure 6.11. Trends in mean (red) and median (green) ESR_C as a function of repair crew size.

ASSAI and $ASSAI_C$ Trends

Figures 6.12 and 6.13 show trends with ASSAI and $ASSAI_C$, respectively, with increasing repair crews for recovery. Like ESR and ESR_C, both these values increase approximately linearly with repair crew count. Unlike what was discussed for those metrics, though, ASSAI and $ASSAI_C$ behave as expected, with $ASSAI_C$ being greater than ASSAI for each data point. The margin where this is true is only between 0.02 and 0.04, but the expected trend is present. This margin could likely be improved in the same way ESR and ESR_C could be improved by future work: investigating BESS energy management strategies optimized for continuing to supply critical loads in emergency operation scenarios.

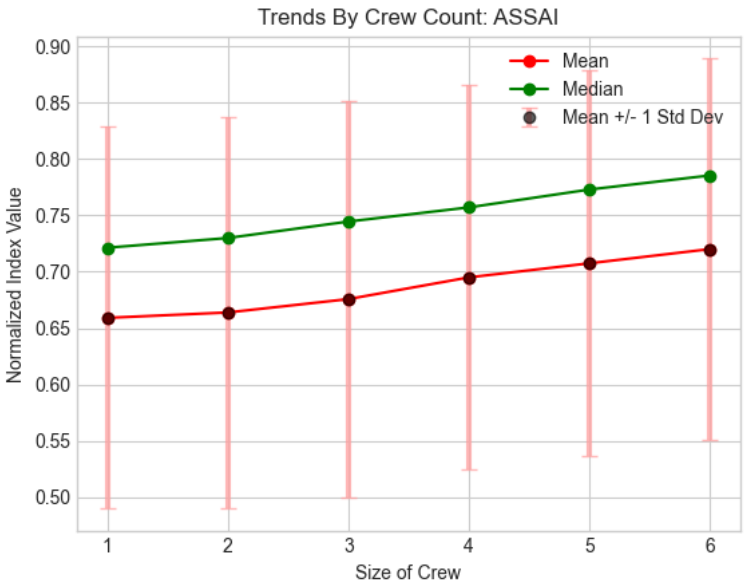

Figure 6.12. Trends in mean (red) and median (green) ASSAI as a function of repair crew size.

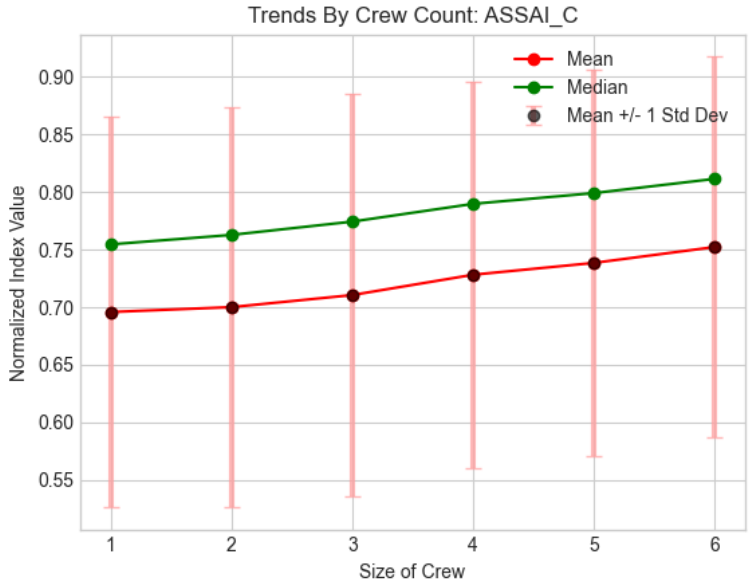

Figure 6.13. Trends in mean (red) and median (green) $ASSAI_C$ as a function of repair crew

CONCLUSION

The objective of this research was to investigate power system resilience through simulation of a benchmark test system specified in [4] and propose metrics to be utilized in evaluating that system's resilience to system degradation caused by extreme events. This objective was not only met, but the model produced to analyze the test system includes perhaps a greater level of detail than what is necessary to accomplish this objective.

As evidenced by the previous chapters in this paper, an extensive model for simulating system degradation and recovery from an extreme event was created. Simulation results from this model are produced by maintaining several aspects constant between multiple executions (regional topography, extreme event impact probability model, and initial equipment operation times). Other aspects tend to introduce stochastic processes to the recovery dynamics of the test system and result in variation between multiple simulations (initial BESS SOC levels, the random process used to establish overall system degradation, hour of year at which the extreme event occurs, repair crew skill, equipment repair time, and repair strategy when using a blind-pick repair strategy). To reduce a single simulation's impact on any conclusion drawn regarding expected values for simulation results, a Monte-Carlo simulation approach was utilized to gather thousands of data points and evaluate resilience metrics against what is the most likely system behavior during recovery.

Several iterations of this Monte-Carlo simulation were performed to test the effect that different numbers of repair crews have on resilience metrics. As expected, increasing the number of repair crews available (which can be generalized to say: increasing the number of resources available) during recovery improved the resilience metrics incrementally.

Through this work, several questions were raised that would be worthwhile pursuing with subsequent research. The first question regards what power flow analysis reveals during this recovery process. For example, any lines that become overloaded when trying to supply loads would trip during recovery and could become bottlenecks for the recovery process, becoming a driving factor for load curtailment. Investigating a power flow analysis during recovery could shed light for what equipment needs to be upgraded by a system manager. A second question pertains to additional resilience metrics that could be defined. For example, if economic data was available surrounding the cost of additional work crews on the recovery effort, the incremental improvement in resilience metrics could be compared against the additional cost of recovery resources to achieve that improvement; this could be an interesting optimization problem. A third question is regarding strategies implemented for BESS energy management and recovery; if different strategies with different objectives and operational logic were defined for implementation to the system, the potential improvement simply in effective dispatch of recovery resources would be intriguing. These additional questions could each be entire research works to investigate.

REFERENCES CITED

[1] A. B. Smith, "Climate.gov - Science & Information For A Climate-Smart Nation," Climate.gov, 9 January 2017. [Online]. Available: https://www.climate.gov/news-features/blogs/beyond-data/2016-historic-year-billion-dollar-weather-and-climate-disasters-us. [Accessed 17 November 2021].

[2] Merriam-Webster, "Resilience," 2021. [Online]. Available: https://www.merriam-webster.com/dictionary/resilience.

[3] R. N. Allan and R. Billington, Reliability Evaluation of Engineering Systems: Concepts and Techniques, Springer Science + Business Media, LLC, 1992.

[4] M. N. Alam, S. Chakrabarti and X. Liang, "A Benchmark Test System for Networked Microgrids," *IEEE Transactions on Industrial Informatics*, 2020.

[5] "Presidential Policy Directive -- Critical Infrastructure Security and Resilience," Office of the Press Secretary, Washington, D.C., 2013.

[6] National Infrastructure Advisory Council, "Critical Infrastructure Resilience: Final Report and Recommendations," Cybersecurity and Infrastructure Security Agency, Washington, D.C., 2010.

[7] J.-P. Watson, R. Guttromson, C. Silva-Monroy, R. Jeffers, K. Jones, J. Ellison, C. Rath, J. Gearhart, D. Jones, T. Corbet, C. Hanley and L. T. Walker, "Conceptual Framework for Developing Resilience Metrics for the Electricity, Oil, and gas Sectors in the United States," Office of Scientific and Technical Information, U.S. Department of Energy, Oak Ridge, TN, 2015.

[8] C. O'Hara, "PJM," 23 February 2018. [Online]. Available: https://www.pjm.com/-/media/committees-groups/committees/mrc/20180223-special/20180223-item-01-grid-resilience-in-rtos-and-isos.ashx. [Accessed 28 February 2021].

[9] Federal Energy Regulatory Commission, *Order Terminating Rulemaking Proceeding, Initiating New Proceeding, and Establishing Additional Procedures - RM18-1-000,* 2018.

[10] Reliability Issues Steering Committee, "Report on Resilience," North American Electric Reliability Corporation, Atlanta, 2018.

[11] M. Panteli and P. Mancarella, "The Grid: Stronger, Bigger, Smarter?," *IEEE Power & Energy Magazine,* pp. 58-66, May/June 2015.

[12] F. H. Jufri, V. Widiputra and J. Jung, "State-of-the-art review on power grid resilience to extreme weather events: Definitions, frameworks, quantitative assessment methodologies, and enhancement strategies," *Applied Energy*, vol. 239, no. February, pp. 1049-1065, 2019.

[13] F. Petit and V. Vargas, "Grid Modernization: Metrics Analysis (GMLC1.1) - Resilience," U.S. Department of Energy, Richland, WA, 2020.

[14] N. Bhusal, M. Abdelmalak, M. Kamruzzaman and M. Benidris, "Power System Resilience: Current Practices, Challenges, and Future Directions," *IEEE Access*, vol. 8, pp. 18064-18086, 2020.

[15] M. Mahzarnia, P. Siano and P. T. Baboli, "A Review of the Measures to Enhance Power Systems Resilience," *IEEE Systems Journal*, vol. 14, no. 3, pp. 4059-4070, 2020.

[16] Y. Yang, W. Tang, Y. Liu, Y. Xin and Q. Wu, "Quantitative Resilience Assessment for Power Transmission Systems Under Typhoon Weather," *IEEE Access*, vol. 6, pp. 40747-40756, 2018.

[17] J. Lu, J. Guo, Z. Jian, Y. Yang and W. Tang, "Dynamic Assessment of Resilience Power Transmission Systems in Ice Disasters," in *IEEE*, Guangzhou, China, 2018.

[18] Z. Yang, P. Dehghanian and M. Nazemi, "Enhancing Seismic Resilience of Electric Power Distribution Systems with Mobile Power Sources," in *IEEE*, Baltimore, MD, USA, 2019.

[19] U. Shipurkar, "Wind Turbine Generator Systems Failures - Probabilities and Mechanisms," Delft University of Technology, 2015.

[20] C. D. Dao, B. Kazemtabrizi and C. J. Crabtree, "Offshore Wind Turbine Reliability and Operational Simulation Under Uncertainties," *Wind Energy*, vol. 23, no. 10, pp. 1919-1938, 2020.

[21] A. Ellis, R. Nelson, E. Von Engeln, R. Walling, J. McDowell, L. Casey, E. Seymour, W. Peter, C. Barker and B. Kirby, "Reactive Power Interconnection Requirements for PV and Wind Plants - Recommendations to NERC," Sandia National Laboratories, Albuquerque, NM, 2012.

[22] NREL, "Researchers at NREL Find Fewer Failures of PV Panels and Different Degradation Modes in Systems Installed After 2000," NREL, 2017.

[23] NIST, "Impact of Grid Storage Functions on Battery Degradation," NIST, 2011.

[24] P. Selvam and M. McGowan, "New Study Shows Tornadoes Tend Toward Higher Elevations and Cause Greater Damage Moving Uphill," University of Arkansas, Fayetteville, AR, 2013.

[25] A. Gholami, T. Shekari, M. H. Amirioun, F. Aminifar, M. H. Amini and A. Sargolzaei, "Toward a Consensus on the Definition and Taxonomy of Power System Resilience," *IEEE Access*, vol. 6, pp. 32035-32053, 2018.

[26] R. Billington and R. N. Allan, Reliability Evaluation of Engineering Systems, Second Edition, New York: Springer Science + Business Media, LLC, 1992.

[27] University of Illinois, "Stephen Flynn," [Online]. Available: https://ciri.illinois.edu/people/stephen-flynn. [Accessed 11 April 2021].

[28] Federal Energy Regulatory Commission, *Order Terminating Proceeding - AD18-7-000*, 2021.

[29] Office of Electricity, "North American Energy Resilience Model," U.S. Department of Energy, Washington, D.C. , 2019.

APPENDICES

APPENDIX A

SIMULATION RESULT PLOTS FOR ONE REPAIR CREW

The following figures (Figures A.1-A.11) provide the statistical Monte-Carlo simulation results as a histogram for each resilience metric defined in chapter 5 of this paper. The statistical mean and median values are included on each plot.

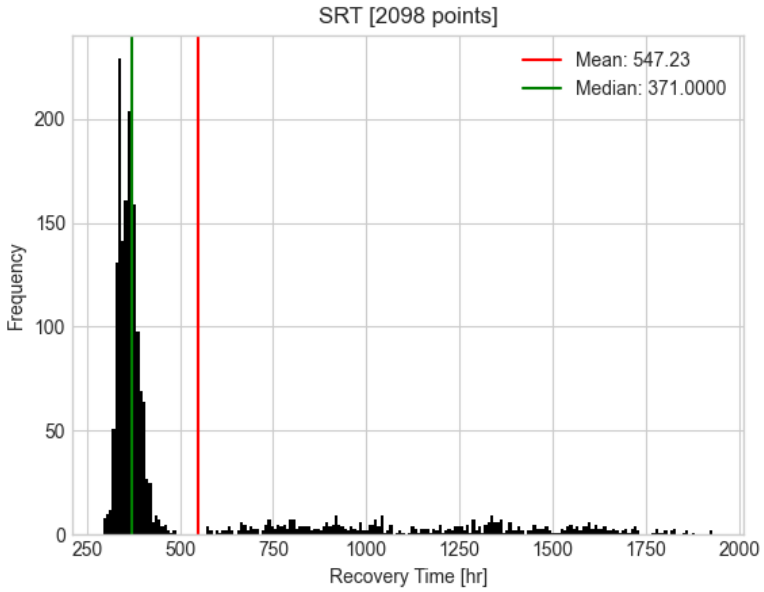

Figure A.1. Monte-Carlo simulation results for SRT under a severity-5 flood with a blind-pick repair strategy. The statistical mean (red) and median (green) are included.

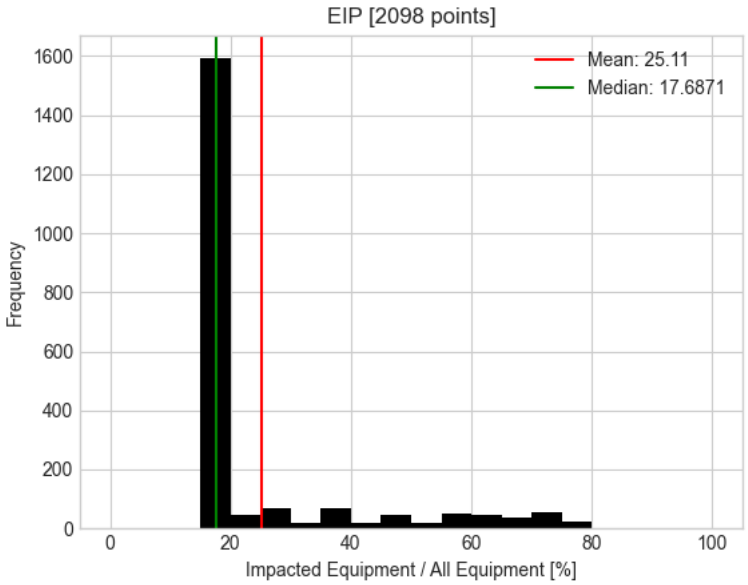

Figure A.2. Monte-Carlo simulation results for EIP under a severity-5 flood with a blind-pick repair strategy. The statistical mean (red) and median (green) are included.

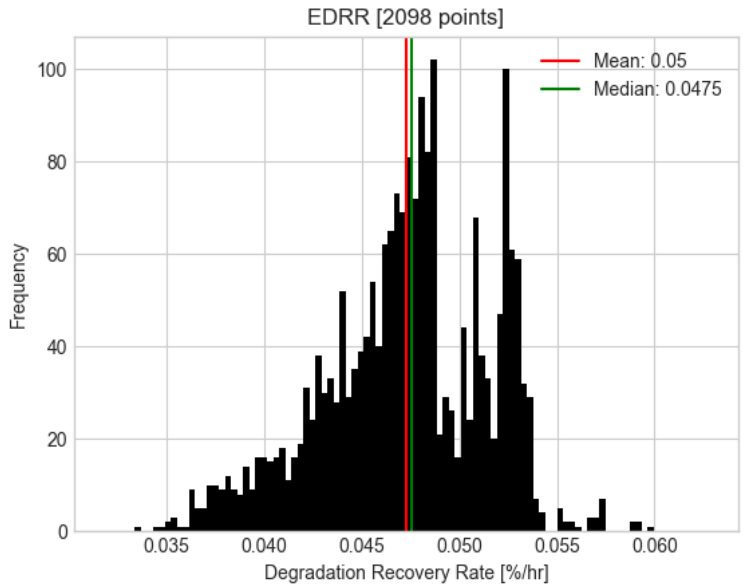

Figure A.3. Monte-Carlo simulation results for EDRR under a severity-5 flood with a blind-pick repair strategy. The statistical mean (red) and median (green) are included.

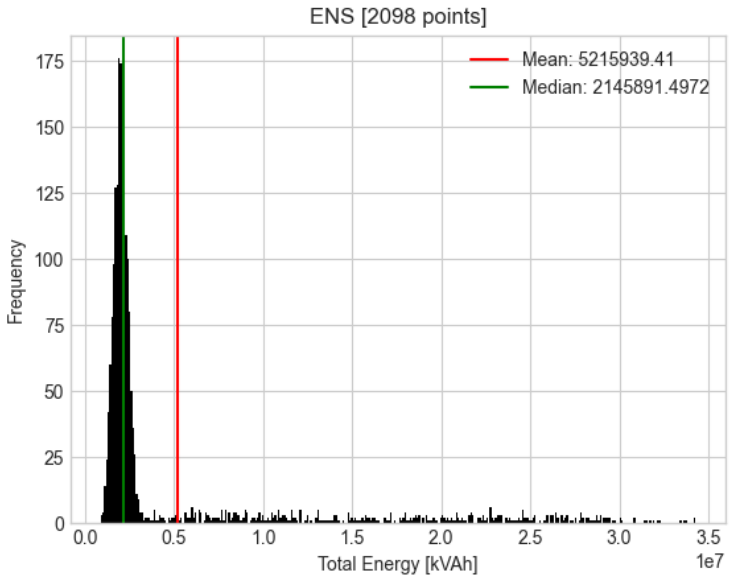

Figure A.4. Monte-Carlo simulation results for ENS under a severity-5 flood with a blind-pick repair strategy. The statistical mean (red) and median (green) are included.

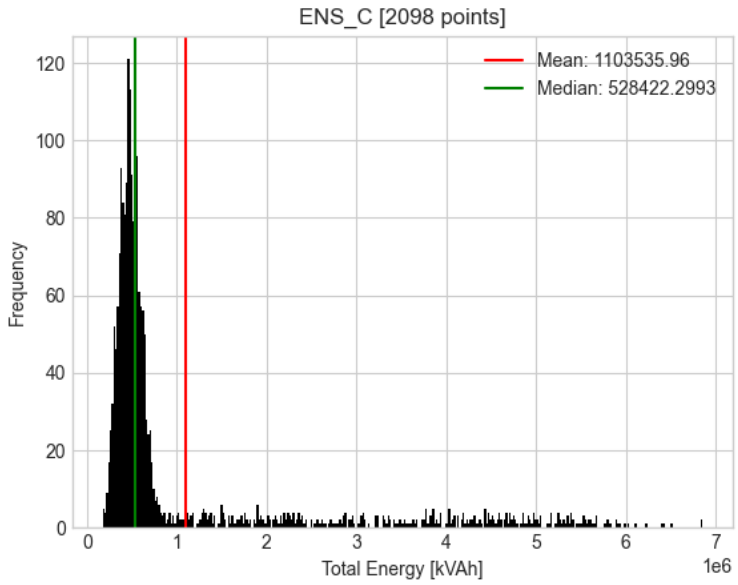

Figure A.5. Monte-Carlo simulation results for ENS_C under a severity-5 flood with a blind-pick repair strategy. The statistical mean (red) and median (green) are included.

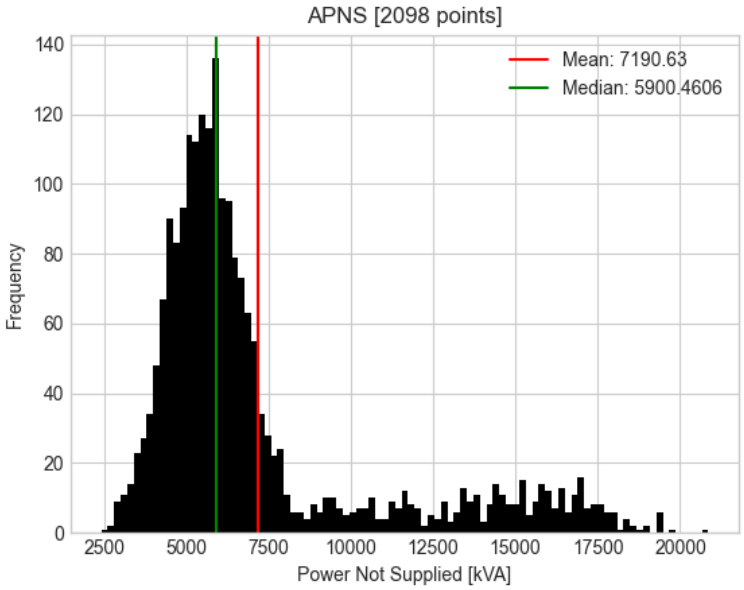

Figure A.6. Monte-Carlo simulation results for APNS under a severity-5 flood with a blind-pick repair strategy. The statistical mean (red) and median (green) are included.

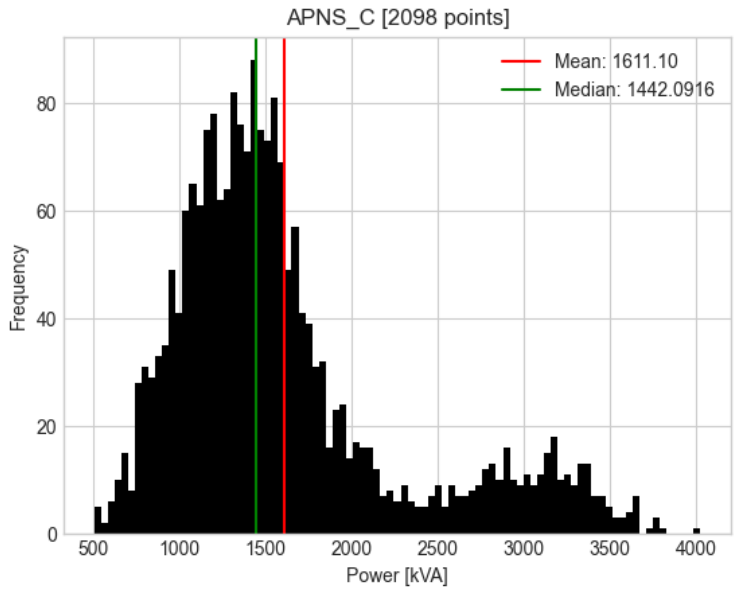

Figure A.7. Monte-Carlo simulation results for $APNS_C$ under a severity-5 flood with a blind-pick repair strategy. The statistical mean (red) and median (green) are included.

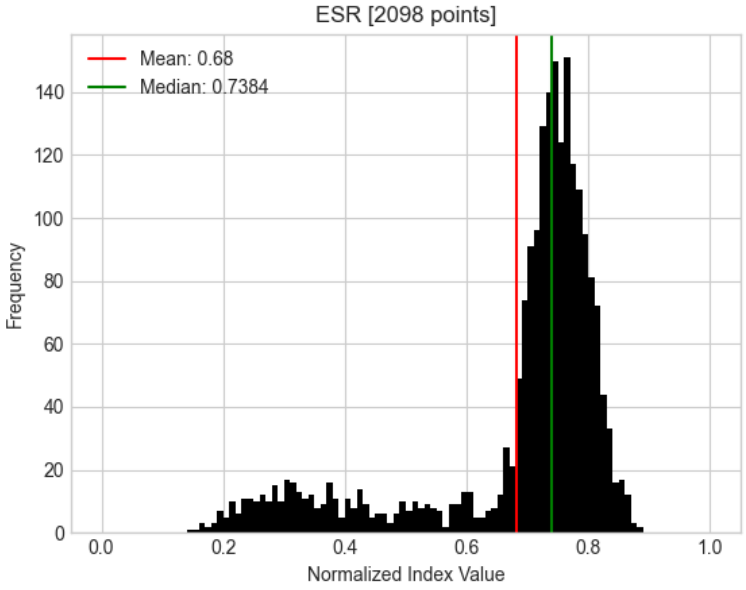

Figure A.8. Monte-Carlo simulation results for ESR under a severity-5 flood with a blind-pick repair strategy. The statistical mean (red) and median (green) are included.

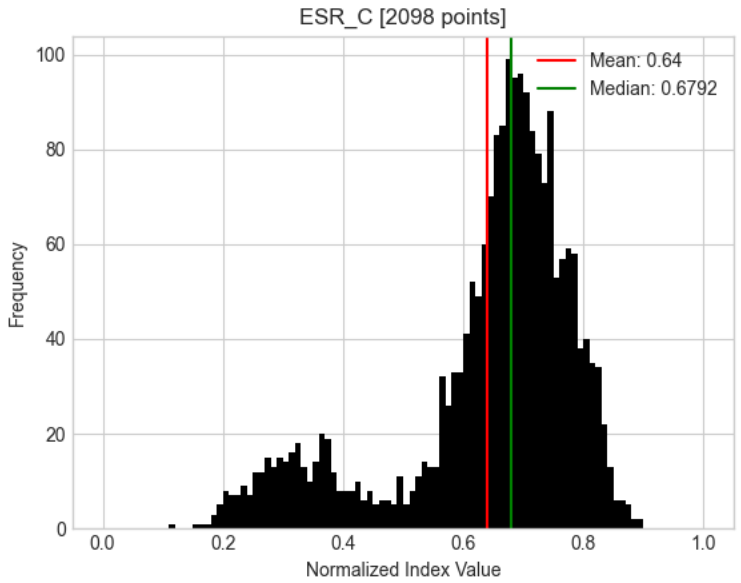

Figure A.9. Monte-Carlo simulation results for ESR_C under a severity-5 flood with a blind-pick repair strategy. The statistical mean (red) and median (green) are included.

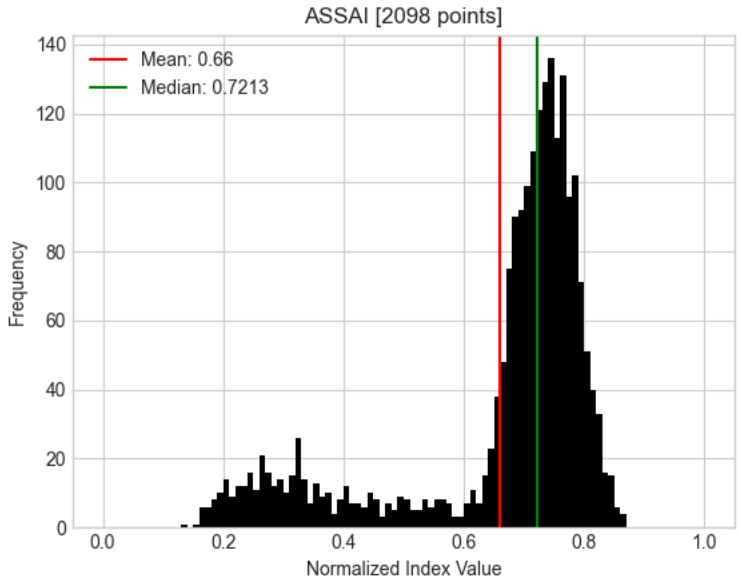

Figure A.10. Monte-Carlo simulation results for ASSAI under a severity-5 flood with a blind-pick repair strategy. The statistical mean (red) and median (green) are included.

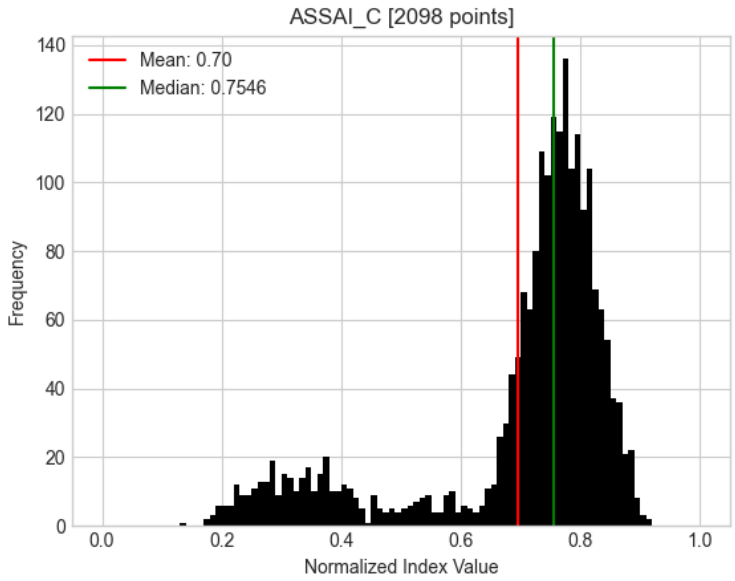

Figure A.11. Monte-Carlo simulation results for $ASSAI_C$ under a severity-5 flood with a blind-pick repair strategy. The statistical mean (red) and median (green) are included.

APPENDIX B

SIMULATION RESULT PLOTS FOR TWO REPAIR CREWS

The following figures (Figures B.1-B.11) provide the statistical Monte-Carlo simulation results as a histogram for each resilience metric defined in chapter 5 of this paper. The statistical mean and median values are included on each plot.

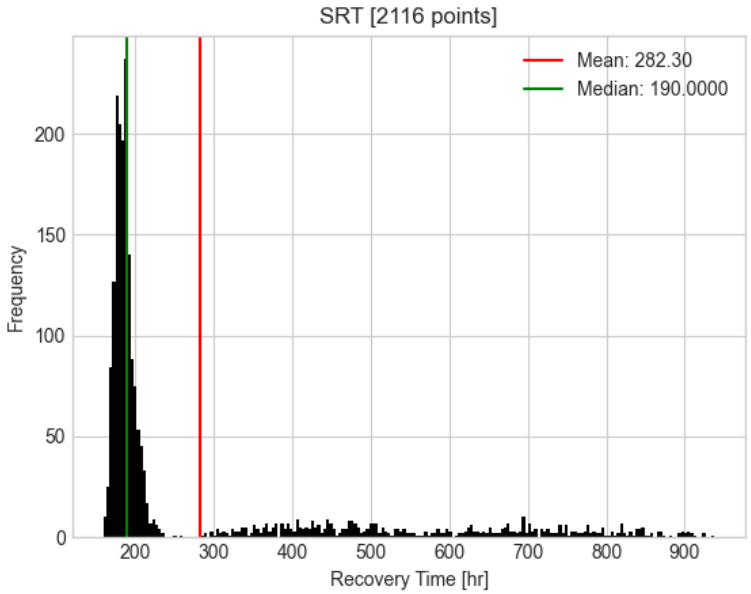

Figure B.1. Monte-Carlo simulation results for SRT under a severity-5 flood with a blind-pick repair strategy. The statistical mean (red) and median (green) are included.

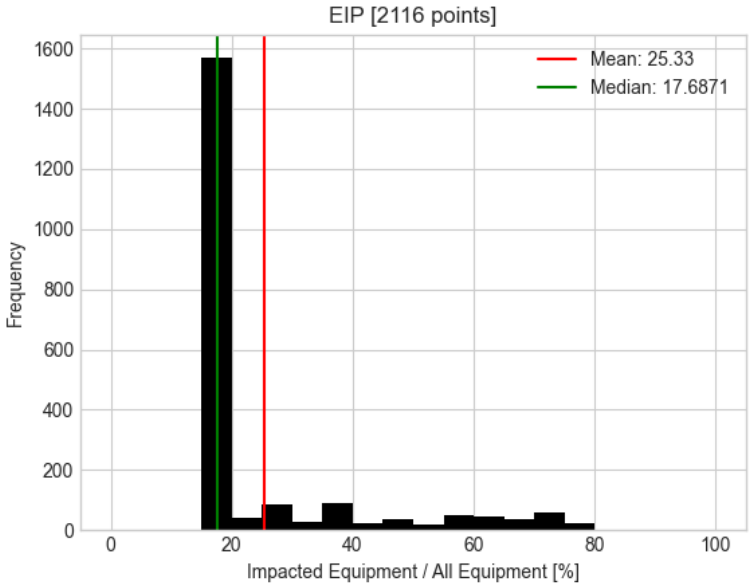

Figure B.2. Monte-Carlo simulation results for EIP under a severity-5 flood with a blind-pick repair strategy. The statistical mean (red) and median (green) are included.

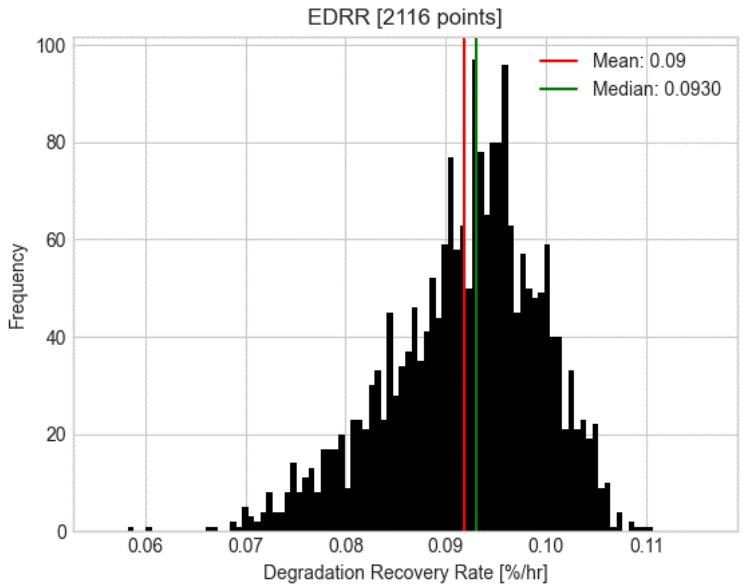

Figure B.3. Monte-Carlo simulation results for EDRR under a severity-5 flood with a blind-pick repair strategy. The statistical mean (red) and median (green) are included.

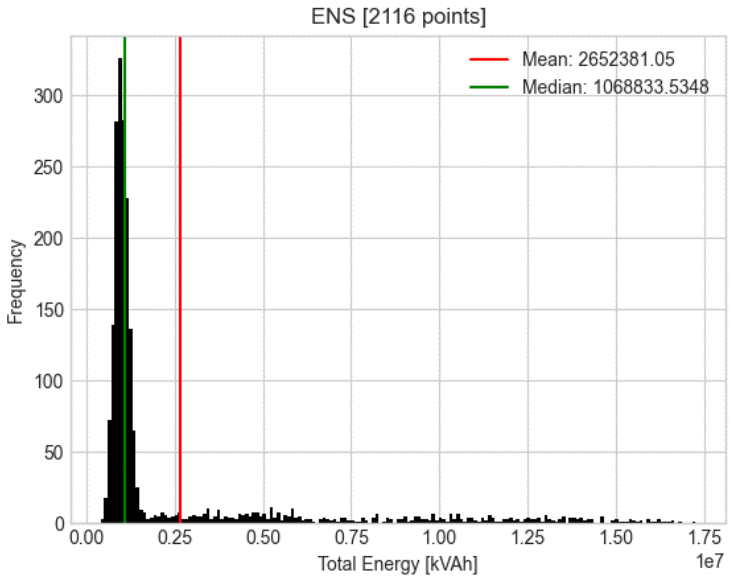

Figure B.4. Monte-Carlo simulation results for ENS under a severity-5 flood with a blind-pick repair strategy. The statistical mean (red) and median (green) are included.

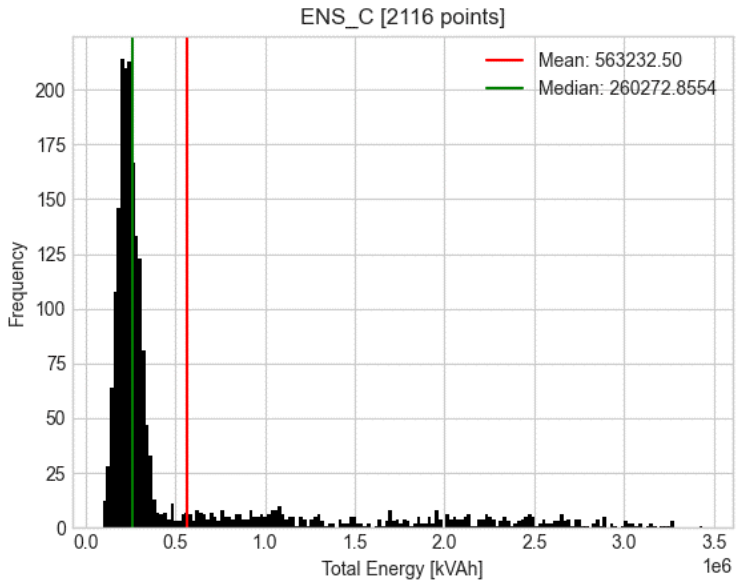

Figure B.5. Monte-Carlo simulation results for ENS_C under a severity-5 flood with a blind-pick repair strategy. The statistical mean (red) and median (green) are included.

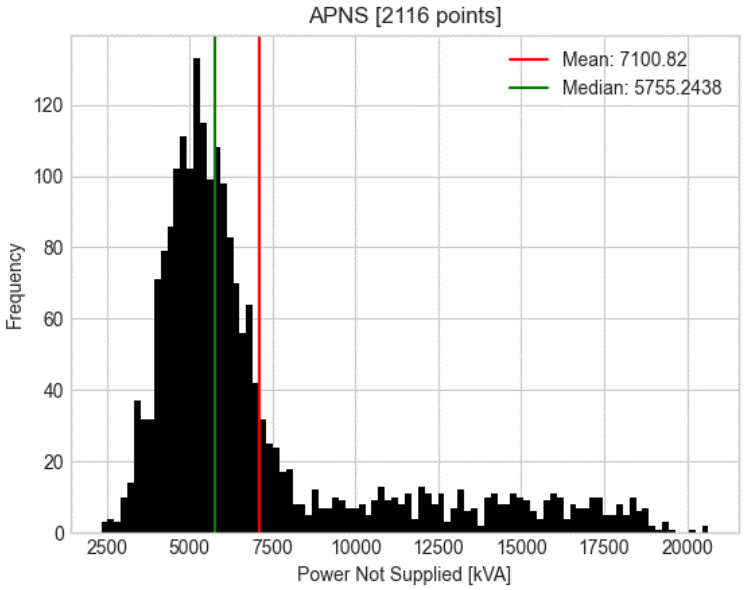

Figure B.6. Monte-Carlo simulation results for APNS under a severity-5 flood with a blind-pick repair strategy. The statistical mean (red) and median (green) are included.

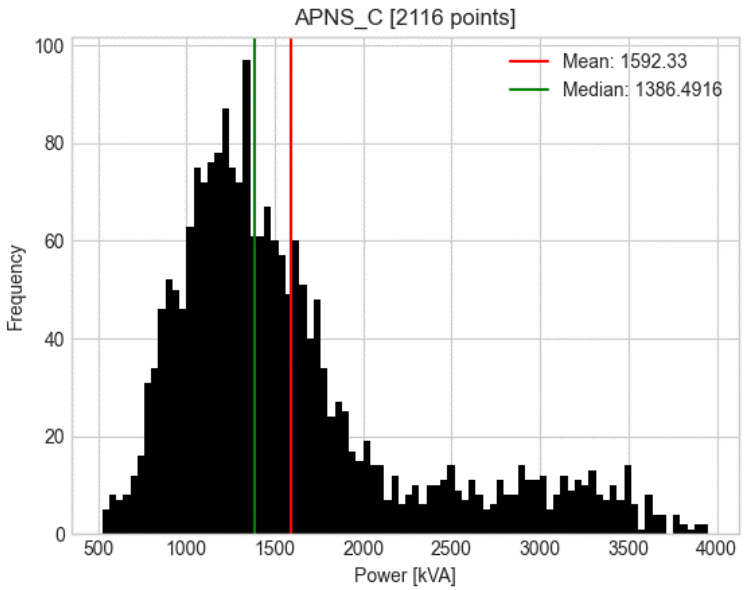

Figure B.7. Monte-Carlo simulation results for $APNS_C$ under a severity-5 flood with a blind-pick repair strategy. The statistical mean (red) and median (green) are included.

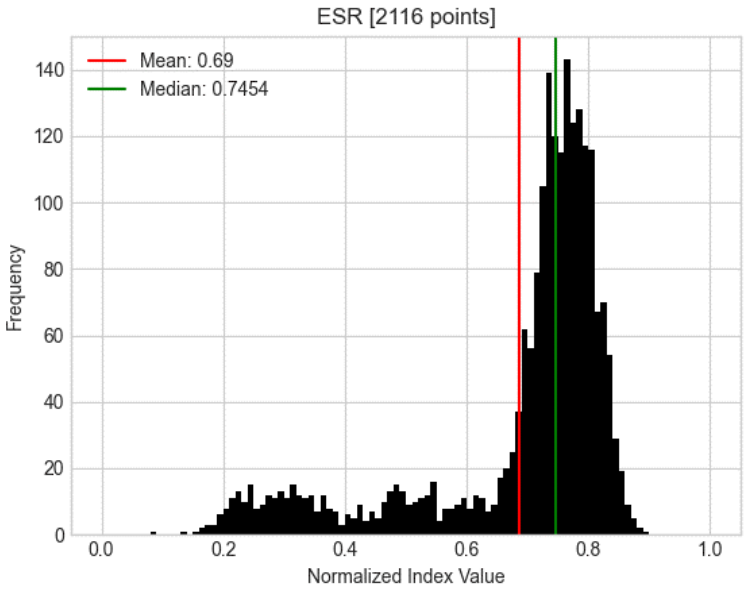

Figure B.8. Monte-Carlo simulation results for ESR under a severity-5 flood with a blind-pick repair strategy. The statistical mean (red) and median (green) are included.

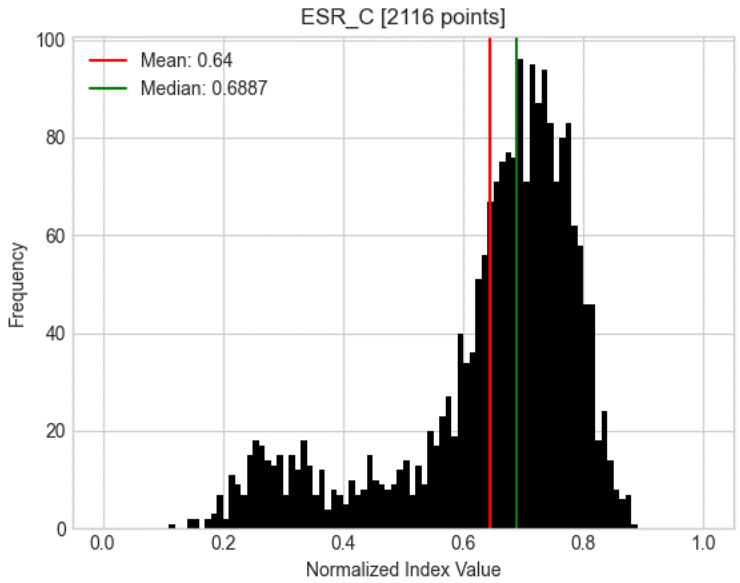

Figure B.9. Monte-Carlo simulation results for ESR_C under a severity-5 flood with a blind-pick repair strategy. The statistical mean (red) and median (green) are included.

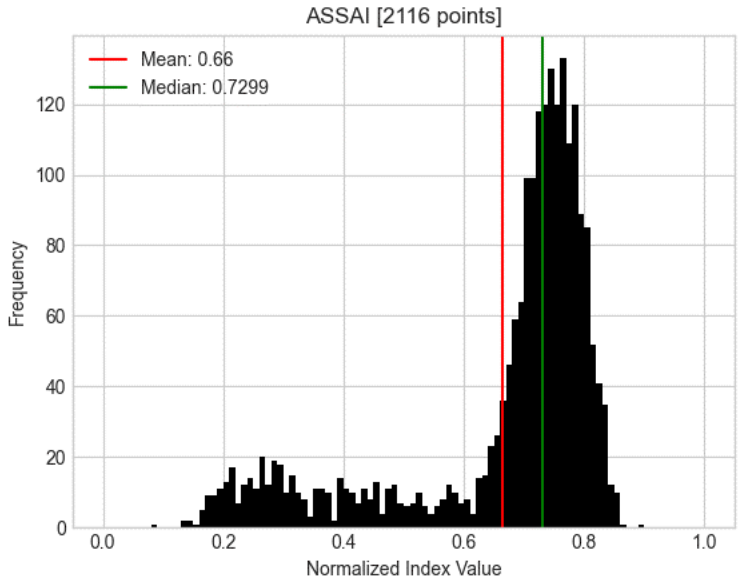

Figure B.10. Monte-Carlo simulation results for ASSAI under a severity-5 flood with a blind-pick repair strategy. The statistical mean (red) and median (green) are included.

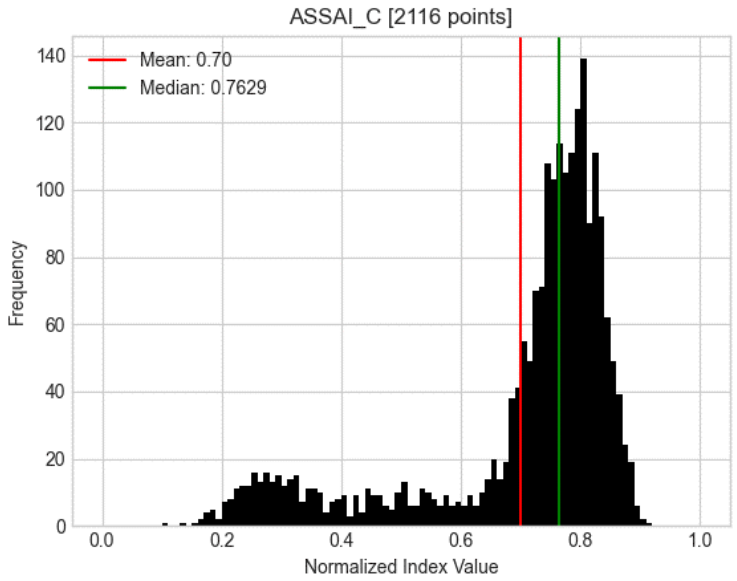

Figure B.11. Monte-Carlo simulation results for $ASSAI_C$ under a severity-5 flood with a blind-pick repair strategy. The statistical mean (red) and median (green) are included.

APPENDIX C

SIMULATION RESULT PLOTS FOR THREE REPAIR CREWS

The following figures (Figures C.1-C.11) provide the statistical Monte-Carlo simulation results as a histogram for each resilience metric defined in chapter 5 of this paper. The statistical mean and median values are included on each plot.

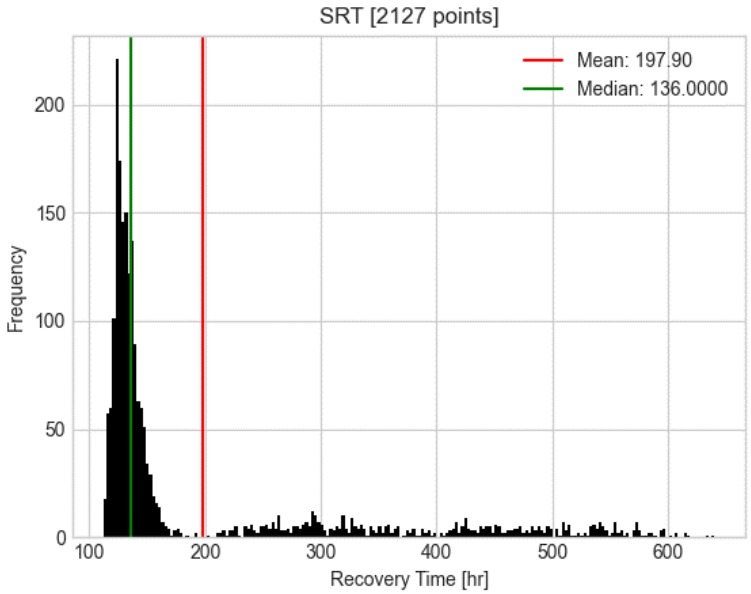

Figure C.1. Monte-Carlo simulation results for SRT under a severity-5 flood with a blind-pick repair strategy. The statistical mean (red) and median (green) are included.

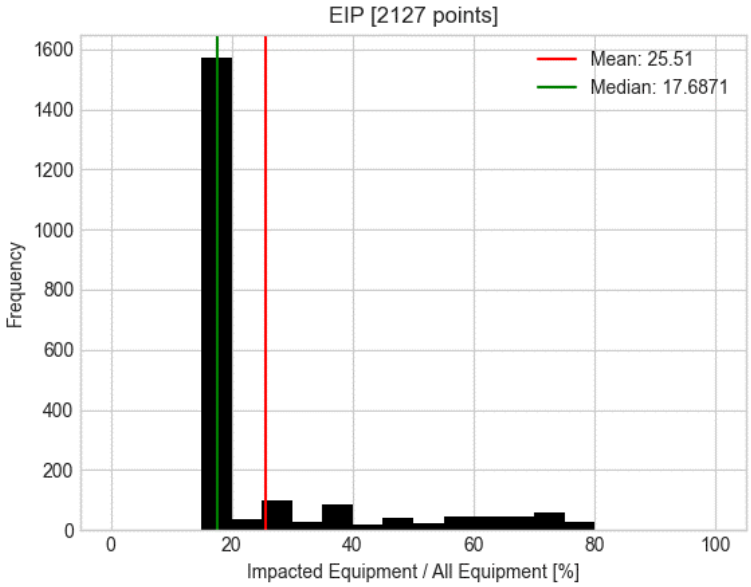

Figure C.2. Monte-Carlo simulation results for EIP under a severity-5 flood with a blind-pick repair strategy. The statistical mean (red) and median (green) are included.

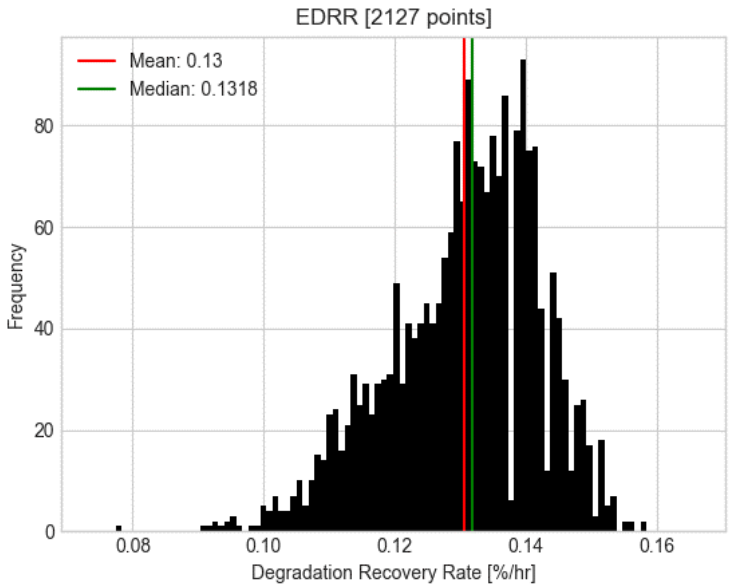

Figure C.3. Monte-Carlo simulation results for EDRR under a severity-5 flood with a blind-pick repair strategy. The statistical mean (red) and median (green) are included.

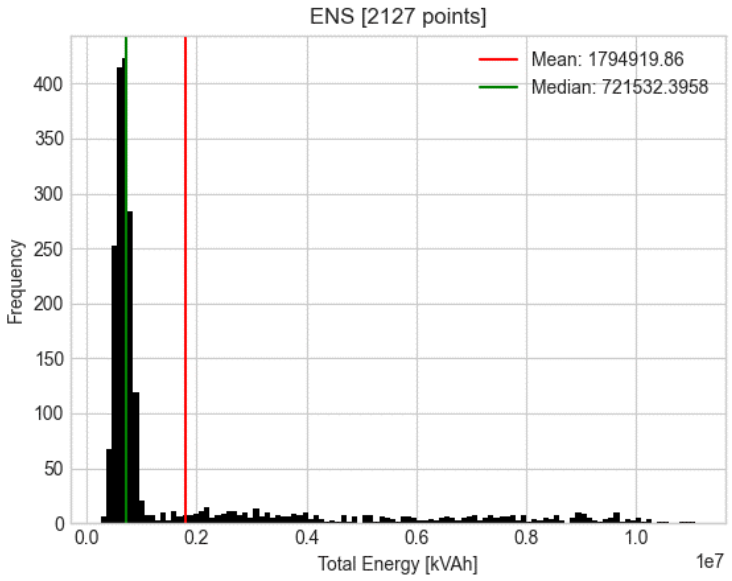

Figure C.4. Monte-Carlo simulation results for ENS under a severity-5 flood with a blind-pick repair strategy. The statistical mean (red) and median (green) are included.

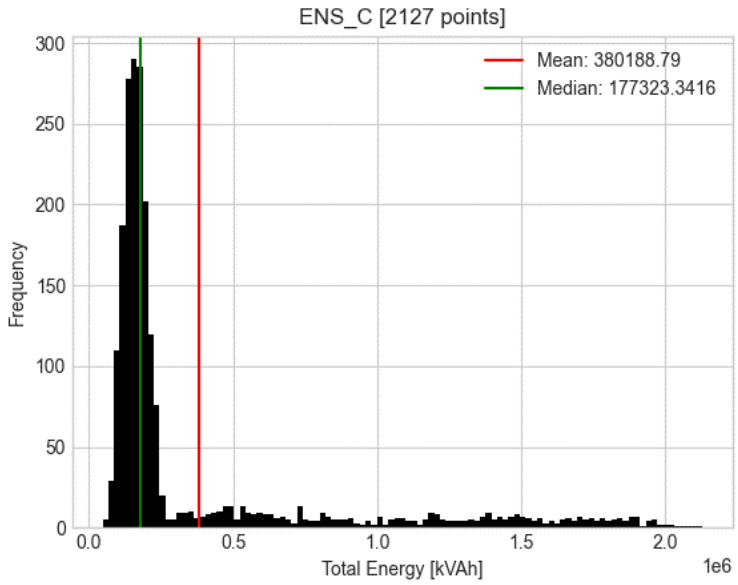

Figure C.5. Monte-Carlo simulation results for ENS_C under a severity-5 flood with a blind-pick repair strategy. The statistical mean (red) and median (green) are included.

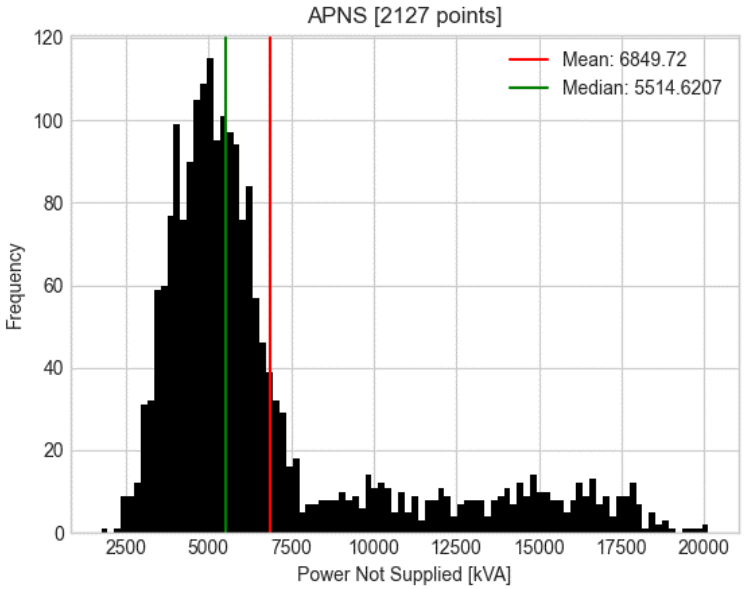

Figure C.6. Monte-Carlo simulation results for APNS under a severity-5 flood with a blind-pick repair strategy. The statistical mean (red) and median (green) are included.

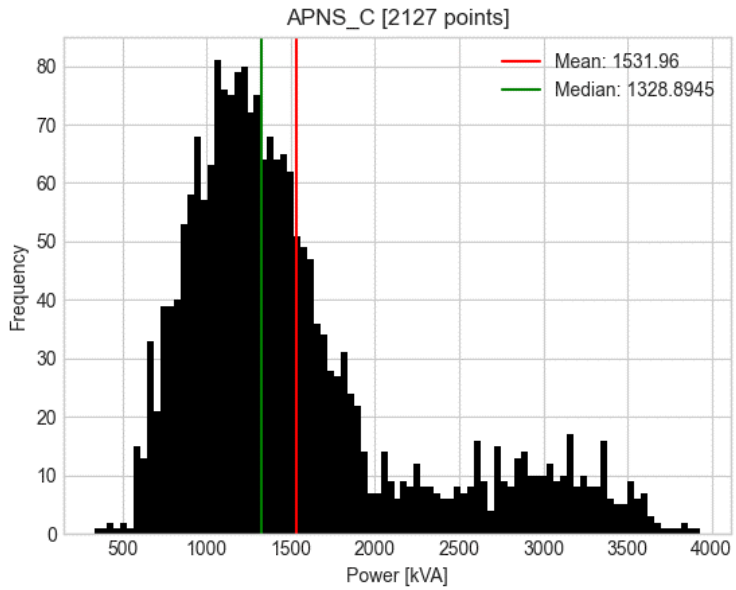

Figure C.7. Monte-Carlo simulation results for $APNS_C$ under a severity-5 flood with a blind-pick repair strategy. The statistical mean (red) and median (green) are included.

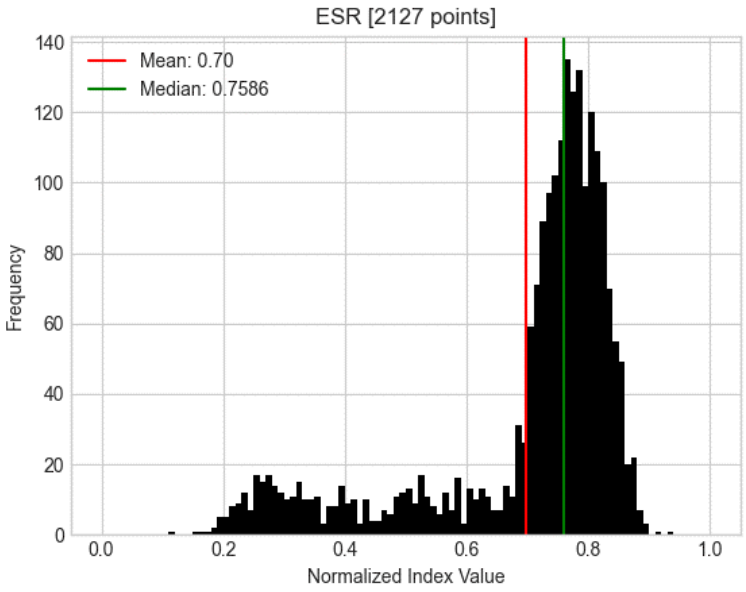

Figure C.8. Monte-Carlo simulation results for ESR under a severity-5 flood with a blind-pick repair strategy. The statistical mean (red) and median (green) are included.

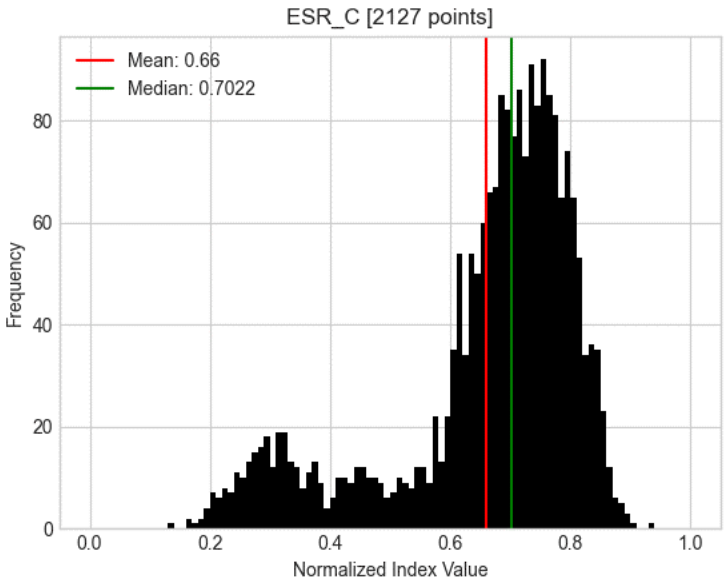

Figure C.9. Monte-Carlo simulation results for ESR_C under a severity-5 flood with a blind-pick repair strategy. The statistical mean (red) and median (green) are included.

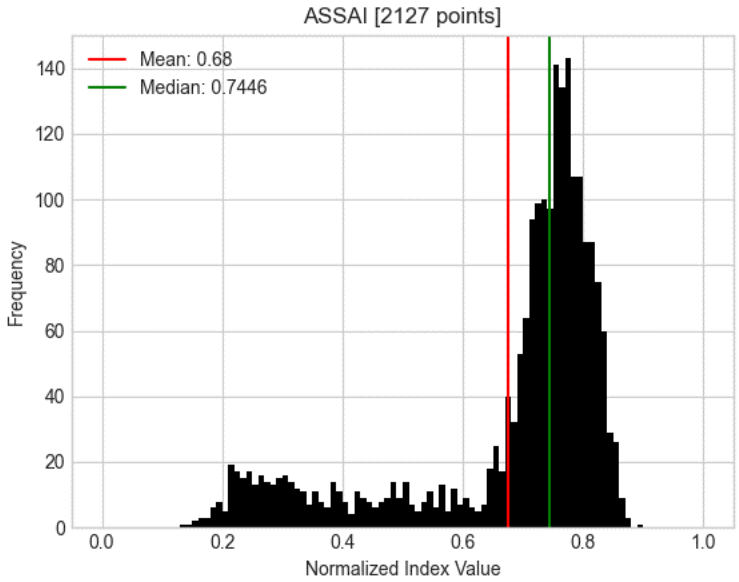

Figure C.10. Monte-Carlo simulation results for ASSAI under a severity-5 flood with a blind-pick repair strategy. The statistical mean (red) and median (green) are included.

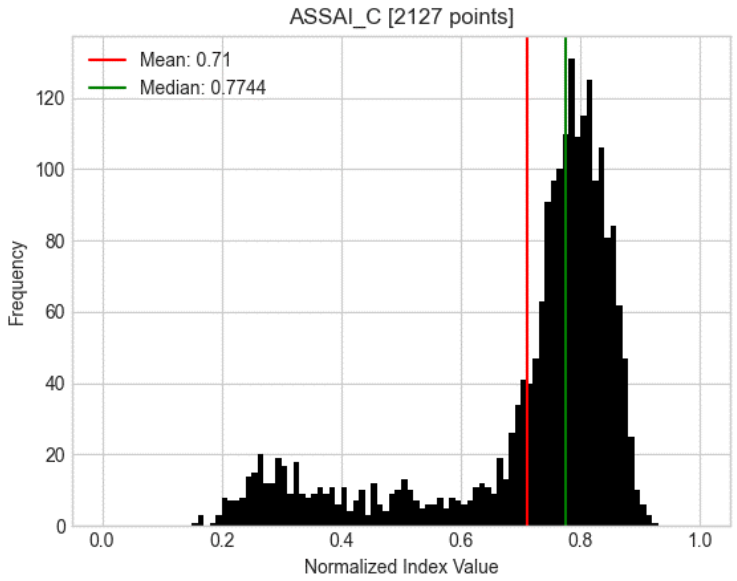

Figure C.11. Monte-Carlo simulation results for $ASSAI_C$ under a severity-5 flood with a blind-pick repair strategy. The statistical mean (red) and median (green) are included.

APPENDIX D

SIMULATION RESULT PLOTS FOR FOUR REPAIR CREW

The following figures (Figures D.1-D.11) provide the statistical Monte-Carlo simulation results as a histogram for each resilience metric defined in chapter 5 of this paper. The statistical mean and median values are included on each plot.

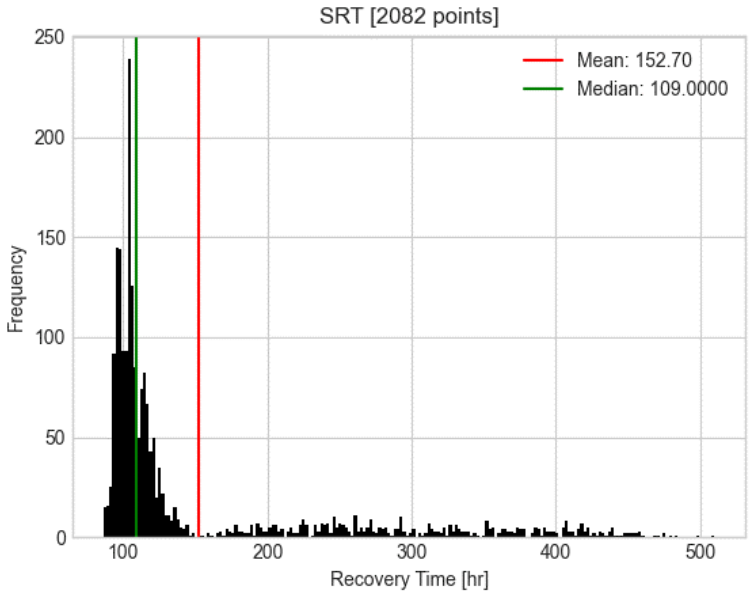

Figure D.1. Monte-Carlo simulation results for SRT under a severity-5 flood with a blind-pick repair strategy. The statistical mean (red) and median (green) are included.

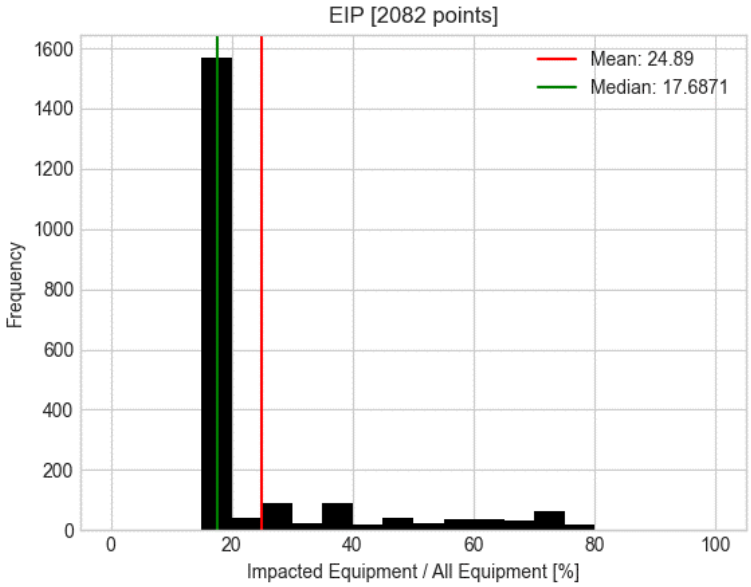

Figure D.2. Monte-Carlo simulation results for EIP under a severity-5 flood with a blind-pick repair strategy. The statistical mean (red) and median (green) are included.

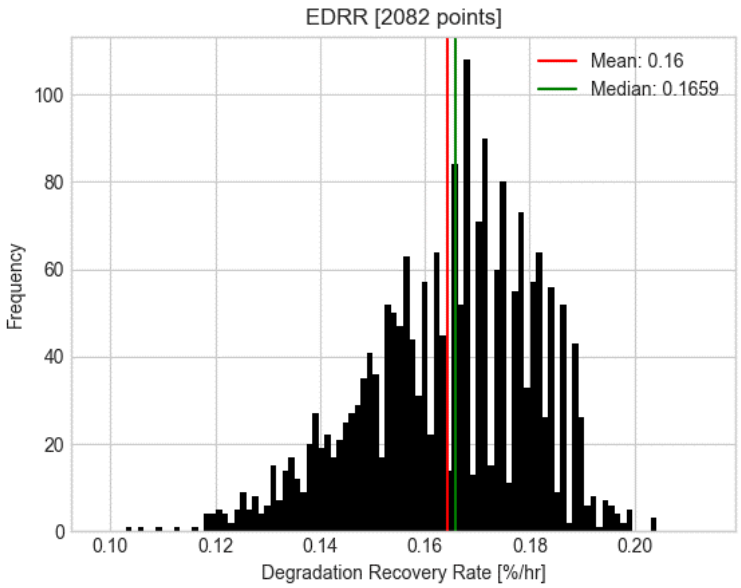

Figure D.3. Monte-Carlo simulation results for EDRR under a severity-5 flood with a blind-pick repair strategy. The statistical mean (red) and median (green) are included.

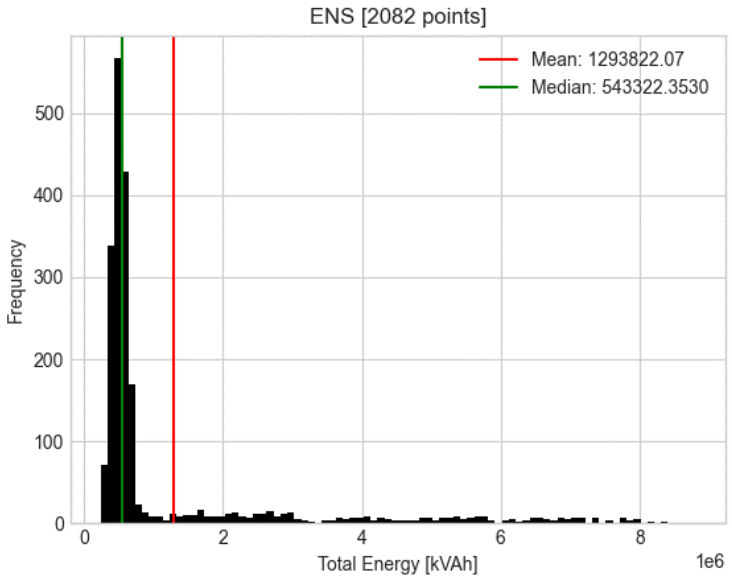

Figure D.4. Monte-Carlo simulation results for ENS under a severity-5 flood with a blind-pick repair strategy. The statistical mean (red) and median (green) are included.

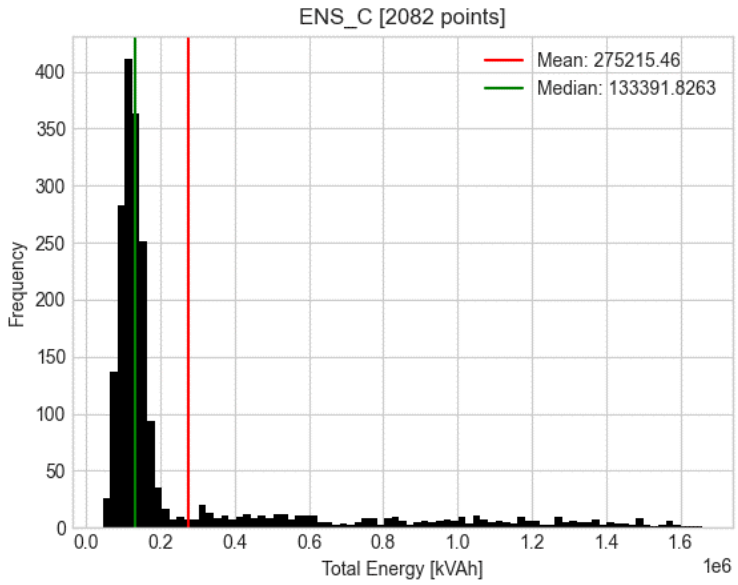

Figure D.5. Monte-Carlo simulation results for ENS_C under a severity-5 flood with a blind-pick repair strategy. The statistical mean (red) and median (green) are included.

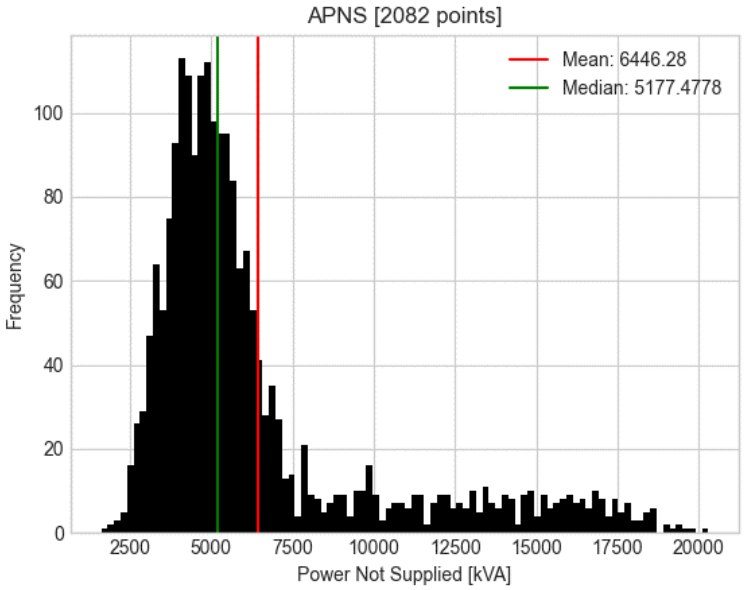

Figure D.6. Monte-Carlo simulation results for APNS under a severity-5 flood with a blind-pick repair strategy. The statistical mean (red) and median (green) are included.

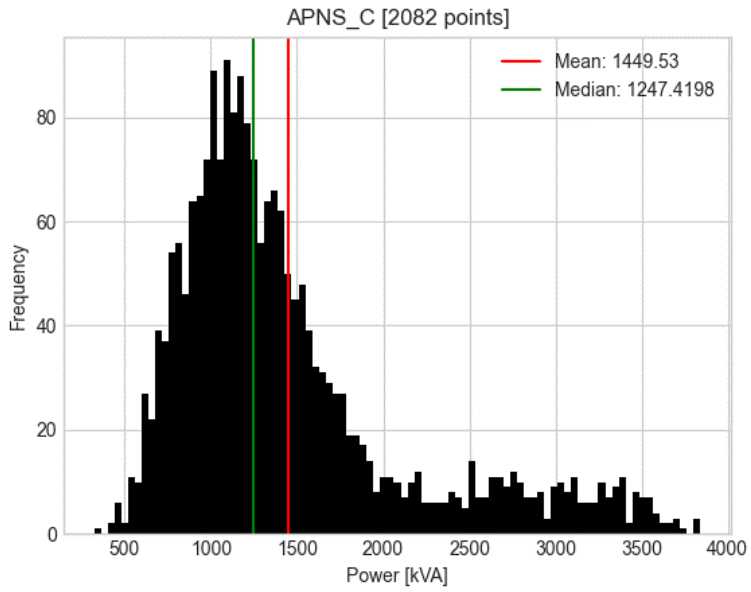

Figure D.7. Monte-Carlo simulation results for $APNS_C$ under a severity-5 flood with a blind-pick repair strategy. The statistical mean (red) and median (green) are included.

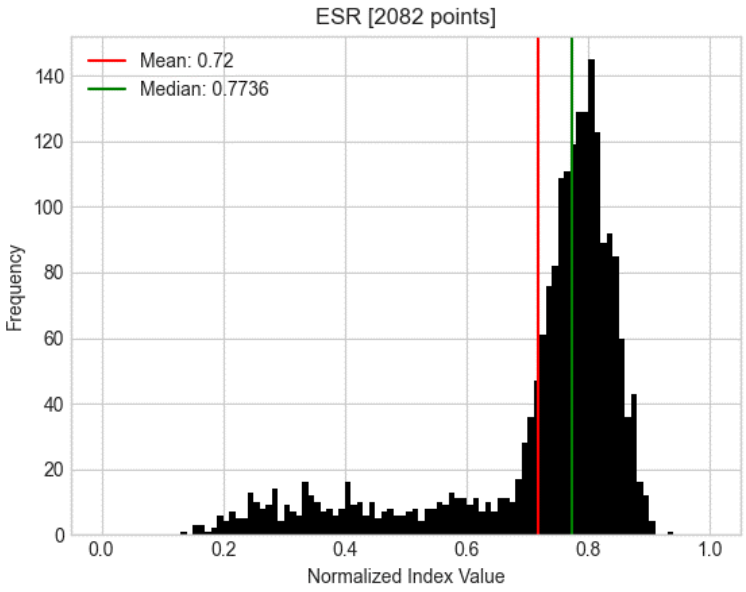

Figure D.8. Monte-Carlo simulation results for ESR under a severity-5 flood with a blind-pick repair strategy. The statistical mean (red) and median (green) are included.

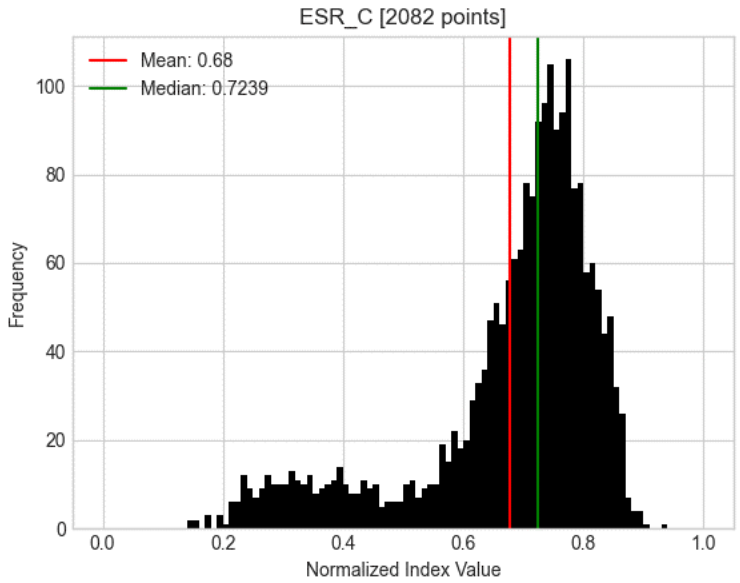

Figure D.9. Monte-Carlo simulation results for ESR_C under a severity-5 flood with a blind-pick repair strategy. The statistical mean (red) and median (green) are included.

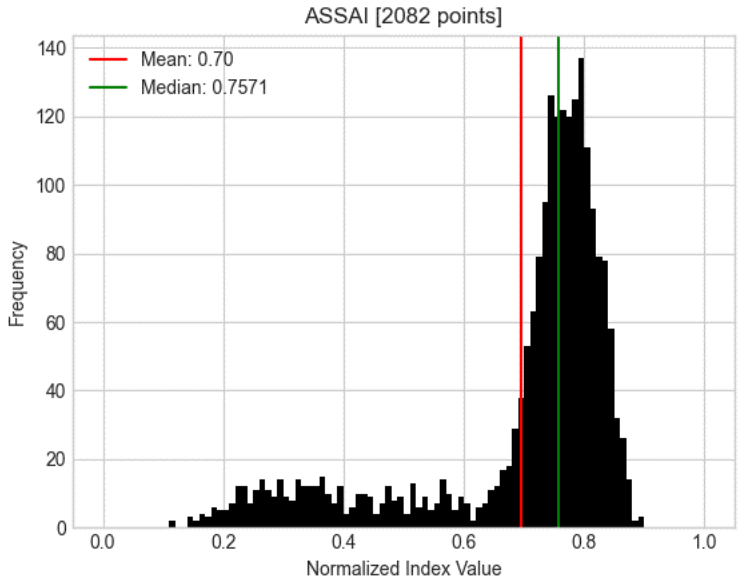

Figure D.10. Monte-Carlo simulation results for ASSAI under a severity-5 flood with a blind-pick repair strategy. The statistical mean (red) and median (green) are included.

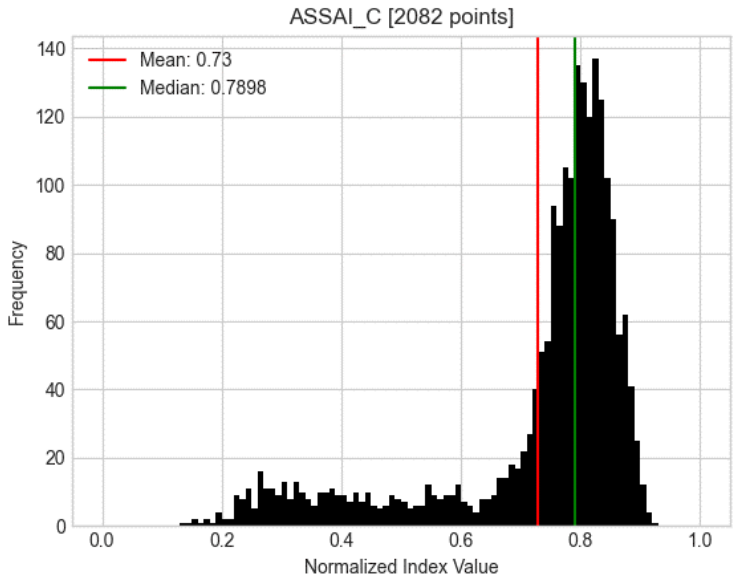

Figure D.11. Monte-Carlo simulation results for $ASSAI_C$ under a severity-5 flood with a blind-pick repair strategy. The statistical mean (red) and median (green) are included.

APPENDIX E

SIMULATION RESULT PLOTS FOR FIVE REPAIR CREWS

The following figures (Figures E.1-E.11) provide the statistical Monte-Carlo simulation results as a histogram for each resilience metric defined in chapter 5 of this paper. The statistical mean and median values are included on each plot.

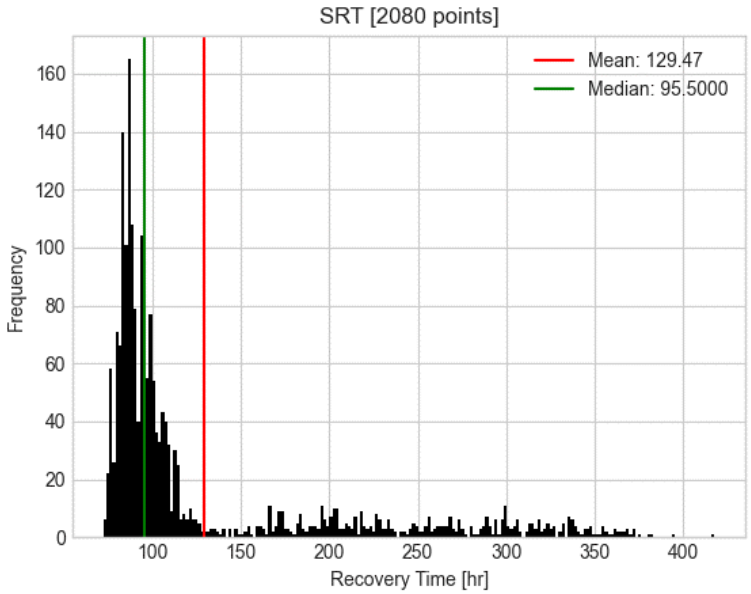

Figure E.1. Monte-Carlo simulation results for SRT under a severity-5 flood with a blind-pick repair strategy. The statistical mean (red) and median (green) are included.

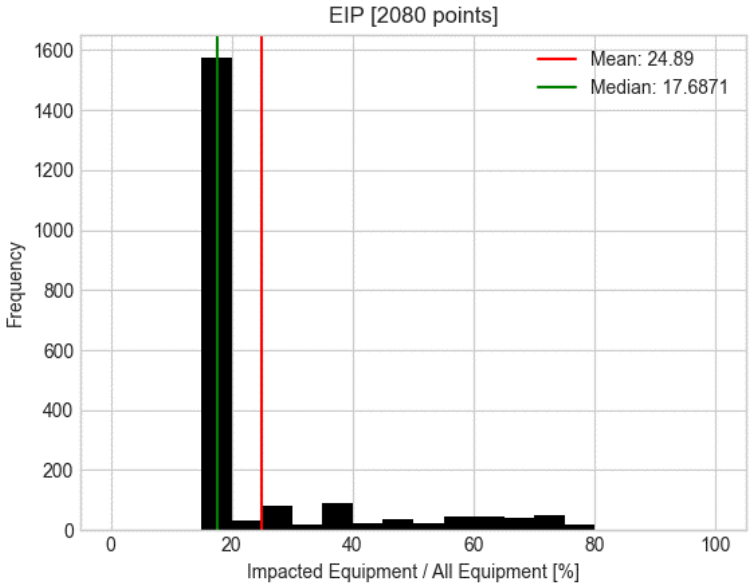

Figure E.2. Monte-Carlo simulation results for EIP under a severity-5 flood with a blind-pick repair strategy. The statistical mean (red) and median (green) are included.

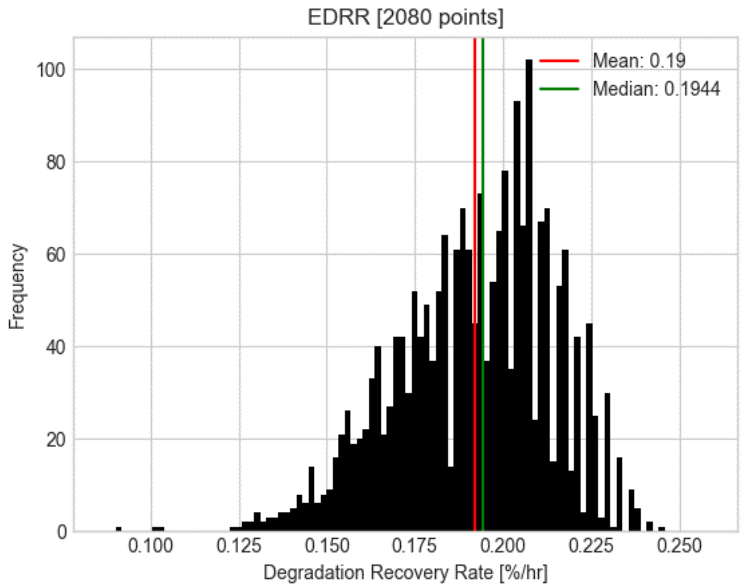

Figure E.3. Monte-Carlo simulation results for EDRR under a severity-5 flood with a blind-pick repair strategy. The statistical mean (red) and median (green) are included.

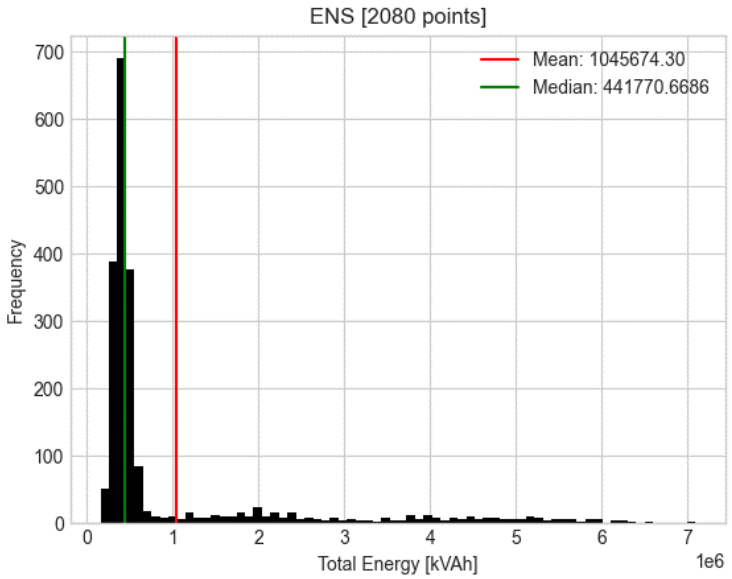

Figure E.4. Monte-Carlo simulation results for ENS under a severity-5 flood with a blind-pick repair strategy. The statistical mean (red) and median (green) are included.

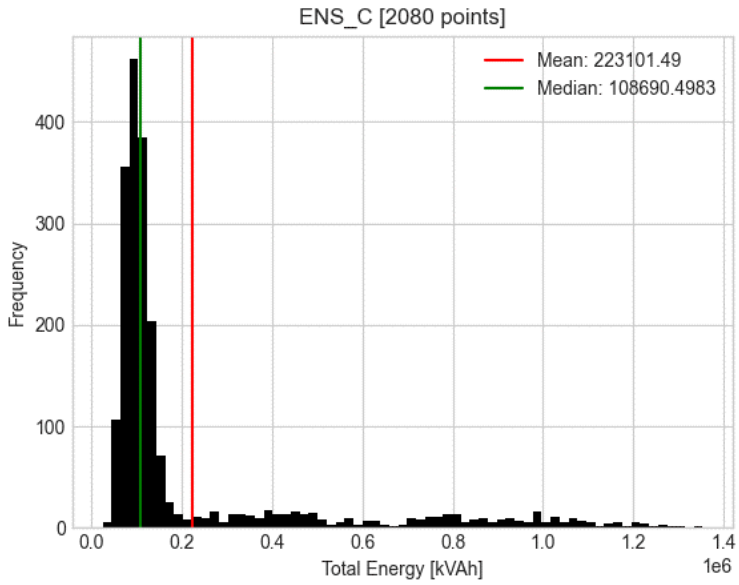

Figure E.5. Monte-Carlo simulation results for ENS_C under a severity-5 flood with a blind-pick repair strategy. The statistical mean (red) and median (green) are included.

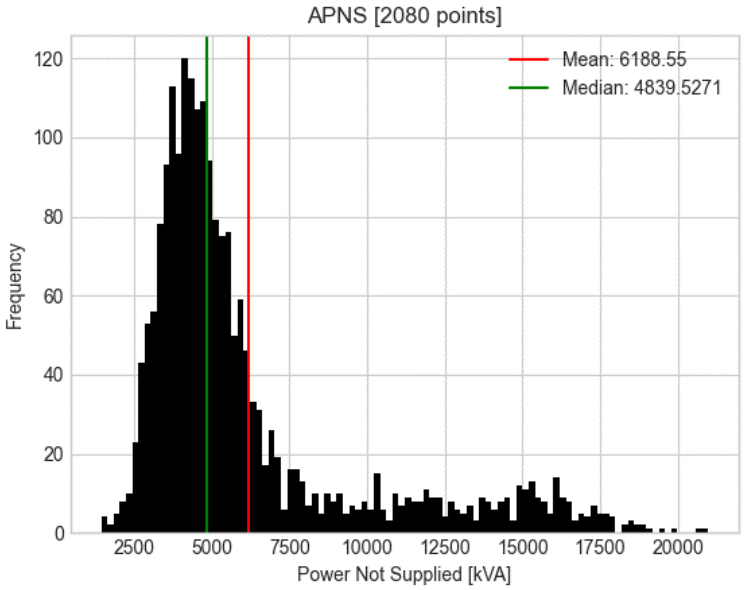

Figure E.6. Monte-Carlo simulation results for APNS under a severity-5 flood with a blind-pick repair strategy. The statistical mean (red) and median (green) are included.

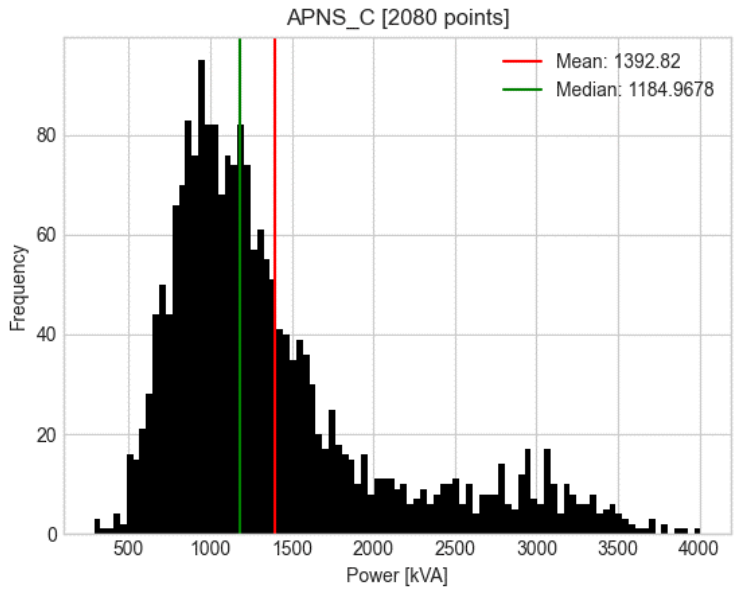

Figure E.7. Monte-Carlo simulation results for $APNS_C$ under a severity-5 flood with a blind-pick repair strategy. The statistical mean (red) and median (green) are included.

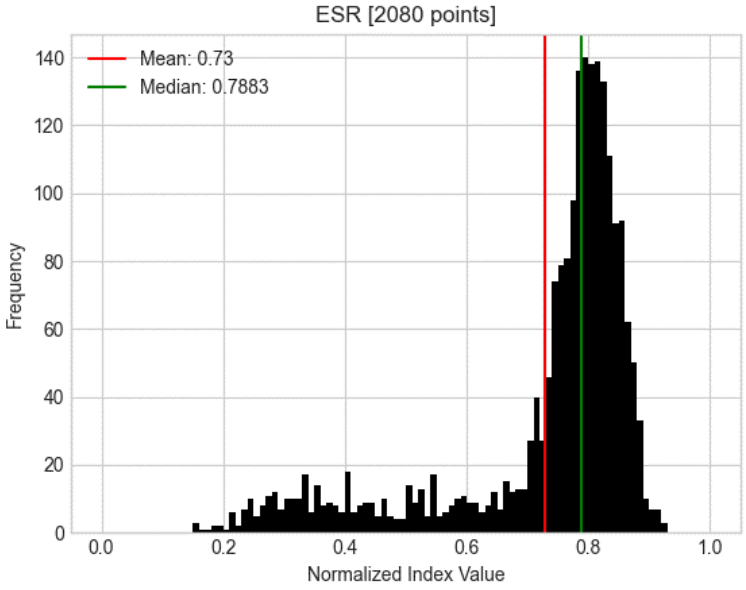

Figure E.8. Monte-Carlo simulation results for ESR under a severity-5 flood with a blind-pick repair strategy. The statistical mean (red) and median (green) are included.

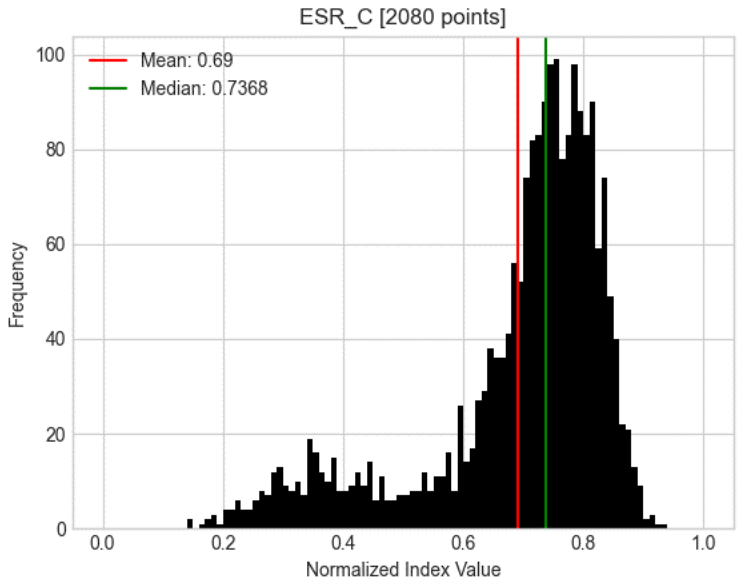

Figure E.9. Monte-Carlo simulation results for ESR_C under a severity-5 flood with a blind-pick repair strategy. The statistical mean (red) and median (green) are included.

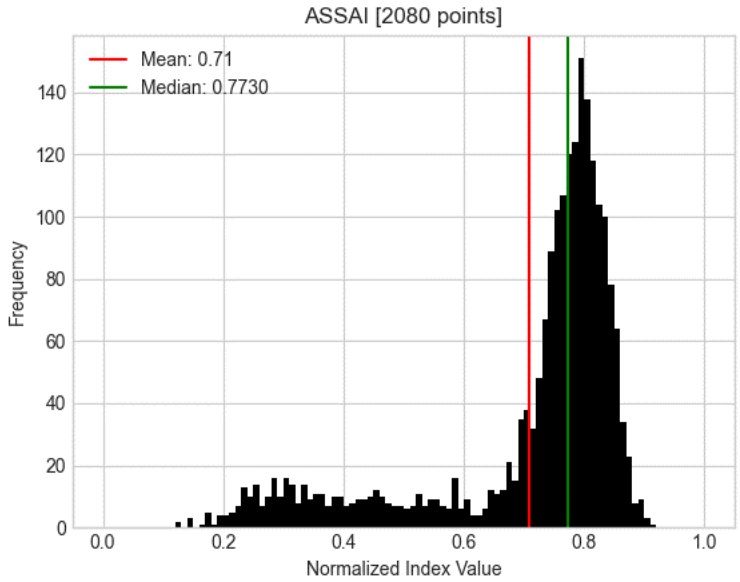

Figure E.10. Monte-Carlo simulation results for ASSAI under a severity-5 flood with a blind-pick repair strategy. The statistical mean (red) and median (green) are included.

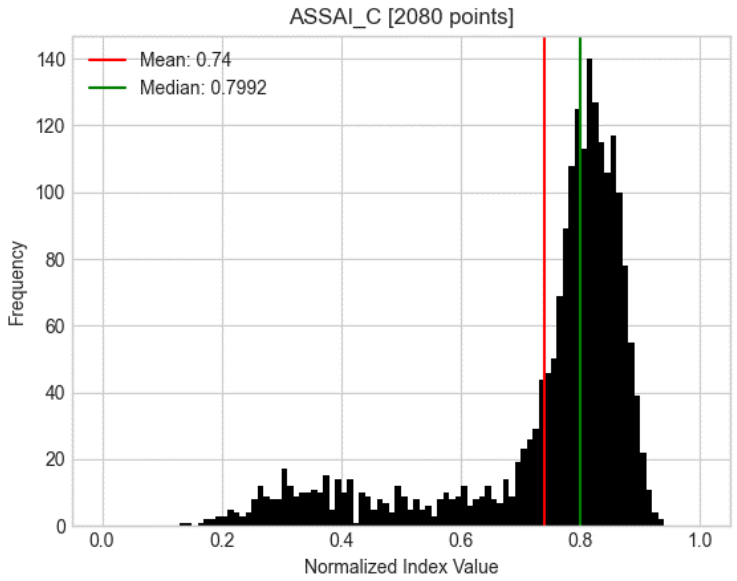

Figure E.11. Monte-Carlo simulation results for $ASSAI_C$ under a severity-5 flood with a blind-pick repair strategy. The statistical mean (red) and median (green) are included.

APPENDIX F

SIMULATION RESULT PLOTS FOR SIX REPAIR CREWS

The following figures (Figures F.1-F.11) provide the statistical Monte-Carlo simulation results as a histogram for each resilience metric defined in chapter 5 of this paper. The statistical mean and median values are included on each plot.

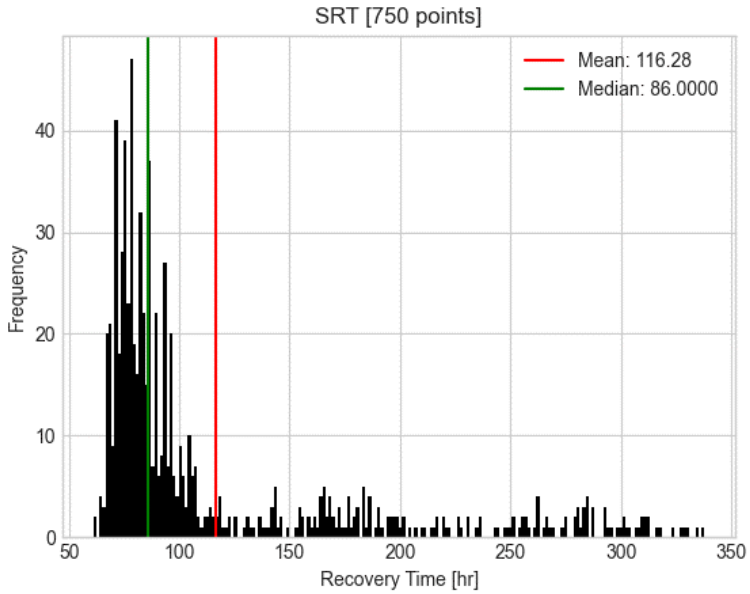

Figure F.1. Monte-Carlo simulation results for SRT under a severity-5 flood with a blind-pick repair strategy. The statistical mean (red) and median (green) are included.

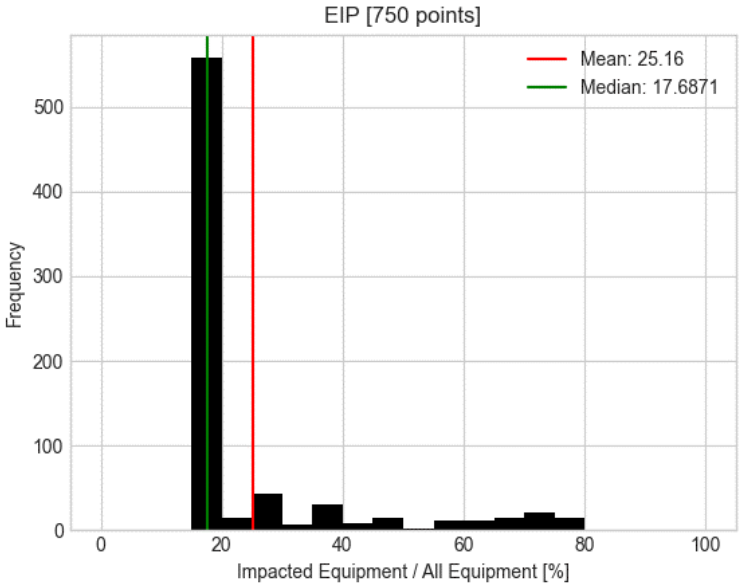

Figure F.2. Monte-Carlo simulation results for EIP under a severity-5 flood with a blind-pick repair strategy. The statistical mean (red) and median (green) are included.

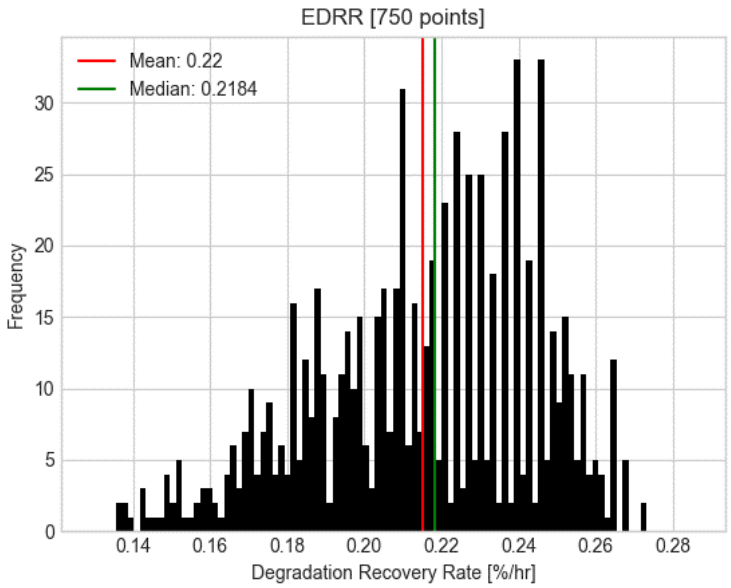

Figure F.3. Monte-Carlo simulation results for EDRR under a severity-5 flood with a blind-pick repair strategy. The statistical mean (red) and median (green) are included.

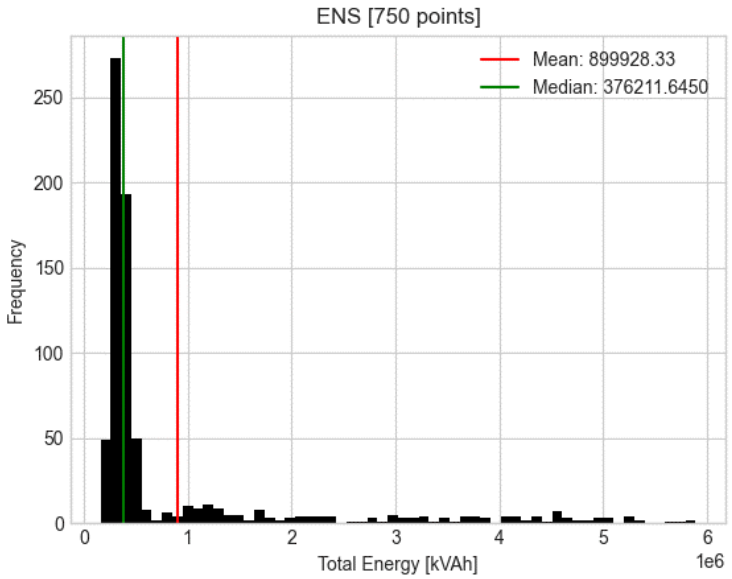

Figure F.4. Monte-Carlo simulation results for ENS under a severity-5 flood with a blind-pick repair strategy. The statistical mean (red) and median (green) are included.

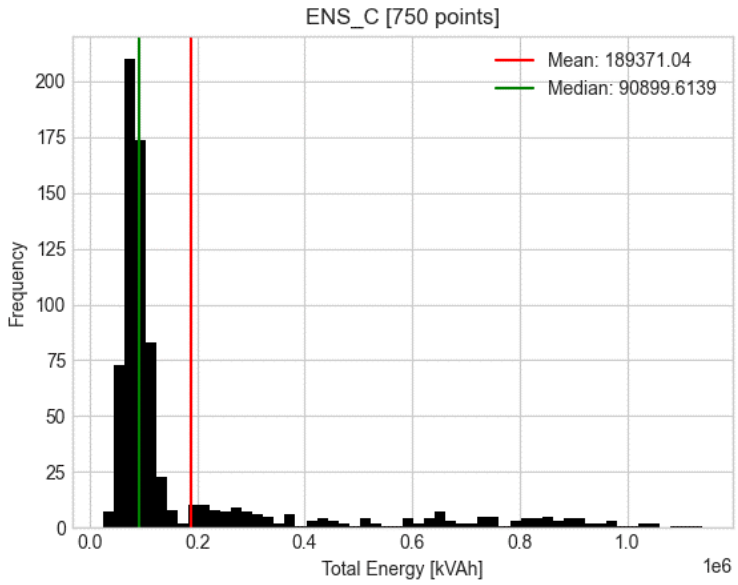

Figure F.5. Monte-Carlo simulation results for ENS_C under a severity-5 flood with a blind-pick repair strategy. The statistical mean (red) and median (green) are included.

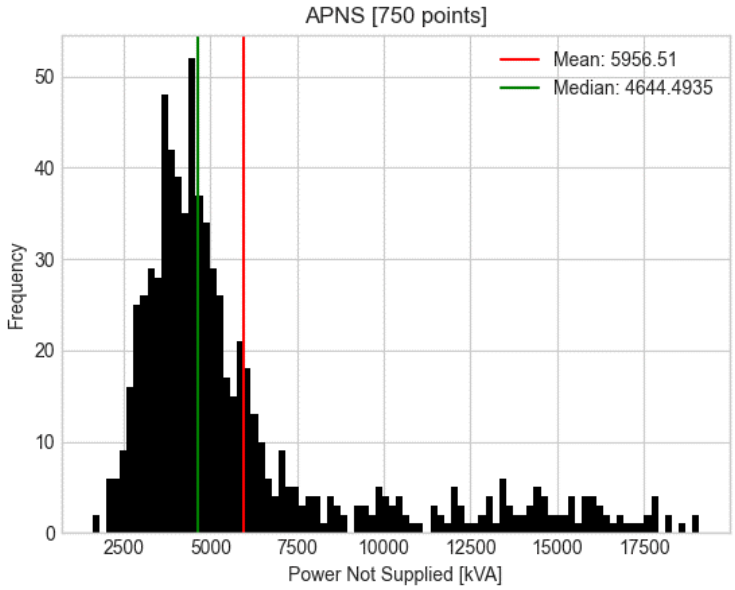

Figure F.6. Monte-Carlo simulation results for APNS under a severity-5 flood with a blind-pick repair strategy. The statistical mean (red) and median (green) are included.

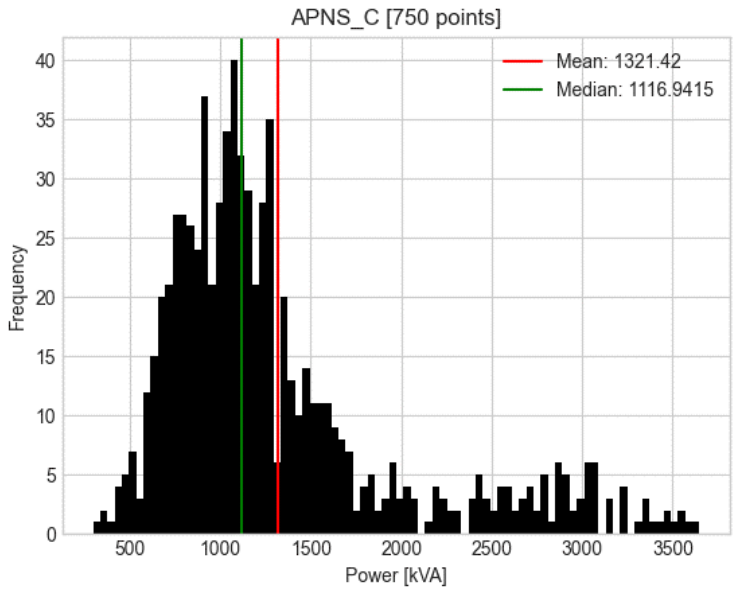

Figure F.7. Monte-Carlo simulation results for $APNS_C$ under a severity-5 flood with a blind-pick repair strategy. The statistical mean (red) and median (green) are included.

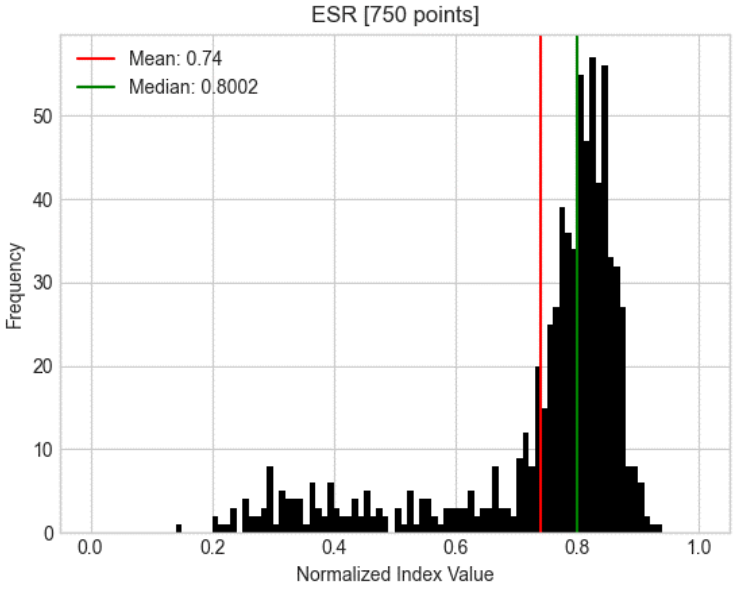

Figure F.8. Monte-Carlo simulation results for ESR under a severity-5 flood with a blind-pick repair strategy. The statistical mean (red) and median (green) are included.

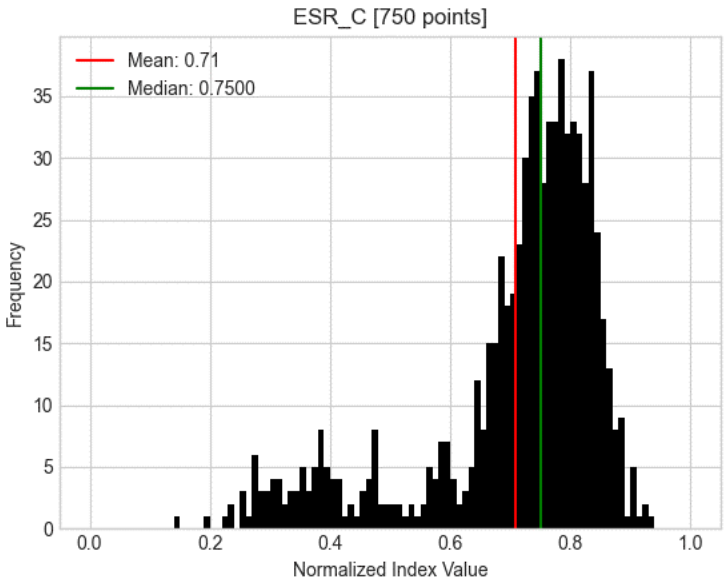

Figure F.9. Monte-Carlo simulation results for ESR_C under a severity-5 flood with a blind-pick repair strategy. The statistical mean (red) and median (green) are included.

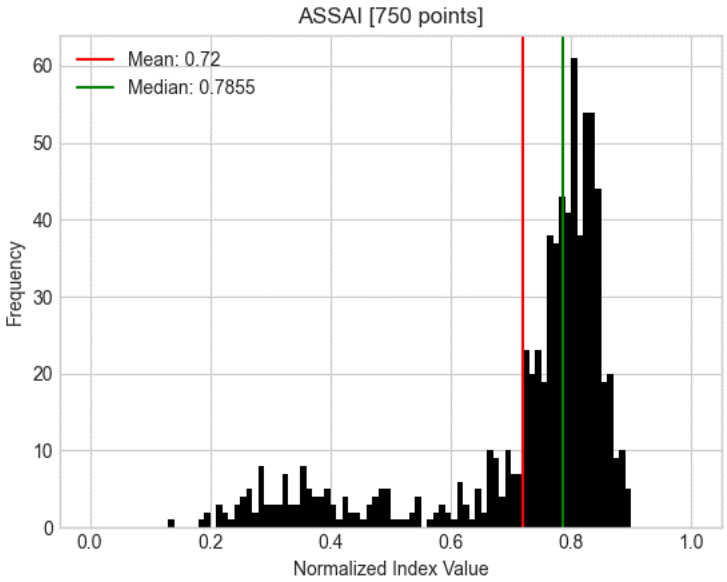

Figure F.10. Monte-Carlo simulation results for ASSAI under a severity-5 flood with a blind-pick repair strategy. The statistical mean (red) and median (green) are included.

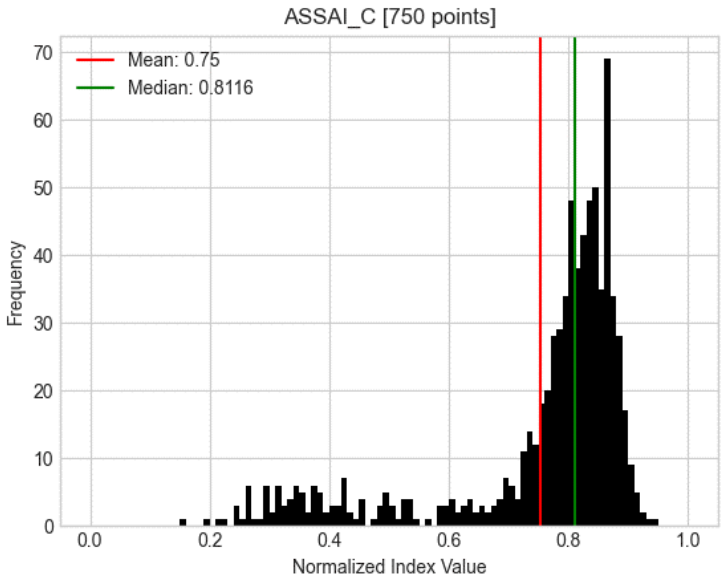

Figure F.11. Monte-Carlo simulation results for $ASSAI_C$ under a severity-5 flood with a blind-pick repair strategy. The statistical mean (red) and median (green) are included.